

# PROCEEDINGS

---

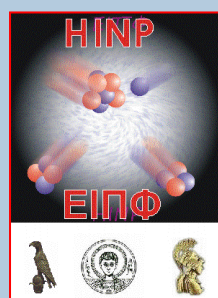
of the

## 3<sup>rd</sup> ONE-DAY WORKSHOP

on New Aspects and Perspectives in Nuclear Physics

LABORATORY OF PHYSICAL CHEMISTRY  
DEPARTMENT OF CHEMISTRY  
NATIONAL AND KAPODISTRIAN UNIVERSITY OF ATHENS

APRIL 8, 2016



### EDITORS

G. A. Souliotis  
A. Pakou

---

HELLENIC INSTITUTE OF NUCLEAR PHYSICS

**HELLENIC INSTITUTE OF NUCLEAR PHYSICS**

# **PROCEEDINGS**

of the

## **3<sup>rd</sup> ONE-DAY WORKSHOP**

**on New Aspects and Perspectives in Nuclear Physics**



**LABORATORY OF PHYSICAL CHEMISTRY  
DEPARTMENT OF CHEMISTRY  
NATIONAL AND KAPODISTRIAN UNIVERSITY OF ATHENS**

**APRIL 8, 2016**

# HELLENIC INSTITUTE OF NUCLEAR PHYSICS

## **GOVERNING BOARD**

G. Lalazissis (President)  
E. Styliaris (Vice President)  
A. Pakou (Secretary)  
G. A. Souliotis (Treasurer)  
P. Misaelides (Member)

## **ORGANIZING COMMITTEE**

G. A. Souliotis (Chair)  
D. Bonatsos  
E. Stiliaris  
A. Pakou  
G. Lalazissis

## **EDITORS**

G. A. Souliotis  
A. Pakou

## FOREWORD

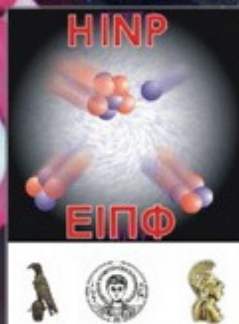
The 3rd Workshop on new Aspects and Perspectives in Nuclear Physics, sponsored by the Hellenic Institute of Nuclear Physics (HINP), was held at the Physical Chemistry Laboratory of the Department of Chemistry of the National and Kapodistrian University of Athens (NKUA), on the 8th of April, 2016. Following the tradition of the previous two workshops, the aim was to present an overview of new aspects and perspectives in Nuclear Physics, as demonstrated by research carried out at the national and international level, to promote synergy between the various groups and to conclude the current status, challenges and future opportunities in Nuclear Physics research in a round table discussion.

There has been an enthusiastic response to the Workshop in terms of the number of participants who gave oral presentations, covering a wide range of forefront aspects in the field of Nuclear Physics. Their paper contributions are included in this volume of Proceedings. As before, invited talks were not in the scope of the Workshop, as it was mainly organized to strengthen interaction between the members of the Institute.

We would like to thank the Department of Chemistry of NKUA for hosting the Workshop and the President of the Department for his encouragement and support. Finally, the support to technical aspects provided by the graduate students of the Physical Chemistry Laboratory is warmly acknowledged.

Georgios A. Souliotis  
on behalf of the Organizing Committee  
Athens, October 2016

# HELLENIC INSTITUTE OF NUCLEAR PHYSICS



## **3<sup>d</sup> one-day Workshop on New Aspects and Perspectives in Nuclear Physics**

**8<sup>th</sup> of April, 2016  
Athens, Greece**

**Nuclear Structure and Nuclear Astrophysics  
Nuclear Reactions, Rare Isotopes  
Hadronic Physics  
Applications of Nuclear Physics  
Discussion: The Present and Future of Nuclear Physics in Greece**

Laboratory of Physical Chemistry,  
Department of Chemistry,  
Physical Chemistry Room  
"Giannakopoulos", 5th floor  
University of Athens  
Panepistimiopolis, Zografou, GR-15771

<http://nuchem.chem.uoa.gr/hinpw3>

### **Organizing committee**

G. Souliotis (NKUA)  
E. Styliaris (NKUA)  
D. Bonatsos (NCRS)  
A. Pakou (Uoi)  
G. Lalazisis (AUTH)

## Contents

<i>The 2015 U.S. Long Range Plan for Nuclear Science</i> D. Bonatsos	1
<i>Development of numerical tools for phenomenological description of neutrino emission from microquasars</i> F. K. Anagnostopoulos, T. Smponias and T. S. Kosmas	3
<i>The role of magnetic fields in the formation and propagation of hadronic microquasars jets</i> E.-D. S. Paspaliaris, T. Smponias and T. S. Kosmas	11
<i>Speed of sound bounds and neutron star structure</i> Ch.C. Moustakidis, T. Gaitanos, Ch. Margaritis, and G.A. Lalazissis	18
<i>SU(3) symmetry in deformed nuclei</i> A. Martinou, I. E. Assimakis and D. Bonatsos	28
<i>New coupling scheme in heavy nuclei</i> I. E. Assimakis, A. Martinou and D. Bonatsos	31
<i>Multi-strangeness production in hadron induced reactions</i> T. Gaitanos, Ch. Moustakidis, G.A. Lalazissis and H. Lenske	34
<i>Lifetime of the 4+1 state of <math>^{148}\text{Ce}</math> and its B4/2 ratio</i> P. Koseoglou, V. Werner, N. Pietralla et al.	43
<i>Systematic study of proton-induced spallation reactions with the Constrained Molecular Dynamics (CoMD) model</i> A. Assimakopoulou, G. A. Souliotis, A. Bonasera and M. Veselsky	50
<i>Probing the cluster structure of <math>^7\text{Li}</math> via elastic scattering on protons and deuterons in inverse kinematics</i> A. Pakou, V. Soukeras et al.	55
<i>Influence of resonance and continuum states on elastic scattering of <math>^6\text{Li}+p</math></i> V. Soukeras, A. Pakou et al.	61
<i>Study of the <math>^6\text{Li}+p \rightarrow ^3\text{He}+^4\text{He}</math> reaction in inverse kinematics</i> Ch. Betsou, A. Pakou et al.	67
<i>Alpha - particle production in the reaction <math>^7\text{Be}+^{28}\text{Si}</math> at near barrier energies</i> O. Sgouros, A. Pakou et al.	73
<i>Multi-sequential decay of <math>^{40}\text{Ar}</math> projectiles at 27.6 MeV/A</i> N.G. Nicolis	79

<i>Production of rare isotopes toward the astrophysical r-process path</i> G.A. Souliotis, A. Papageorgiou et al.	85
<i>Neutron-Rich Isotope Production in <math>^{238}\text{U}</math> Projectile Fission at 20 MeV/nucleon</i> N. Vonta , G.A. Souliotis et al.	93
<i>Rare Isotope Production in peripheral heavy-ion collisions in the energy range 15-25 MeV/nucleon</i> A. Papageorgiou, G.A. Souliotis et al.	102
<i>Microscopic description of neutron-induced fission with the CoMD Model: Preliminary Results</i> S. Papadimitriou, G.A. Souliotis, A. Assimakopoulou, A. Bonasera and M. Veselsky	111

# The 2015 U.S. Long Range Plan for Nuclear Science

Dennis Bonatsos\*

*Institute of Nuclear and Particle Physics, National Center for Scientific Research  
“Demokritos”, Athens, Greece*

---

## Abstract

The 2015 Long Range Plan for Nuclear Science [1], released in October 2015 by the U.S. Nuclear Science Advisory Committee, is reviewed, with emphasis on new directions in the field of nuclear science and new facilities under construction, as well as on manpower, budget, and the broader impacts of nuclear science.

*Keywords:* nuclear science, long range plan, U.S.A.

---

Given the size limitations, lists of keywords are presented.

### 1. Quantum Chromodynamics

The fundamental description of the heart of visible matter

- QCD and the structure of hadrons and nuclei
- QCD and the phases of strongly interacting matter
- Understanding the glue that binds us: The next QCD frontier in NP

*High-energy nuclear physics / QCD facilities*

- Continuous Electron Beam Accelerator Facility (CEBAF), Newport News, Virginia, 12 GeV upgrade, Thomas Jefferson National Accelerator Facility (JLab)
- Relativistic Heavy Ion Collider (RHIC), Upton, Long Island, New York, Brookhaven National Laboratory (BNL)
- Electron Ion Collider (EIC), future

### 2. Nuclear structure and reactions

288 stable isotopes, 3000 isotopes known, >6000 isotopes predicted

---

\*e-mail: bonat@inp.demokritos.gr

- Proton drip line reached up to  $Z=83$ , Neutron drip line reached up to  $Z=8$
- Current upper limit  $Z=118$ ,  $A=294$

### **3. Nuclear Astrophysics**

- Origin of the elements
- The life of stars, The death of stars, The matter of neutron stars

#### *Facilities for Nuclear Structure and Astrophysics*

- Argonne Tandem Linac Accelerator System (ATLAS), Lemont, Chicago, Illinois, Argonne National Laboratory (ANL)
- National Superconducting Cyclotron Laboratory (NSCL), East Lansing, Michigan, Michigan State University (MSU)
- Facility for Rare Isotope Beams (FRIB) 2020-2022
- 88-inch Cyclotron, Berkeley Hills, Berkeley, California, Lawrence Berkeley National Laboratory (LBNL)
- Association for Research at University Nuclear Accelerators (ARUNA), 12 institutions, John D. Fox Accelerator Laboratory, Florida State University

### **4. Fundamental Symmetries and Neutrinos**

- What are the absolute masses of neutrinos, and how have they shaped the evolution of the universe?
- Are neutrinos their own antiparticles?
- Why is there more matter than antimatter in the present universe?
- What are the unseen forces that disappeared from view as the universe expanded and cooled?

#### *Facilities for Fundamental Symmetries and Neutrino Physics*

- Sanford Underground Research Facility (SURF), Lead, South Dakota, former Homestake gold mine
- Fundamental Neutron Physics Beamline (FnPB), Spallation Neutron Source (SNS), Oak Ridge National Lab (ORNL), Oak Ridge, Knoxville, Tennessee
- UltraCold Neutron (UCL) facility, Los Alamos National Lab (LANL), Los Alamos, New Mexico
- Fermilab Muon Campus, Fermi National Accelerator Laboratory, Batavia, Chicago, Illinois

## **5. Theoretical Nuclear Physics**

- New investments in computational nuclear theory
- FRIB Theory Alliance, Facility for Rare Isotope Beams
- Topical Collaborations

Theory of Reactions for Unstable Isotopes (TORUS)

Neutrinos and Nucleosynthesis in Hot and Dense Matter (NuN)

Jet and Electromagnetic Tomography (JET)

## **6. Workforce, Education, and Outreach**

- Undergraduate Research Experience
- National Nuclear Physics Summer School (NNPSS)
- Nuclear Science Outreach to Students and the Public

## **7. Broader Impacts Medicine**

- Clinical diagnosis of cancers using isotopes
- Alpha emitters for cancer therapy, Proton radiation therapy

## **8. Broader impacts other**

- National security, Radioisotope dating
- Elemental analysis (PIXE, PIGE, RBS, NAA, XRF)
- Nondestructive studies in art and archaeology
- Energy (99 reactors, 5 under construction 12 under active review by the NRC)
- Accelerator applications (Purposeful modification of materials, Destroying food- and water-borne pathogens)

## **9. Budgets**

- Department of Energy, Office of Science, Office of Nuclear Physics
- National Science Foundation, Mathematical and Physical Sciences Directorate, Physics Division

## **References**

- [1] [http://science.energy.gov/~media/np/nsac/pdf/2015LRP/2015\\_LRPNS\\_091815.pdf](http://science.energy.gov/~media/np/nsac/pdf/2015LRP/2015_LRPNS_091815.pdf)

# Development of numerical tools for phenomenological description of neutrino emission from microquasars

F. K. Anagnostopoulos<sup>1,\*</sup>, T. Smponias<sup>2</sup>, T. S. Kosmas<sup>2</sup>

*<sup>1</sup> Physics Department, National and Kapodistrian University, Athens*

*<sup>2</sup> Physics Department, University of Ioannina, 45110 Ioannina, Greece*

---

## Abstract

The main objective of this work is the development of efficient numerical tools for simulating the neutrino emission from microquasars. We considered hadronic jets for which the main contribution to the neutrino emission comes from the proton-proton interactions taking place in relativistic jets. We created a code to calculate the neutrino emission from a model jet simulated with the PLUTO hydro-code and the necessary physical quantities, i.e. the pion injection function and the pion energy distribution at an elementary unit volume (grid) of PLUTO. The derived code is able to reliably reproduce the aforementioned physical quantities with quite good accuracy. Moreover, by combining our code with the PLUTO hydro-code and the radiative transfer code of Ref. [8], one may simulate non-thermal emissions from MQ jets by consuming less time than when using the code of Ref. [3]. This offers the possibility to obtain simulations of better precision and also the opportunity of refining the model in use.

**Keywords** X-ray binaries, neutrinos, simulation, non-thermal emission

---

## INTRODUCTION

A microquasar (MQ) is an X-Ray Binary Star (XRB) with twin, collimated, relativistic jets, [1]. It consists of main-sequence (companion) star, in coupled orbit with a compact astrophysical object (black hole, neutron star). There is mass accretion to the compact object by means of stellar wind or mass flux through the inner Lagrangian Point (Roche Lobe Overflow). Due to the conservation of angular momentum, an accretion disc is formed. From an observational point of view, a MQ is strongly luminous in the X-Ray and Radio wavelengths, with a time-dependent spectrum. MQ's are important because they have a close resemblance with Active Galactic Nuclei (AGN, or quasars), an astrophysical system with growing importance for cosmology. In addition to this, MQ' s provide an identical environment for testing black hole solutions. So, a deep understanding of the astrophysical conditions in MQ's is highly desirable.

Following the recent developments in the detection of the astrophysical neutrinos from IceCube, Ref.[11], we placed emphasis on the study of the possible neutrino emission. Although the content of the jet is still in debate, there are observations of Fe II lines. The latter means that there is hadronic content in the jets. A common assumption is that the jet consists of protons only (bulk flow protons). A small amount of them are accelerated (via 1<sup>st</sup>-order Fermi acceleration) at shock fronts within the jet, and in turn collide with bulk jet flow (cold) protons. In general, accelerated particles in the jet can

---

\* Corresponding author, e-mail: fotis-anagnostopoulos@hotmail.com

gain energies up to  $10^7$  GeV. In such MQ jets, the main contribution to the neutrino emission comes from the proton-proton interactions taking place in the jets [2, 4]. Proton-proton interactions produce pions which may decay to muons and neutrinos (prompt neutrinos). Furthermore, muons may decay to electrons and neutrinos (delayed neutrinos). Neutral pions and mesons decay quickly producing high energy  $\gamma$ -rays.

The importance of simulating the neutrino flux from a MQ is severe because of the possibilities for understanding the jet launching mechanisms and/or its substance. On the other hand, it may be useful for studying physics beyond of the standard model to having neutrinos with known characteristics (i.e energy spectrum and flavor) traveling at astronomical distances, [5].

In previous papers [3,7,8] the simulation has the following stages:

(a)The jet is simulated using a magnetohydrodynamical code (i.e PLUTO), which calculates the values of physical quantities (i.e magnetic field, mass density) for every cell.

(b)For calculating the neutrino emissivity per grid cell, they used the formalism of Ref [2] and an appropriate algorithm. The latter takes as input the aforementioned physical quantities.

This work aims to provide an efficient numerical tool for more realistic modeling of the neutrino emission from MQs.

## A BRIEF DESCRIPTION OF OUR MODEL

In order to simulate the neutrino flux, according to [5], we need:

- Description and energy spectrum of primary particles (protons)
- The properties of the target material with which the above interacts.
- Modelling of the properties of the particle production of hadronic interactions
- A description of the properties of the medium (astrophysical conditions).
- The (relative well) known properties of weak decays.

### (a)Assumptions

- i. We speculate that there are hadronic jets only, that consists of protons.
- ii. The source from which the secondary particles (pions) are injected is isotropic and time-independent.
- iii. One-zone approximation: The particle acceleration happens in such a way that the diffusion effects could be ignored, Ref. [2].
- iv. We ignore jet-clumps interactions.
- v. Only the synchrotron and adiabatic expansion energy loss mechanisms are considered.
- vi. The primary particles (protons) are accelerated via 1<sup>st</sup>-order Fermi mechanism only.
- Vii. Only prompt neutrinos are considered.

### (b)Formalism

The pion injection function, [2]:

$$Q_{\pi}^{pp}(E_{\pi}) = n_{gas} c \int_{\frac{E_{\pi}}{E_{\pi}^{max}}}^1 N_p \left( \frac{E_{\pi}}{X} \right) F_{pp} \left( \frac{E_{\pi}}{X}, X \right) \sigma_{pp}^{inel.} \left( \frac{E_{\pi}}{X} \right) \frac{dX}{X}$$

The pion injection function gives the possibility for the production of a pion with energy

in the range  $E_n$  to  $E_n^{\max}$ . The quantities  $F_{pp}$ ,  $\sigma_{pp}^{inel}$ ,  $N_p$  are the proton injection function, the p-p inelastic interactions cross section and the energy spectrum of the non-thermal protons, respectively. From Ref. [2, 4] we got:

$$F_{pp}\left(\frac{E_\pi}{x}, x\right) = 4aB_\pi x^{a-1} \left(\frac{1-x^a}{1+rx^a(1-x^a)}\right)^4 \left(\frac{1}{1-x^a} + \frac{r(1-2x^a)}{1+rx^a(1-x^a)}\right) \left(1 - \frac{m_\pi c^2}{xE_p}\right)^{1/2}$$

$$x = \frac{E_\pi}{E_p}, a' = 3.67 + 0.83L + 0.075L^2, B_\pi = \alpha' + 0.25, r = 2.6/\sqrt{a'},$$

$$\sigma_{pp}^{(inel.)}(E_p) = (34.3 + 1.88L + 0.25L^2) \left(1 - \left(\frac{E_{th.}}{E_p}\right)^4\right)^2 10^{-27}, L = \ln\left(\frac{E_p}{10000 \text{ GeV}}\right), N_p(E_p) = \frac{K_0}{E_p^\lambda}$$

The value of the spectral indice lambda is 2 if the protons are accelerated via the 1<sup>st</sup> order Fermi mechanism, Ref. [10]. In order to calculate the neutrino energy, the energy spectrum of a pion right before its annihilation is needed. This satisfies the general transport equation of Ref. [9]. The latter equation written with our formalism:

$$\frac{\partial N(E_\pi, t, \mathbf{r})}{\partial t} - D(E_\pi) \nabla N(E_\pi, t, \mathbf{r}) + \frac{\partial (N(E_\pi, t, \mathbf{r}) b_\pi(E_\pi))}{\partial E_\pi} + t_\pi^{-1} N(E_\pi, t, \mathbf{r}) = Q_\pi^{pp}(E_\pi, t, \mathbf{r})$$

The quantity  $N_p$  stands for the steady state pion distribution and corresponds to the energy spectrum of a pion right before its annihilation to give neutrinos. Also,

$$b_\pi(E_\pi) = -E_\pi(t_{syn}^{-1} + t_{ad.}^{-1}), t_\pi^{-1}(E_\pi) = t_{esc}^{-1} + t_{dec.}^{-1}, \text{ where } t_{dec.}^{-1} = \left(\frac{\tau_{0\pi}}{\gamma(E_\pi)}\right)^{-1}, t_{esc.}^{-1} = c/z$$

Using the assumptions of the previous subsection:

$$\frac{d(N(E_\pi) b_\pi(E_\pi))}{dE_\pi} + t_\pi^{-1} N(E_\pi) = Q_\pi^{pp}(E_\pi)$$

The latter formula is slightly different from the equivalent in Ref. [2] due to intrinsic differences between our model and the geometrical model used therein.

It is trivial to solve the previous ODE to obtain  $N_n$ . Then we have:

$$N_\pi(E_\pi) = \frac{1}{|b_\pi(E_\pi)|} \int_{E_n}^{E_n^{\max}} Q_{pp}^{(inel.)}(E') e^{\tau_\pi(E_\pi, E')} dE', \text{ where } \tau_\pi(E_\pi, E') = \int_{E'}^E \frac{t_\pi^{-1}(E'')}{|b_\pi(E'')|} dE''$$

### (c) Parameters and Constants

Parameters	Values	Comments
$z(\text{cm})$	$10^{11}$	Cell's characteristic dimension
$M_{BH}(M_{solar})$	10	Compact Object mass
$n(1/\text{cm})^3$	$10^{10}$	Cold protons numerical density
$q_{rel.}(\text{dimensionless})$	$2.9 \cdot 10^{-3}$	Ratio of cold protons/non thermal protons kinetic energy, [2,3]
$R_0(\text{cm})$	$5R_{sch}$	Distance of the base of the jet from the compact object

Parameters	Values	Comments
$E_p^{\max}$ (GeV)	$10^7$	Maximum energy of a fast proton, [2,3,7,8].
$E_p^{\min}$ (GeV)	1.22	Threshold energy for p-p interaction
$E_n^{\max}$ (GeV)	$10^7$	Maximum energy of a pion produced from a fast proton
$E_n^{\min}$ (MeV)	139.5	Pion energy at rest
B(G)	400	Characteristic value of the magnetic field in the jet
$L_k$ (erg/s)	$10^{39}$	Kinetic luminosity of the jet, [2,3]

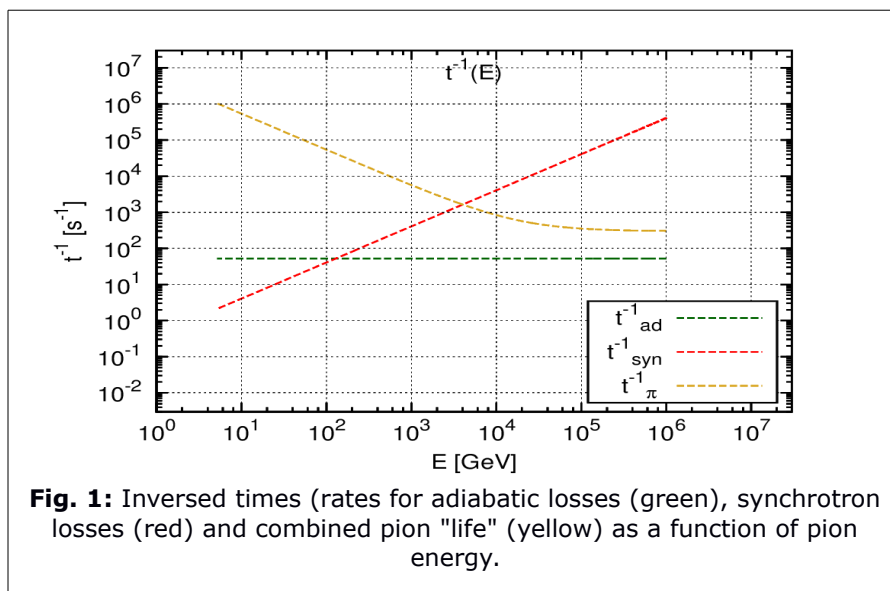
The maximum energy of the secondary particles is obtained equating the various deceleration rates with the acceleration rate, [3]. The kinetic luminosity estimation comes from observations of the interactions between the jet of SS-433 MQ and the W50 supernova remnant. In our code we avoided common block structures and we used extensively library (.h) files. We tested our code using a PC with the following characteristics:

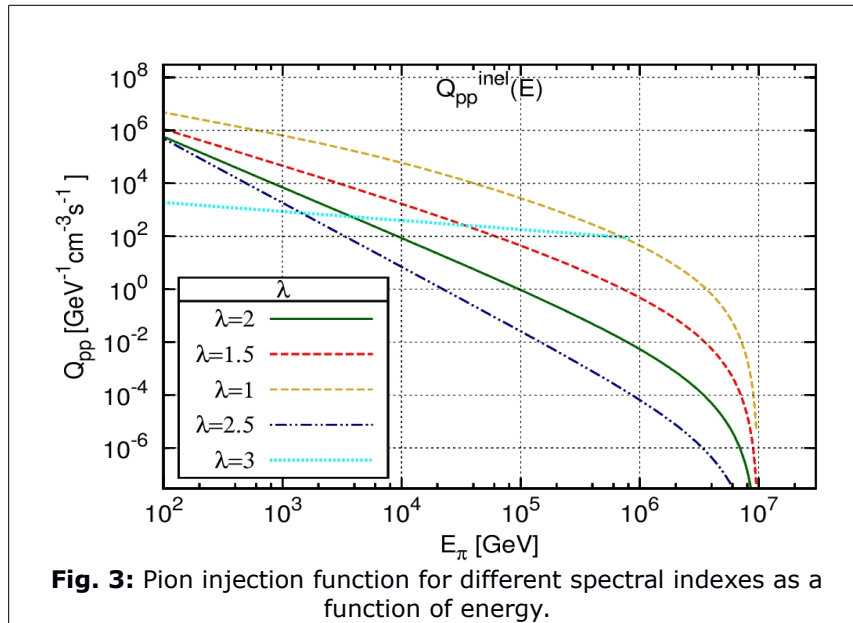
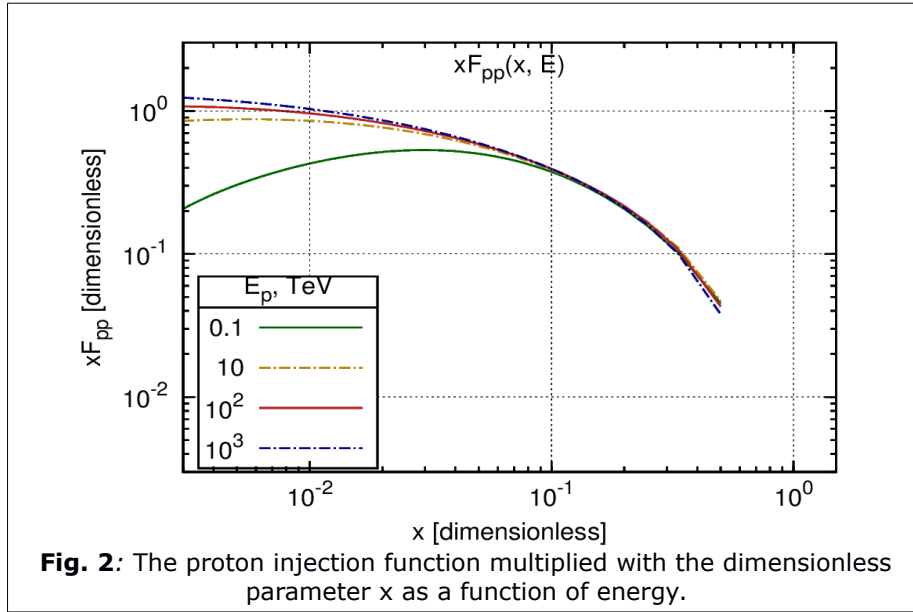
Total memory RAM: 3934 Megabytes

Processor: Intel(R) Core(TM) i5-2500 CPU 3.30 GHz

## RESULTS AND DISCUSSION

Using the code described in the previous section we obtained the following results.



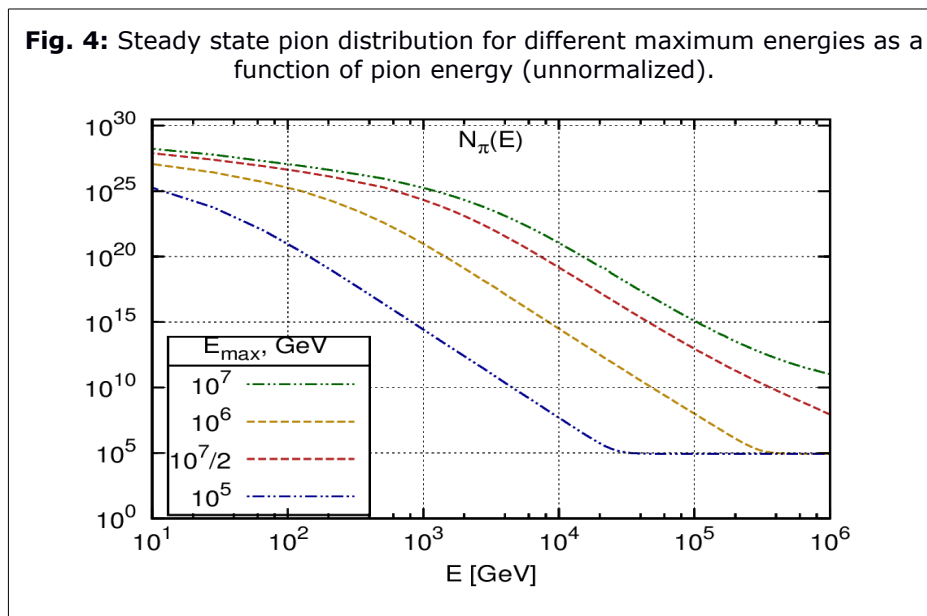


Comparing the characteristic rates for the synchrotron, adiabatic losses and pion annihilation in the volume of concern as functions of pion energy with the same in Ref. [2], we could say that the functional form is the same. A small numerical difference in the reversed rate of adiabatic losses is due to differences in the definition of  $z$ .

Then, comparing the diagram of the proton injection function multiplied with the pion/proton energy ratio ( $x$ ) as a function of energy with the same in Ref [4], we conclude full identity. An exception is for  $E=0.1$  TeV because in Ref [4] the natural system of units is employed and so we got a difference in a factor of  $c$ , for small energies.

As it is expected from the physical meaning of the pion injection function (probability of injection in the flow of pions with energy between  $E_n$  and  $E_n+dE_n$ ), it is falling as a power law, with different steep for different spectral index. In general,  $\lambda$  smaller or equal to 2 corresponds to 1<sup>st</sup> order Fermi mechanism and lambda bigger means 2<sup>nd</sup> order Fermi acceleration or other mechanisms, [10]. In reality, the

region of the source it is not compact, which means that a contribution from different spectral indexes is expected. However, a value of  $\lambda=3$  gives almost steady injection function that is unphysical, at least with our current understanding of the astrophysical environment into the jet. The curve for  $\lambda=2$  is in very good agreement with the same of Ref. [3].



Moreover, we plot the steady state distribution of pions as a function of energy. The curvature of the curve changes in the above-mentioned energy range in a way that is intuitively spurious. As a result, we decided to run our code for different maximum energies. The result is a non-linear behavior as it seen above (Fig. 4). However, in the energy range of interest there is a sufficient stability. Also, if we compare this with the same quantity used in Ref. [3], we could say that is almost identical.

## CONCLUSIONS

We developed an efficient numerical tool for calculating the neutrino emission from MQ's jets. Using the aforementioned code we were able to reliably reproduce with good accuracy the results of the previews works. Also, we explored different acceleration mechanisms of the fast protons that probably are working at the astrophysical environment of a MQ. The latter code is written in C programming language. This, among many things, makes it more easily used along with PLUTO (which is written also in C). In addition to this, is consuming sufficiently less computational time than any other in the literature. That could improve the resolution of the grid used from the PLUTO' s simulation, which means more realistic results. It is important to note that our code is extremely flexible, so we could change the physical model without important changes in our code.

Combining the results of the simulations of the jets with the results of theoretical calculations, of the emissivity of neutrinos and the cross sections of p-p and p- $\gamma$  collisions, using numerical methods, can lead to a detailed investigation of the neutrino production from the microquasars jets. These methods can also be used for the gamma rays emission of the jets.

Lastly, we aim to include more energy losing mechanisms and in general to refine the previously described assumptions in an effort to make predictions for future observations of IceCube observatory.

## References

- [1] F. I. Mirabel, *Annu. Rev. Astron. Astrophys.* 37, 409 (1999)
- [2] M. M. Reynoso, G. E. Romero, *Astron. Astrophys.* 493, 1 (2013)
- [3] T. Smponias, T. S. Kosmas, *MNRAS* 438, 1014 (2014)
- [4] S. R. Kelner et al, *Phys. Rev. D* 79, 039901 (2009)
- [5] P. Lipari et al, *Phys. Rev. D* 75, 123005 (2007)
- [6] A. Mignone et al., *The Astrophys. J. Suppl. Series* 170, 228 (2007)
- [7] T. Smponias, T. S. Kosmas, *MNRAS* 412, 132 (2011)
- [8] T. Smponias, O. T. Kosmas, *Advan. High Energy Phys.*, ID 921757, in press.
- [9] Syrovatskii, S. I., *Soviet Astronomy* 3, 22 (1959)
- [10] Rieger, F. M., Bosch-Ramon, V., & Duffy, P., *Astrophys. Space Scien.*, 309 (2007)
- [10] R.M. G. Aartsen et al. (IceCube Collaboration), *Phys. Rev. Lett.*, 115 (2015)

# The role of magnetic fields in the formation and propagation of hadronic microquasars jets

E.-D. S. Paspaliaris<sup>1,\*</sup>, T. Smponias<sup>1</sup>, T. S. Kosmas<sup>1</sup>

<sup>1</sup>*Department of Physics, University of Ioannina, 45110 Ioannina, Greece.*

---

## Abstract

In the present work, we examine the role of the magnetic field, which causes a rather pronounced confinement of the jets at microquasars (MQ). Due to radial Lorentz forces acting on the jet's matter towards the jet's axis, the outgoing flux is collimated along the same axis and vertically to the compact object. Alternatively, a rotating central object may drag the surrounding magnetic field into collimation around the produced jet. In such objects, jet emerges from each side of the accretion disc.

These jets operate as cosmic engines, capable of accelerating particles on very high energies ( $\sim 10^2$  TeV) and consist sources of high energy neutrinos and gamma rays. We also examine the role of the magnetic field (MF), which causes to a rather pronounced jet confinement. Our aim is to investigate and model its role on various physical observables of the jet, by simulating the jet's flow and derive 2D and 3D visualizations and furthermore examine its effect on the neutrino emissivity.

**Keywords** hadronic jets, microquasars, magnetic fields, simulation, neutrinos

---

## INTRODUCTION

In general, jets can be produced in binary systems known as microquasars, being sources of high energy neutrinos and  $\gamma$ -rays, operate as cosmic engines capable of accelerating particles (such as protons, neutrons, pions) on very high energies. The high energy (non-thermal) protons may collide with cold protons leading to emission of high energy neutrinos and gamma-rays moderated by the magnetic field [3]. In this work, we have simulated relativistic magneto-hydrodynamic (RMHD) jets' flow, for different magnetic field values using the PLUTO hydrocode [8]. By adjusting the relevant physical parameters (injection velocity, pressure and density of the jet), we study the dependence of the collimation of the outflow on the magnetic field (specifically its toroidal component) intensity in and around the jet [6, 9].

Modification of the magnetic field, allowed us to investigate its effect on the neutrino and  $\gamma$ -ray emissivity. We also examined the degree of the collimation of the flux within a chosen region of values of the initial density and injection velocity of the flux [6]. We mainly explored the role of magnetic fields in the formation and propagation of these jets by making 2-D and 3-D animations (using the PLUTO data) with the visualization and graphical analysis tools of Visit 9.1. [9].

---

\* Corresponding author, email: vaggelispaspa@hotmail.com

## THEORETICAL DETAILS

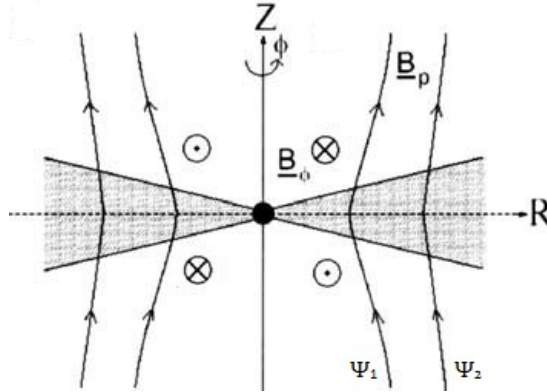


**Fig. 1.** Schematic view of the two basic components of the magnetic field. The accretion disk is presented by the shaded area around the R-axis. The central axis of the jet is the Z-axis [8].

There are two important components of the MF, the toroidal  $B_\phi$ , which follows the rotational movement of the accretion disk and the poloidal  $B_p$ , which follows the flux of the jet (Fig. 1). Hence, the magnetic field can be decomposed as,

$$\vec{B} = \vec{B}_p + B_\phi \hat{\phi} \quad (1)$$

The poloidal component can also be expressed as  $\vec{B}_p \equiv B_r \hat{r} + B_z \hat{z}$ . In terms of a scalar flux function  $\Psi$ , the poloidal equation can be written as,

$$\vec{B}_p = \vec{\nabla} \times \left( \frac{\Psi}{r} \hat{\phi} \right) = \frac{1}{r} \vec{\nabla} \Psi \times \hat{\phi} \quad (2)$$

and similarly,

$$\vec{B}_r = -\frac{1}{r} \frac{\partial \Psi}{\partial z}, \quad \vec{B}_z = \frac{1}{r} \frac{\partial \Psi}{\partial r}, \quad (3)$$

while the  $B_\phi$  is independent of the flux function  $\Psi$ .

The equation of motion for the jet flux is,

$$\rho(\vec{v} \cdot \vec{\nabla})\vec{v} = -\vec{\nabla}P - \rho\vec{\nabla}\Phi + \frac{1}{4\pi}(\vec{\nabla} \times \vec{B}) \times \vec{B}. \quad (4)$$

It can also be proved that the poloidal mass flux per unit of the poloidal magnetic field is constant along the field lines. There is also the mass load function  $\eta$ , which can be expressed in terms of the flux function  $\Psi$  as,

$$\eta(\Psi) = \frac{d\Psi_m}{d\Psi}. \quad (5)$$

Here  $d\Psi_m = \rho u_p dA$  and  $d\Psi = B_p dA$  with  $u_p \equiv |\vec{u}_p|$  being the poloidal component of the velocity. It can be proved that  $\vec{u}_p$  is parallel to the  $\vec{B}_p$ .

The angular momentum and the energy has also contributions from the magnetic field as,

$$L(\Psi) = r_A^2 \Omega(\Psi) \quad (6)$$

$$E(\Psi) = \frac{1}{2} v^2 + h + \Phi - \frac{r \Omega B_\phi}{4\pi\eta}, \quad (7)$$

where  $\Omega$  is the angular velocity, that differs in different magnetic surfaces. Equation (7) is the known Bernoulli equation for the flux, that expresses the conservation of the energy per unit mass along the poloidal field lines and function  $h$  is the specific enthalpy.

Using equation of motion (4), the Grad-Shafranov equation can also be produced as,

$$\begin{aligned} & \nabla \cdot \left[ (M_A - 1) \frac{\nabla \Psi}{4\pi r^2} \right] - (B_\phi^2 + M_A^2 B_p^2) \frac{\eta'}{4\pi\eta} \\ & = \rho \left[ E' - \Omega_m (\Omega r_A)' - (\Omega_m r^2 - \Omega r_A^2) \Omega' - \frac{\alpha_s^2}{\gamma(\gamma - 1)} K' \right]. \end{aligned} \quad (8)$$

The scalar functions  $\Psi$ ,  $E(\Psi)$ ,  $L(\Psi)$ ,  $\Omega(\Psi)$ ,  $\eta(\Psi)$  and  $K(\Psi)$ , are integrals of motion and  $M_A^2$  is the Mach-Alfvén number [2].

The rotation of the accretion disk rotates the matter around the central object of the MQ. The acceleration of the jet is supported by the accretion disk which is dominated by a perpendicular MF. The MF lines are stretched by the material that is fixed on the lines, ending up surrounding them. So, the particles of the ionized material are tight on the lines and behave like beads of a rosary. Due to the initial velocity, the inertia of the flux pushes the MF lines. Finally, the MF becomes highly toroidal and at last helical.

In the approximation of a thin disk, the rotation velocity is Keplerian and the effective potential per unit mass is,

$$\Phi_{eff} = -GM_{BH} \left[ \frac{r_0}{\sqrt{r^2 + z^2}} + \frac{1}{2} \left( \frac{r}{r_0} \right)^2 \right]. \quad (9)$$

For the launch of the jet, there must be at least one particle to be in unstable equilibrium at the point  $(r_0, 0)$ . Thus, we have to demand that the second derivative of the effective potential along the MF lines is negative.

The collimation of the jet, is achieved by a tensional force associated with the  $B_\phi$  leading to a radially inwards directed component of the Lorentz force,

$$F_{L,r} \simeq j_z B_\phi. \quad (10)$$

Due to these radial Lorentz forces acting on the jet's matter towards the jet's central axis, the outgoing flux is collimated along the same axis and vertically to the accretion disk [5]. The  $B_p$  also contributes to the jet collimation by affecting the minimum opening angle of the jet.

This magneto-hydrodynamic (MHD) theory has to be extended if the flux velocity is comparable with the velocity of light. Under these circumstances Eq. (4) becomes,

$$\rho(\vec{v} \cdot \vec{v})(\xi \vec{v}) = -\vec{v}P - \rho_e \vec{E} + \frac{\vec{j} \times \vec{B}}{c} + \gamma \rho \vec{v} \left( \xi \gamma \frac{GM_{BH}}{\sqrt{r^2+z^2}} \right), \quad (11)$$

where  $c^2 \xi$  is the relativistic enthalpy per unit mass and  $\gamma$  is the local bulk Lorentz factor of the flux.

Now, the angular momentum and energy, are conservative quantities along the poloidal MF lines. In the relativistic case, their expressions are,

$$L(\Psi) = \gamma \xi r v_\phi - \frac{r B_\phi}{4\pi\eta} \quad (12)$$

and

$$E(\Psi) = \gamma \xi \left( \frac{GM_{BH}}{\sqrt{r^2+z^2}} \right) - \frac{r \Omega B_\phi}{4\pi\eta}, \quad (13)$$

Respectively [2].

Finally, the shape of the magnetic surfaces comes out of the solution of Eq. (11) for the force balance across the poloidal field lines. Thus, the collimation may be achieved through a combination between the self-collimation and the pressure by the material that exists around the jet.

## RESULTS AND DISCUSSION

In this work, the jet's flow simulations are performed using the PLUTO astrophysical code in its relativistic magneto-hydrodynamic (RMHD) version [1].

**Tab. 1.** Values of various physical and model parameters for the simulation run [9].

Parameter		Comments
cell size ( $\times 10^{10}$ cm)	0.25	PLUTO's computational cell
$\rho_{\text{jet}}$ ( $\text{cm}^{-3}$ )	$1.0 \times 10^{11}$	initial jet matter density
$\rho_{\text{sw}}$ ( $\text{cm}^{-3}$ )	$1.0 \times 10^{12}$	stellar wind density
$\rho_{\text{adw}}$ ( $\text{cm}^{-3}$ )	$1.0 \times 10^{12}$	accretion disk wind density
$t_{\text{run}}^{\text{max}}$ (s)	$1.5 \times 10^3$	model execution time
Interpolation Method	Linear	
Integrator	MUSCL-Hancock	
EOS	Ideal	Equation of state
BinSep (cm)	$4.0 \times 10^{12}$	Binary star separation
$M_{\text{BH}}/M_{\text{sun}}$	3-10	Mass range of collapsed star
$M_{\text{star}}/M_{\text{sun}}$	10-30	Mass range of Main Seq. star
$\beta = v_0/c$	0.26	Initial jet speed
$L_{\text{k}}^{\text{p}}$	$2 \times 10^{36}$	Jet kinetic luminosity
grid resolution	$120 \times 200 \times 120$	PLUTO grid resolution (xyz)

The Generalized Lagrange Multiplier (GLM) correction method is used, enforcing magnetic divergence suppression through hyperbolic divergence cleaning, while the MUSCL-Hancock scheme is employed as the integrator [6]. The stellar wind is set to decrease away from the companion star as  $1/r^2$ , while a corona of  $1/y^2$ ,  $y$  being the jet axis direction, is setup near the compact object, respectively. The most important model parameters are shown in Tab. 1 and have

been chosen with the purpose to describe the SS-433 system. The VisIt visualization suite is then employed in order to present the results of the simulations in a graphical manner. The boundary conditions are outflow at the top and at the sides of the computational domain ("box") and reflective at the bottom where the jet base is located. The jet's ejection comes from the middle of the bottom ( $x-z$ ) plane, moving upwards along the model's  $y$ -axis.

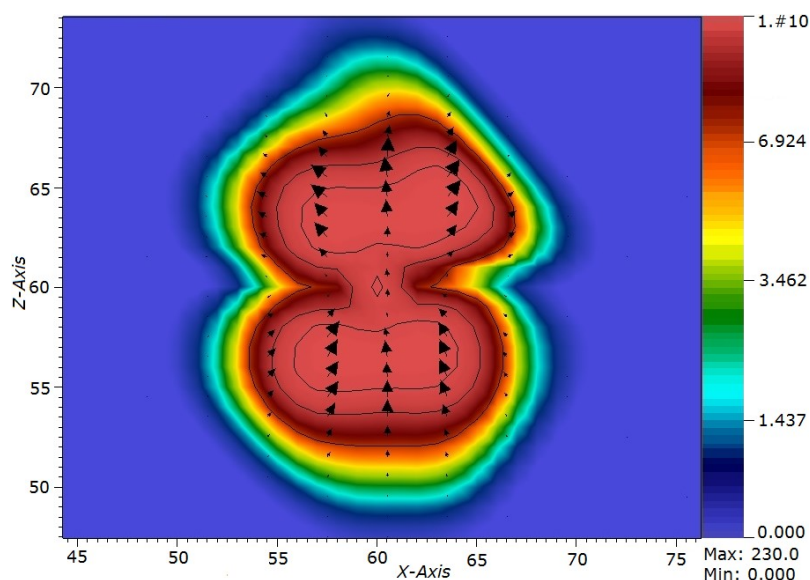


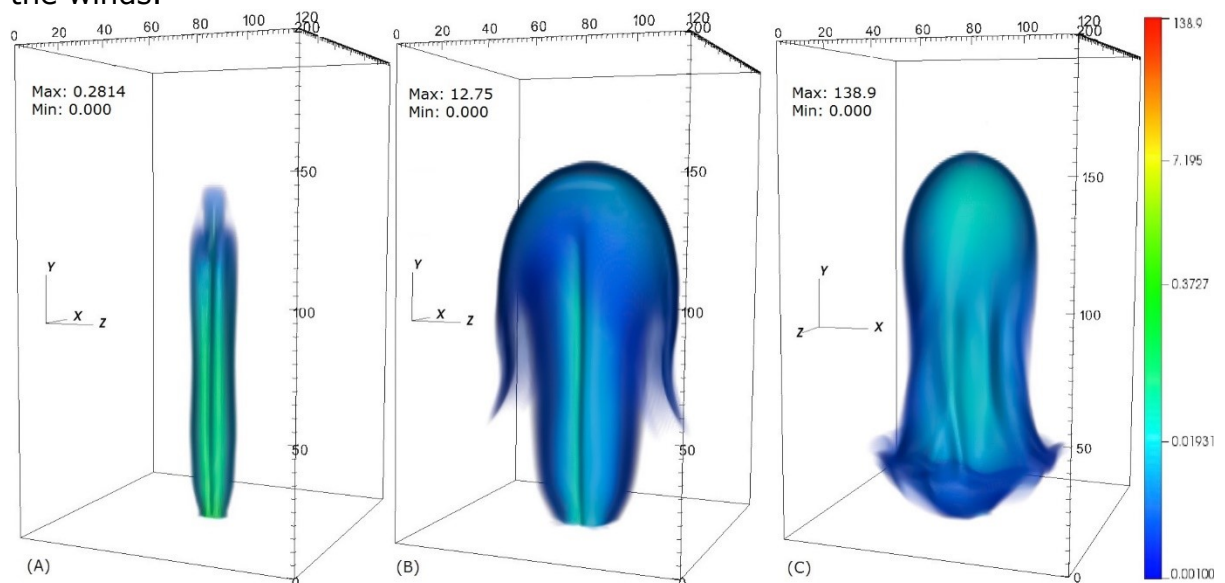
**Fig. 2.** A 2-dimensional plot of the strongest components of the jet magnetic field, in PLUTO simulation units, for a jet's cross-section, depicting a slice cut parallel to the  $x-z$  plane.

The two main components of the MF can be determined, in Fig. 2, and the presence of the toroidal component (ringwise) seems to contribute to the jets confinement through the Lorentz force. The toroidal component of the field is also significant, while other MF lines (vectors) form part of the poloidal component, especially near the jet's central axis. The color shows that the value of the MF is stronger near the same axis.

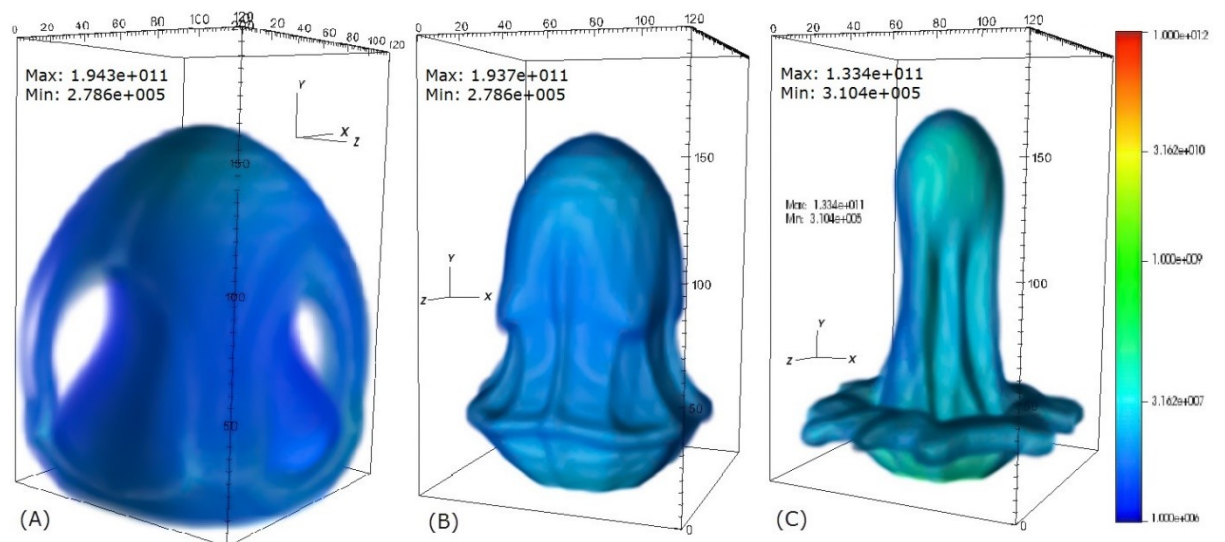
In Fig. 3 we present three different cases of the same jet's MF magnitude, roughly halfway into the simulation run. As can be seen, if we change the initial value of the MF at the base of the jet, the jet gets a different formation. In the case (A), where the initial value is 2G we see that the MF is weak and has cylindrical shape. In the case (B), where the value is 50G, we see that the same shape still exists, but now, it is covered by a larger one. The space that is occupied by the MF is larger and its value seems to decrease from the vicinity of the central axis to the outer layers. In the case (C), 500G, the MF occupies a bit smaller volume than the previous case, but the jet seems to be shaped very well and the magnitude of the MF is stronger, because the magnetic force towards the jet axis is stronger too.

Figure 4 presents the jet's mass density, at the middle of the simulation, for the same cases of the initial MF values, as in Fig. 3. We see that, when the MF is stronger, the jet is more collimated around the central axis. Moreover when the MF takes its lowest value, there is sideways flow and the jet becomes more extended. If we compare the Figs. 3 and 4, in this case, we conclude that the MF occupies a small portion of the mass density and that explains the sideways flow.

On the other hand, in the cases (B) and (C), the jet is better magnetized and demonstrates a denser flow that stays more focused and does not dissipate into the winds.



**Fig. 3.** Plots of the MF magnitude for different MF values at the base of the jet. (A) 2G, (B) 50G, (C) 500G.



**Fig. 4.** Plots of the mass density at the jet for different MF values at the base of the jet. (A) 2G, (B) 50G, (C) 500G.

## CONCLUSIONS

There is a strong dependence of the jet's collimation and neutrino emission on the magnetic field. The confinement of the flux of the jet is analogous to the magnitude of the toroidal component of the field. This mechanism intensifies the possible neutrino emission, as it allows the magnetized matter to keep dense. At the places where the matter density is high, the possibility of the reactions which lead to the neutrino emission is high as well. In that way, the field contributes to enhance the neutrino emissivity. Moreover, when the MF is strong, the sideways flow is of secondary importance and, therefore, less emission is expected from the sides of the jet. This is opposed to the weak MF case, where the jet expands more

and mixes with the ambient medium, allowing for more dynamical effects to occur over a larger volume at the jet sides. In this case, neutrino emission at vertical directions of the central axis is also expected to occur.

The combination of the results, of the simulations of the jets with theoretical predictions, of the emissivity of neutrinos and the cross sections of p-p and p- $\gamma$  collisions, using numerical methods, provides detailed investigations of the neutrino production from microquasars' jets. These methods can also be employed for gamma rays emission estimations of the jets.

## References

- [1] T. Smponias and T.S. Kosmas, MNRAS **412**, 1320-1330 (2011)
- [2] G.E. Romero and G.S. Vila, Lecture Notes in Physics **876**, (2014)
- [3] M.M. Reynoso and G.E. Romero, A&A **493**, 1-11 (2009)
- [4] I. Felix Mirabel, C. R. Physique **8**, 7-15 (2007)
- [5] R.E. Pudritz, M.J. Hardcastle and D.C. Gabuzda, Space Sci. Rev. **169**, 27-72 (2012)
- [6] M. Elizabete, Advances in Space Research **35**, 908-924 (2005)
- [7] H.R. Christiansen et. al., Phys. Rev. D **73**, 063012 (2006)
- [8] A. Mignone et al., The Astrophys. J. Suppl. Ser. **170(1)**, 228-242 (2007)
- [9] T. Smponias and O.T Kosmas, Adv. High Energy Phys. **2015**, 92757 (2015)
- [10] I.F. Mirabel, C.R. Physique **8**, 7-15 (2007)

# Speed of sound bounds and neutron star structure

Ch.C. Moustakidis, T. Gaitanos, Ch. Margaritis, and G.A. Lalazissis

*Department of Theoretical Physics, Aristotle University of Thessaloniki, 54124  
Thessaloniki, Greece*

---

## Abstract

The accurate determination of the maximum mass of the neutron stars is one of the most important tasks in Astrophysics. It is directly related with the identification of the black holes in the Universe, the production of neutron stars from the supernovae explosion and the Equation of State (EoS) of dense matter. The upper bound of the speed of sound imposes strong constraints on the maximum mass of neutron stars. However, this upper bound remains still an open issue. Recent observations, of binary neutron star systems, offer the possibility to measure with high accuracy both the mass and the tidal polarizability of the stars. We study possible effects of the upper bound of the speed of sound on the upper bound of the mass and the tidal polarizability. We conclude that this kind of measurements, combined with recent observations of neutron stars with masses close to  $2M_{\odot}$ , will provide robust constraints on the equation of state of hadronic matter at high densities.

*Key words:* Neutron stars; Nuclear equation of state; Speed of sound; Tidal polarizability.

---

The determination of the maximum mass of a neutron star (NS) (rotating and nonrotating) is one of the long-standing, important subjects in Astrophysics (for a comprehensive introduction dedicated to this problem see Ref. [1]). In particular, the identification of a black hole requires the knowledge of the maximum mass of a neutron star. The maximum neutron star mass has a considerable interest for the study of the production of neutron stars and black holes in the dynamics of supernovae explosion. Moreover, the experimental observations of neutron star masses have imposed strong constraints on the hadronic EoS of superdense matter (see also the references about the neutron star mass distribution [2,3]). The most famous examples are the recent discoveries of massive neutron stars with gravitational masses of  $M = 1.97 \pm 0.04 M_{\odot}$  (PRs J1614-2230 [4]) and  $M = 2.01 \pm 0.04 M_{\odot}$  (PSR J0348+0432 [5]). From theoretical point of view, it is well known that the exact value of the maximum mass

$M_{\max}$  of a NS depends strongly on the EoS of  $\beta$ -stable nuclear matter [6–22]. One possibility to proceed with an estimate of  $M_{\max}$  is based on the pioneering idea of Rhoades and Ruffini [10], where an optimum upper bound of mass of non-rotating neutron stars has been derived using a variational technique. Recently, Bedaque and Steiner [22] have found simple arguments that support the limit  $c/\sqrt{3}$  in non-relativistic and/or weakly coupled theories.

The main motivation of the present paper is to study in detail the limiting cases of the upper bound of the speed of sound and their effects on the bulk neutron star properties. We calculate maximum neutron star masses in relation to various scenarios for the upper bound of the speed of sound. We use a class of equation of states, which have been extensively employed in the literature and mainly have the advantage to predict neutron star masses close or higher to the experimentally observed value of  $2M_{\odot}$  [4,5]. We also extend our study to the analysis of the tidal polarizability (deformability), which can be estimated experimentally.

It is known that no bounds can be determined for the mass of non-rotating neutron stars without some assumptions concerning the properties of neutron star matter [1]. In this study, following the work of Sabbadini and Hartle [23,24] we consider the following four assumptions: (i) the matter of the neutron star is a perfect fluid described by a one-parameter equation of state between the pressure  $P$  and the energy density  $E$ , (ii) the energy density  $E$  is non negative (due to attractive character of gravitational forces), (iii) the matter is microscopically stable, which is ensured by the conditions  $P \geq 0$  and  $dP/dE \geq 0$  and (iv) below a critical baryon density  $n_0$  the equation of state is well known. The adiabatic speed of sound is defined as [25]

$$\frac{v_s}{c} = \sqrt{\left(\frac{\partial P}{\partial E}\right)_S} \quad (1)$$

where  $S$  is the entropy per baryon. In the present work we consider the following three upper bounds for the speed of sound: 1)  $\frac{v_s}{c} \leq 1$  (causality limit from special relativity (see [1] and reference therein)), 2)  $\frac{v_s}{c} \leq \frac{1}{\sqrt{3}}$  (from QCD and other theories (see [22] and reference therein)), 3)  $\frac{v_s}{c} \leq \left(\frac{E - P/3}{P + E}\right)^{1/2}$  (from relativistic kinetic theory (see [26] and reference therein)).

We construct the maximum mass configuration by considering the following structure for the neutron star EoS

$$P(E) = \begin{cases} P_{crust}(E), & E \leq E_{c-edge} \\ P_{NM}(E), & E_{c-edge} \leq E \leq E_0 \\ \left(\frac{v_s}{c}\right)^2 (E - E_c) + P_{NM}(E_0), & E_0 \leq E. \end{cases} \quad (2)$$

According to Eq. (2), the EoS yielding the maximum mass of neutron stars, is divided into three regions. In particular, above the critical energy density  $E_0$  the EoS is maximally stiff with the speed of sound  $\sqrt{\left(\frac{\partial P}{\partial E}\right)_S}$  fixed to the interval  $(1/\sqrt{3} - 1)c$ . In the intermediate region  $E_{c-edge} \leq E \leq E_0$  we employed a specific EoS which is used for various nuclear models (see below for more details), while for  $E \leq E_{c-edge}$  we used the equation of Feynman, Metropolis and Teller [27] and also of Baym, Bethe and Sutherland [28].

We use the following notations and specifications for the results of the theoretical calculations: a) the case where the critical (fiducial) density is  $n_0 = 1.5n_s$  and for  $n \geq n_0$  the speed of sound is fixed to the value  $v_s = c$  (EoS/maxstiff), b) the case where the fiducial density is  $n_0 = 1.5n_s$  and for  $n \geq n_0$  the speed of sound is fixed to the value  $v_s = c/\sqrt{3}$  (EoS/minstiff), and c) the case where the for  $n \geq n_{c-crust}$  we simple employ the selected EoS without constraints (EoS/normal).

In the present work we employed various relativistic and non-relativistic nuclear models, which are suitable to reproduce the bulk properties of nuclear matter at low densities, close to saturation density as well as the maximum observational neutron star mass (Refs. [4,5]). In the present work we include the following models: the MDI model [29], Momentum dependent relativistic mean field model [30–35], the HLPS model [36,37], the H-HJ model [38,39] and Skyrme models [40,41].

The relativistic kinetic theory also predicts an upper bound of the speed of sound, which differs from unity. In the low temperature limit  $1/kT \rightarrow \infty$  the conditions are given by the following inequalities [26,42,43]

$$E \geq 0, \quad P \geq 0, \quad (P + E) \left(\frac{v_s}{c}\right)^2 \geq 0, \quad \left(\frac{v_s}{c}\right)^2 \leq \frac{E - P/3}{P + E}, \quad P \leq 3E. \quad (3)$$

The conditions in Eqs. (3) impose stringent constraints on the high-density equation of state and thus, stringent constraints on the maximum neutron star mass. Requirement of these conditions implies that the maximally stiff equation of state fulfills the following expression

$$\left(\frac{v_s}{c}\right)^2 = \frac{E - P/3}{P + E}. \quad (4)$$

Now, the total equation of state, suitably to describe the maximum mass configuration of a neutron matter, is given by the ansatz (see again Eq. (2))

$$P(n) = \begin{cases} P_{crust}(n), & n \leq n_{c-edge} \\ P_{NM}(n), & n_{c-edge} \leq n \leq n_0 \\ C_1 n^{a_1}(a_1 - 1) + C_2 n^{a_2}(a_2 - 1), & n_0 \leq n. \end{cases} \quad (5)$$

For the equation of state in the interval  $n_{c-edge} \leq n \leq n_0$  we employed the MDI model with  $L = 110$  MeV. However, the results, especially for low values of the fiducial density  $n_0$  are model independent. It is worth to point that the condition  $\left(\frac{v_s}{c}\right)^2 \leq \frac{E-P/3}{P+E}$  is well satisfied everywhere.

Gravitational waves from the final stages of inspiraling binary neutron stars are expected to be one of the most important sources for ground-based gravitational wave detectors [44–50]. The masses of the component of the system will be determined with moderate accuracy, especially if the neutron stars are slowly spinning, during the early stage of the evolution. The tidal fields induce quadrupole moments on the neutron stars. The response of the neutron star is described by the dimensionless so-called Love number  $k_2$ , which depends on the neutron star structure and consequently on the mass and the EoS of the nuclear matter. The tidal Love numbers  $k_2$  is obtained from the ratio of the induced quadrupole moment  $Q_{ij}$  to the applied tidal field  $E_{ij}$

$$Q_{ij} = -k_2 \frac{2R^5}{3G} E_{ij} \equiv \lambda E_{ij}, \quad (6)$$

where  $R$  is the neutron star radius. The tidal Love number  $k_2$  depends on the compactness parameter  $\beta$  and the quantity  $y_R$ . Actually,  $y_R$  is determined by solving the following differential equation for  $y$

$$r \frac{dy(r)}{dr} + y^2(r) + y(r)F(r) + r^2 Q(r) = 0, \quad y(0) = 2, \quad y_R \equiv y(R) \quad (7)$$

where  $F(r)$  and  $Q(r)$  are functionals of  $E(r)$ ,  $P(r)$  and  $M(r)$  (see Ref. [47,48] for more details). The equation (7) must be integrated self consistently with the TOV equations using the boundary conditions  $y(0) = 2$ ,  $P(0) = P_c$  and  $M(0) = 0$ .

In addition, the combined tidal effects of two neutron stars in a circular orbits are given by a weighted average of the quadrupole responses  $\tilde{\lambda}$  [44,47]. The weighted average  $\tilde{\lambda}$  is usually plotted as a function of chirp mass  $\tilde{M} = (m_1 m_2)^{3/5} / M^{1/5}$  for various values of the ratio  $h = m_1 m_2 / M^2$ .

We start the discussion with Fig. 1. It shows the radius-mass relation of neutron stars using various EoS without any restriction on the speed of sound (except the relativistic one). One can see, that all hadronic models can reproduce the recent observation of two-solar massive neutron stars. In general, the stiffer EoS (at high densities) the higher the maximum neutron star mass.

In order to clarify the critical density dependence on  $M_{\max}$ , we display in Fig. 1 the dependence of the maximum mass for the chosen EoS, on the fiducial density  $n_0$ . We considered three upper bounds for the speed of sound:  $v_s = c$ ,  $v_s = c/\sqrt{3}$  and the bound originated from the kinetic theory (see Eq. (4)). First, one sees an overall reduction of the neutron star mass with increasing critical density. Using the density behavior of the  $v_s = c/\sqrt{3}$  constraint in the calculations, the neutron star mass first decreases and then approaches a constant value, which is characteristic for each EoS. It is remarkable that in all cases the neutron star mass drops below the experimental value of two solar masses (the only exception is the stiff case of the HLPS model). Therefore, the assumption of  $v_s = c/\sqrt{3}$  value as the upper limit for the speed of sound in compressed matter would exclude particular EOSs which contradict with recent astrophysical observation of massive neutron stars. On the other hand, when the causality limit  $v_s = c$  is imposed, the upper bound on the maximum mass significantly increases as is well known from previous studies and the relevant predictions (see Refs. [15,18] and references therein).

We propose now an additional approach to investigate the upper bound of  $v_s$ . In particular, we calculate for the EoSs used in this work and for the various maximum mass configurations, the corresponding values of the tidal polarizability. The tidal polarizability is an important quantity, as it can be deduced from observations on neutron star binary systems. This is shown in Fig. 2. The *signature* of the maximum mass configuration on the values of  $\lambda$  is obvious. In particular, we found that  $\lambda$  takes a wide range of values ( $\lambda \sim (1 - 5) \cdot 10^{36}$  gr cm<sup>2</sup> s<sup>2</sup>) for the employed EoS (EoS/normal case). Since  $\lambda$  is sensitive to the neutron star radius, this quantity is directly affected by the EoS. An EoS leading to large neutron star radii will also give high values for the tidal polarizability  $\lambda$  (and vice versa). The constraints of the upper bound on the speed of sound (EoS/minstiff) leads to a non-negligible increase of  $\lambda$  for high values of neutron star mass. However, in the EoS/maxstiff case the corresponding increase of  $\lambda$  is substantial, compared to the EoS/normal case. Moreover, in this case the values of  $\lambda$  remain measurable even for very high values of the mass. This behavior is due to the strong dependence of  $\lambda$  on the radius  $R$ . Specifically, according to Fig. 2 the increase of the upper bound on the speed of sound influences significantly the maximum mass configuration in two ways. First, a dramatic increase of the upper bound of  $M_{\max}$ . Second, the neutron star radius is significantly increased. A radius increase by 10% leads already to a rise of the tidal polarizability  $\lambda$  by 60%. In the same figure, the ability to measure the tidal polarizability from the Advanced LIGO and

the Einstein Telescope is indicated.

We now discuss the weighted tidal polarizability  $\tilde{\lambda}$  as a function of the chirp mass  $\tilde{M}$  varying the symmetric ratio  $h$ , as shown in Fig. 2. We consider again the main three cases (EoS/normal, EoS/minstiff, and EoS/max stiff) where for the intermediate region of the density we employ the MDI model with the slope parameter  $L = 95$  MeV. The three values of the symmetric ratio (0.25, 0.242, 0.222) correspond to the mass ratio  $m_2/m_1$  (1.0, 0.7, 0.5) (for more details see also Ref. [47]). The uncertainty  $\Delta\tilde{\lambda}$  in measuring  $\tilde{\lambda}$  of the Advanced LIGO and the corresponding of the Einstein Telescope are also presented. From Fig. 2 it is concluded that the upper bound of the speed of sound and consequently the maximum mass configuration affects appreciable the chirp mass-weighted tidal polarizability dependence. This effect is more pronounced for chirp masses  $\tilde{M} > 0.5 M_\odot$ . In particular, for high values of  $\tilde{M}$ , the Einstein telescope has the sensibility to distinguish the mentioned dependence. It is worth to point out also the moderate, but visible dependence on the symmetric ratio  $h$  in each case. This dependence is more effective for the EoS/max stiff case and for  $h = 0.222$ . That is, when the asymmetry of the two masses is very large.

We consider that it is of interest to present the results due to the relativistic kinetic theory constraints on the EoS and to compare them with the upper bounds suggested by other approaches as well as with a future relative observations. In Fig. 3 we display the mass-radius dependence when the constraints on the upper limit of the speed of sound are taken into account according the relativistic kinetic theory. We employ five values for the critical density  $n_0$ . The use of the upper bounds on the speed of sound, imposed by the kinetic theory, lead to values of  $M_{\max}$  which do explain the recent observations, even for high values of the critical density  $n_0$ . The increase of  $M_{\max}$  as well of the compactness parameter  $\beta$  leads, as in the previous cases, to a significant increase on the values of the tidal polarizability  $\lambda$ . This effect is more pronounced at high densities and, in particular, the  $\lambda$ -values are inside the sensibility of the Einstein Telescope.

We believe that the simultaneous measure of  $M$  and  $\lambda$  will help to better understand the stiffness limit of the equation of state. In particular, observations with third-generation detectors, will definitely provide constraints for the stiffness of the EoS at high density. The future detection and analysis of gravitational waves in binary neutron star systems is expected to shed light on this problem.

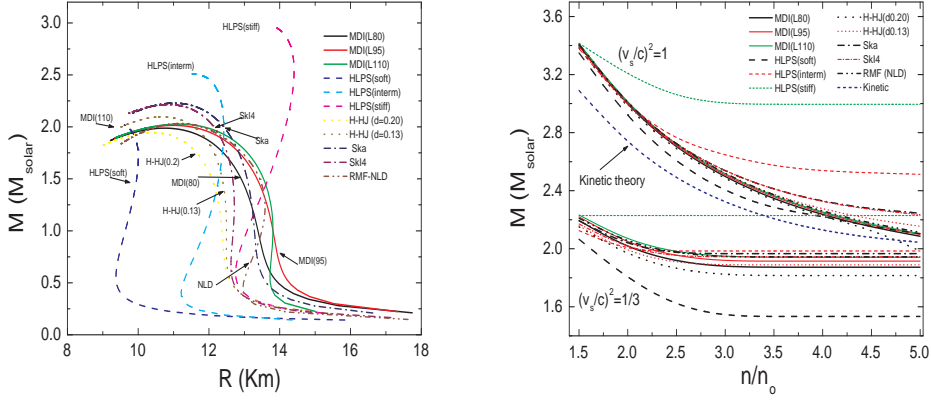


Fig. 1. Left: Mass-radius diagram for the equations of state used in the present work. Right: The maximum mass of neutron stars as function of the critical density  $n_0$  for the two upper bound for the speed of sound  $v_s = c$  and  $v_s = c/\sqrt{3}$ . The case which corresponds to the upper bound for  $v_s$ , which is taken from the kinetic theory, is also indicated.

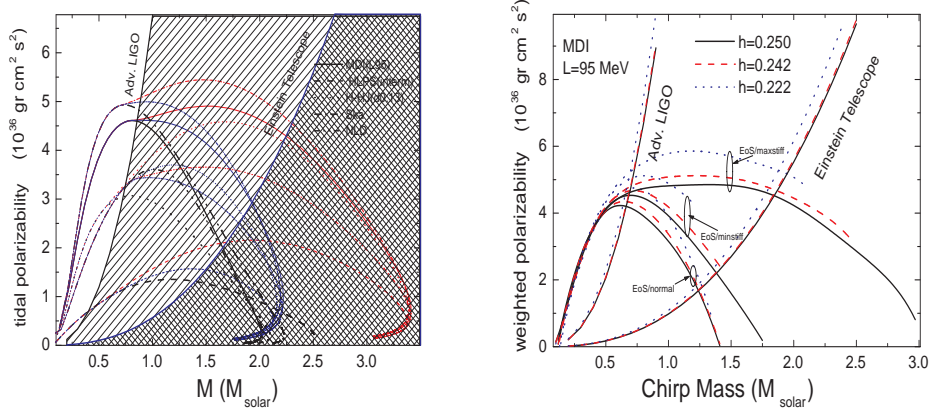


Fig. 2. Left: The tidal polarizability  $\lambda$  of a single neutron stars as function of the mass for the five selected EoS's (EoS/normal case) in comparison with the corresponding maximum mass configurations results (EoS/minstiff and EoS/maxstiff cases). The ability detection region of the Advanced LIGO is the unshaded region and the corresponding of the Einstein Telescope by the unshaded and light shaded region (see text for more details and also Ref. [47]). Right: The weighted tidal polarizability  $\tilde{\lambda}$  as function of the chirp mass  $\tilde{M}$  for various values of the symmetric ratio  $\eta$  for the three considered cases (EoS/normal, EoS/minstiff, and EoS/max stiff) which correspond to the MDI (L95) EoS. The three values of the symmetric ratio (0.25,0.242, 0.222) corresponds to the mass ratio  $m_2/m_1$  (1,0.7, 0.5) (see also Ref. [47] for comparison). The uncertainty  $\Delta\tilde{\lambda}$  in the  $\tilde{\lambda}$  measure of the Advanced LIGO is the unshaded region and the corresponding of the Einstein Telescope by the unshaded and light shaded region (see text for more details and also Ref. [47]).

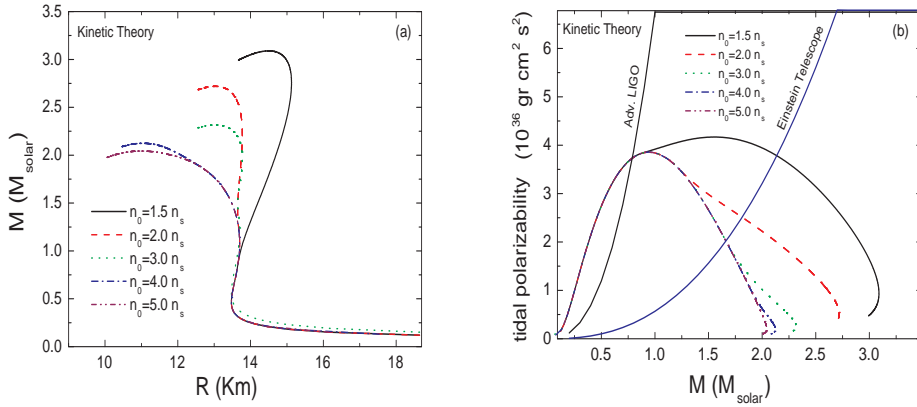


Fig. 3. (a) The mass-radius diagram which corresponds to the constraints for the relativistic kinetic theory in the  $v_s$  and for various values of the critical density  $n_0$  (see text for more details), (b) the  $M$ - $\lambda$  dependence from the kinetic theory in comparison with the observation abilities (see text for more details).

## References

- [1] J.B. Hartle, Phys. Rep. **46**, 201 (1978).
- [2] M. Coleman Miller and J.M. Miller, Phys. Rep. **548**, 1 (2015).
- [3] B. Kiziltan, A. Kottas, M.De Yoreo, and S.E. Thorsett, Astrophys. J. **778**, 66 (2013).
- [4] P. Demorest, T. Pennucci, S. Ransom, M. Roberts, and J. Hessels, Nature **467**, 1081 (2010).
- [5] J. Antoniadis, P.C. Freire, N. Wex, T.M. Tauris, R.S. Lynch, et al., Science **340**, 1233232 (2013).
- [6] S.L. Shapiro and S.A. Teukolsky, *Black Holes, White Dwarfs, and Neutron Stars* (John Wiley and Sons, New York, 1983).
- [7] N.K. Glendenning, *Compact Stars: Nuclear Physics, Particle Physics, and General Relativity*, (Springer, Berlin, 2000)
- [8] P. Haensel, A.Y. Potekhin, and D.G. Yakovlev, *Neutron Stars 1: Equation of State and Structure* (Springer-Verlag, New York, 2007).
- [9] S. Weinberg, *Gravitational and Cosmology: Principle and Applications of the General Theory of Relativity* (Wiley, New York, 1972), pages 47-52.
- [10] C.E. Rhoades and R. Ruffini, Phys. Rev. Lett. **32**, 324 (1974).
- [11] V. Kalogera and G. Baym, Astrophys. J. **470**, L61 (1996).
- [12] S. Koranda, N. Stergioulas, and J.L. Friedman, Astrophys. J. **488**, 799 (1997).

- [13] G.F. Burgio, M. Baldo, P.K. Sahu, A.B. Santra, and H.-J. Schulze, *Phys. Lett. B* **526**, 19 (2002).
- [14] H.-J. Schulze, A. Polls, A. Ramos, and I. Vidana, *Physical Review C* **73**, 058801 (2006)
- [15] J.M. Lattimer and M. Prakash, *From Nuclei to Stars*, (ed. S. Lee, p.275. Singapore: WorldScientific, 2011).
- [16] S. Gandolfi, J. Carlson, and S. Reddy, *Phys. Rev. C* **85**, 032801(R) (2012).
- [17] A. Bauswein, T. W. Baumgarte, and H.-T. Janka, *Phys. Rev. Lett.* **111**, 131101 (2013).
- [18] N. Chamel, P. Haensel, J.L. Zdunik, and A.F. Fantina, *Int. J. Mod. Phys. E*, **22** 1330018 (2013).
- [19] N. Chamel, A.F. Fantina, J.M. Pearson, and S. Goriely, *A&A* **553**, A22 (2013).
- [20] M. Dutra, O. Lourenco, and D.P. Menezes, *Phys. Rev. C* **93**, 025806 (2016).
- [21] C. Breu and L. Rezzolla, *MNRAS* **459**, 646 (2016),
- [22] P. Bedaque and A.W. Steiner, *Phys. Rev. Lett.* **114**, 031103 (2015).
- [23] A.G. Sabbadini and J.B. Hartle, *Ap. Space Sci.*, **25**, 117 (1973).
- [24] J.B. Hartle and A.G. Sabbadini, *Astrophys. J.* **213**, 831 (1977).
- [25] L.D. Landau and E.M. Lifshitz, *Fluid Mechanics* (Pergamon Oxford, 1987), pages 251-254.
- [26] T.S. Olson, *Phys. Rev. C* **63**, 015802 (2002).
- [27] R. P. Feynman, N. Metropolis and E. Teller, *Phys. Rev.* **75**, 1561 (1949).
- [28] G. Baym, C. Pethick and P. Sutherland, *Astrophys. J.* **170**, 299 (1971).
- [29] Madappa Prakash, I. Bombaci, Manju Prakash, P. J. Ellis, J. M. Lattimer, and R. Knorren, *Phys. Rep.* 280, 1 (1997).
- [30] H.-P. Duerr, *Phys. Rev.* **103**, 469 (1956).
- [31] J. Walecka, *Annals Phys.* **83**, 491 (1974).
- [32] B. D. Serot and J. D. Walecka, *Int. J. Mod. Phys. E* **6**, 515 (1997).
- [33] D. Vreternar, A.V. Afanasjev, G.A. Lalazissis, and P. Ring, *Phys. Rep.* 409, 101 (2005).
- [34] T. Gaitanos and M. M. Kaskulov, *Nucl. Phys. A* **899**, 133 (2013).
- [35] T. Gaitanos and M. Kaskulov, *Nucl. Phys. A* **940**, 181 (2015).
- [36] K. Hebeler, J.M. Lattimer, C.J. Pethick, and A. Schwenk, *Phys. Rev. Lett.* **105**, 161102 (2010).

- [37] K. Hebeler, J.M. Lattimer, C.J. Pethick, and A. Schwenk, *Astrophys. J.* **773**, 11 (2013).
- [38] H. Heiselberg and M. Hjorth-Jensen, *Phys. Rep.* **328**, 237 (2000).
- [39] H. Heiselberg and M. Hjorth-Jensen, *Astrophys. J.* **525**, L45 (1999).
- [40] E. Chabanat, P. Bonche, P. Haensel, J. Meyer and R. Schaeffer, *Nucl. Phys. A* **627**, 710 (1997).
- [41] M. Farine, J.M. Pearson and F. Tondeur, *Nucl. Phys. A* **615**, 135 (1997).
- [42] W. Israel, *Ann. Phys. (N.Y.)* **100**, 310 (1976).
- [43] W. Israel and J.M. Stewart, *Ann. Phys. (N.Y.)* **118**, 341 (1979).
- [44] E.E. Flanagan and T. Hinderer, *Phys. Rev. D* **77**, 021502 (2008).
- [45] T. Hinderer, *Astrophys. J.* **677**, 1216 (2008).
- [46] T. Damour and A. Nagar, *Phys. Rev. D* **80**, 084035 (2009).
- [47] T. Hinderer, B.D. Lackey, R.N. Lang, and J.S. Read, *Phys. Rev. D* **81**, 1230161 (2010).
- [48] S. Postnikov, M. Prakash, and J.M. Lattimer, *Phys. Rev. D* **82**, 024016 (2010).
- [49] F.J. Fattoyev, J. Carvajal, W.G. Newton, and B.A. Li, *Phys. Rev. C* **87**, 015806 (2013).
- [50] B.D. Lackey and L. Wade, *Phys. Rev. D* **91**, 043002 (2015).

# SU(3) symmetry in deformed nuclei

Andriana Martinou\*, I. E. Assimakis, Dennis Bonatsos

*Institute of Nuclear and Particle Physics, National Center for Scientific Research  
"Demokritos", Athens, Greece*

---

## Abstract

An approximate SU(3) symmetry appears in heavy deformed even-even nuclei. In each nuclear shell with  $N \geq 3$ , due to the spin orbit interaction, one set of orbitals has escaped to the lower shell and another has intruded from the upper shell. There is an one-to-one correspondence between the orbitals of the two sets, based on pairs of orbitals which have identical quantum numbers of orbital angular momentum, spin, and total angular momentum, but different size. Such relevant orbitals have Nilsson number differences  $\Delta K[\Delta N \Delta n_z \Delta \Lambda] = 0[110]$ . By omitting the intruder Nilsson orbital of highest total angular momentum and replacing the rest of the intruder orbitals by their relevant counterparts, an approximate SU(3) symmetry is reconstructed.

*Keywords:* SU(3) symmetry, Nilsson model, heavy deformed nuclei

---

As remarked by Ben Mottelson [1] on the occasion of the 50th anniversary of the Nilsson model [2, 3], the asymptotic quantum numbers of the Nilsson model can be seen as a generalization of Elliott's SU(3) [4, 5], applicable to heavy deformed nuclei. Working along this line, we find that a hidden approximate SU(3) symmetry of the Elliott type can be uncovered in heavy deformed nuclei. In order to achieve this, we take advantage of the largely overlapping  $\Delta K[\Delta N \Delta n_z \Delta \Lambda] = 0[110]$  pairs, which have been found to play a key role in the development of nuclear deformation within a different context [6, 7, 8]. The steps taken are listed here, using a specific example.

---

\*e-mail:amartinou@hotmail.com

1) The 50-82 nuclear shell consists of the  $3s_{1/2}$ ,  $2d_{3/2}$ ,  $2d_{5/2}$ , and  $1g_{7/2}$  orbitals, which are the pieces of the full sdg shell remaining after the spin-orbit force lowering of the  $1g_{9/2}$  orbitals down into the 28-50 nuclear shell. In addition, it contains the  $1h_{11/2}$  orbitals, lowered into it from the pfh shell by the spin-orbit force.

2) The  $1h_{11/2}$  orbital consists of the Nilsson orbitals  $1/2[550]$ ,  $3/2[541]$ ,  $5/2[532]$ ,  $7/2[523]$ ,  $9/2[514]$ , and  $11/2[505]$ . As a first step in the approximation, in the 50-82 shell we omit the  $11/2[505]$  orbital, i.e. the one with the highest total angular momentum, which, as one can see in the Nilsson diagrams [2, 3], lies at the very top of the 50-82 shell, thus its influence on the structure of the rest of the shell is expected to be minimal.

3) The  $1g_{9/2}$  orbital consists of the Nilsson orbitals  $1/2[440]$ ,  $3/2[431]$ ,  $5/2[422]$ ,  $7/2[413]$ ,  $9/2[404]$ , which are  $0[110]$  partners of the remaining  $1h_{11/2}$  Nilsson orbitals listed in 2), in the same order. A pair of  $0[110]$  partners shares exactly the same values of the orbital angular momentum, spin, and total angular momentum quantum numbers, i.e. it is expected to exhibit identical behavior as far as angular momentum related properties are concerned. This has been corroborated by calculating overlaps of orbitals in Ref. [7]. One can then think of replacing in the 50-82 shell the remaining  $1h_{11/2}$  orbitals by their  $1g_{9/2}$  counterparts and checking numerically the accuracy of this approximation, taking carefully into account that during this replacement the  $N$  and  $n_z$  quantum numbers have been changed by one unit each, while the parity has changed sign.

4) After these two approximations have been made, we are left with a collection of orbitals which is exactly the one of the full sdg shell. The sdg shell of the spherical harmonic oscillator is known to possess the  $U(15)$  symmetry, having an  $SU(3)$  subalgebra [9], therefore we can expect that some of the  $SU(3)$  features would appear within the approximate scheme. Of course one should bear in mind that in axially symmetric deformed nuclei the relevant symmetry is not spherical, but cylindrical [10]. Therefore the relevant algebras are not  $U(N)$  Lie algebras, but more complicated versions of deformed algebras, in which, among

the angular momentum operators, only the  $L_z$  operator has the same physical content as the  $L_z$  operator in the Nilsson model [10].

5) The same procedure can be applied to the 28-50, 82-126, 126-184 shells, leading to approximate pf, pfh, sdgi shells, corresponding to U(10), U(21), U(28) algebras having SU(3) subalgebras (see [9] and references therein).

The consequences of the approximate SU(3) symmetry will be considered in subsequent work. A first step can be seen in [11].

## References

- [1] B. Mottelson, Phys. Scr. **T125** (2006) editorial.
- [2] S. G. Nilsson, Mat. Fys. Medd. K. Dan. Vidensk. Selsk. **29** (1955) no. 16.
- [3] S. G. Nilsson and I. Ragnarsson, Shapes and Shells in Nuclear Structure (Cambridge University Press, Cambridge, 1995).
- [4] J. P. Elliott, Proc. Roy. Soc. Ser. A **245** (1958) 128.
- [5] J. P. Elliott, Proc. Roy. Soc. Ser. A **245** (1958) 562.
- [6] R. B. Cakirli, K. Blaum, and R. F. Casten, Phys. Rev. C **82** (2010) 061304(R).
- [7] D. Bonatsos, S. Karampagia, R. B. Cakirli, R. F. Casten, K. Blaum, and L. Amon Susam, Phys. Rev. C **88** (2013) 054309.
- [8] D. Bonatsos, I. E. Assimakis, and A. Martinou, Bulg. J. Phys. **42** (2015) 439.
- [9] D. Bonatsos and A. Klein, Ann. Phys. (NY) **169** (1986) 61.
- [10] D. Bonatsos, C. Daskaloyannis, P. Kolokotronis, and D. Lenis, arXiv: hep-th/9411218.
- [11] I. E. Assimakis, A. Martinou, and D. Bonatsos, these proceedings.

# New coupling scheme in heavy nuclei

I. E. Assimakis\*, Andriana Martinou, Dennis Bonatsos

*Institute of Nuclear and Particle Physics, National Center for Scientific Research  
"Demokritos", Athens, Greece*

---

## Abstract

The dynamical SU(3) symmetry present in heavy deformed nuclei can be described by a new coupling scheme, which considers the  $\Delta K[\Delta N \Delta n_z \Delta \Lambda] = 0[110]$  Nilsson "partner" orbitals. In order to describe the properties of a given nucleus, it is necessary to identify the U(n) symmetries corresponding to the proton and neutron valence shells of the nucleus, their irreducible representations (irreps), and the SU(3) irreps contained in each of them. Once this is accomplished, a Hamiltonian can be created, containing the Casimir operators of the proper Lie algebras. The calculation of the eigenvalues of the Casimir operators in a given irrep is a solved group theoretical problem. However, one has further to include the three-body operator  $\Omega$  and/or the four body operator  $\Lambda$ , which will break the degeneracies among bands belonging to the same SU(3) irrep, without breaking the SU(3) symmetry. The calculation of the eigenvalues of the  $\Omega$  and  $\Lambda$  operators for nontrivial SU(3) irreps is a formidable group theoretical problem, receiving attention.

*Keywords:* SU(3) symmetry, higher order terms, heavy deformed nuclei

---

In the new approximate SU(3) coupling scheme [1, 2, 3, 4], the Hamiltonian should be composed by terms which are SO(3) scalars. Within SU(3), it is known [5] that five scalars exist in total

1) The second order Casimir operator of SO(3),  $\hat{L}^2$ , having eigenvalues  $I_2(L) = L(L + 1)$ .

---

\*e-mail:ioasimakis@gmail.com

2) The second order Casimir operator of SU(3), having eigenvalues

$$C_2(\lambda, \mu) = (\lambda^2 + \mu^2 + \lambda\mu + 3\lambda + 3\mu)/9.$$

3) The third order Casimir operator of SU(3), having eigenvalues

$$C_3(\lambda, \mu) = (\lambda - \mu)(2\lambda + \mu + 3)(\lambda + 2\mu + 3)/162.$$

4) The third order O(3) scalar shift operator  $O_l^0$ , called  $\Omega$  in the nuclear physics literature. For  $(\lambda, 0)$  irreps its eigenvalues are  $\Omega = \sqrt{6}L(L+1)(2\lambda+3)$ , for  $(\lambda, 2)$  irreps and  $L=0$  one has  $\Omega = 0$ , while for  $(\lambda, 2)$  irreps and  $L=\text{odd}$  they are  $\Omega = \sqrt{6}[L(L+1)-12](2\lambda+5)$ , while for  $(\lambda, 2)$  irreps and  $L=\text{even}$  one has  $\Omega = \sqrt{6}[(L-2)(L+3)(2\lambda+5) \pm 6\sqrt{L(L+1)(L-1)(L+2)+(2\lambda+5)^2}]$ .

5) The fourth order O(3) scalar operator  $Q_l^0$ , called  $\Lambda$  in the nuclear physics literature. For  $(\lambda, 0)$  irreps its eigenvalues are

$$\Lambda = 2L(L+1)[4\lambda^2 + 12\lambda - 6L(L+1) - 27],$$

while for  $(\lambda, 2)$  irreps and  $L=0$  one has  $\Lambda = 0$ . For  $(\lambda, 2)$  irreps and  $L=\text{odd}$  the eigenvalues are

$$\Lambda = 2[L(L+1)-12](4\lambda^2 + 20\lambda - 12) + [-12L^2(L+1)^2 + 98L(L+1) - 960],$$

while for  $(\lambda, 2)$  irreps and  $L=\text{even}$  [6] one has

$$\Lambda = 2[(L-2)(L+3)(2\lambda+5)^2 - 6(L^2+L+1)(L^2+L+3)] \\ \pm 12\sqrt{(2\lambda+5)^4 + 2(2L^4 + 4L^3 - 8L^2 - 10L + 3)(2\lambda+5)^2 + 9(2L+1)^2}.$$

Including only one-body and two-body terms one ends up with a Hamiltonian with eigenvalues  $E = \alpha L(L+1) + \beta C_2(\lambda, \mu)$ . In this scheme, all bands exhibit the pure rotational behavior  $L(L+1)$ , while bands belonging to the same irrep are degenerate. This is the scheme appearing in the framework of the Interacting Boson Approximation model [7]. In the present coupling scheme it does not suffice, since the levels of the  $\gamma_1$  band with even  $L$  would be degenerate with the levels of the ground state band.

Including terms up to the third order, one ends up with a Hamiltonian with eigenvalues  $E = \alpha L(L+1) + \beta C_2(\lambda, \mu) + \gamma\Omega + \delta C_3(\lambda, \mu)$ . The  $\Omega$  term breaks the degeneracy between the levels of the  $\gamma_1$  band with even  $L$  and the levels of the ground state band. Therefore this is the lowest order Hamiltonian which can be used in the framework of the present coupling scheme. The  $C_3(\lambda, \mu)$  has no practical importance, since it only influences the bandheads, and can be

omitted.

Including terms up to the fourth order, one ends up with a Hamiltonian with eigenvalues  $E = \alpha L(L+1) + \beta C_2(\lambda, \mu) + \gamma \Omega + \delta C_3(\lambda, \mu) + \xi \Lambda + \nu L^2(L+1)^2 + \tau L(L+1)C_2(\lambda, \mu) + \rho [C_2(\lambda, \mu)]^2$ . The  $C_3(\lambda, \mu)$  term, as well as the  $L(L+1)C_2(\lambda, \mu)$  and  $[C_2(\lambda, \mu)]^2$  terms, are expected to have no practical importance, and can be omitted.

For the present coupling scheme we will also need the eigenvalues for irreps with  $\mu \geq 4$ . Their calculation [8, 9, 10] is receiving attention.

## References

- [1] R. B. Cakirli, K. Blaum, and R. F. Casten, Phys. Rev. C **82** (2010) 061304(R).
- [2] D. Bonatsos, S. Karampagia, R. B. Cakirli, R. F. Casten, K. Blaum, and L. Amon Susam, Phys. Rev. C **88** (2013) 054309.
- [3] D. Bonatsos, I. E. Assimakis, and A. Martinou, Bulg. J. Phys. **42** (2015) 439.
- [4] A. Martinou, I. E. Assimakis, and D. Bonatsos, these proceedings.
- [5] G. Vanden Berghe, H. E. De Meyer, and P. Van Isacker, Phys. Rev. C **32** (1985) 1049.
- [6] J. Vanthournout, Phys. Rev. C **41** (1990) 2380.
- [7] F. Iachello and A. Arima, *The Interacting Boson Model* (Cambridge University Press, Cambridge, 1987).
- [8] J. W. B. Hughes, J. Phys. A: Math., Nucl. Gen. **6** (1973) 281.
- [9] B. R. Judd, W. Miller Jr., J. Patera, and P. Winternitz, J. Math. Phys. **15** (1974) 1787.
- [10] H. De Meyer, G. Vanden Berghe, and J. Van der Jeugt, J. Math. Phys. **26** (1985) 3109.

# Multi-strangeness production in hadron induced reactions

T. Gaitanos<sup>1,\*</sup>, Ch. Moustakidis<sup>1</sup>, G.A. Lalazissis<sup>1</sup>, H. Lenske<sup>2,3</sup>

<sup>1</sup> *Dept. of Physics, Aristotle University of Thessaloniki, 54124 Thessaloniki, Greece*

<sup>2</sup> *Institut für Theoretische Physik, Universität Giessen, D-35392 Giessen, Germany*

<sup>3</sup> *GSI Helmholtzzentrum für Schwerionenforschung, D-64291 Darmstadt, Germany*

---

## Abstract

We discuss the formation and propagation of multi-strangeness particles in reactions induced by hadron beams relevant for the forthcoming experiments at FAIR. We give particular attention in the dynamical properties of the decuplet-particle  $\Omega$  and study the production and propagation mechanism of this heavy hyperon inside hadronic environments. The transport calculations show the possibility of  $\Omega$ -production, which can be achieved with measurable  $\Omega$ -production cross sections using high-energy secondary  $\Xi$ -beams. This study is important in understanding the hyperon-nucleon and, in particular, the hyperon-hyperon interactions also in the high-strangeness sector. We emphasize the importance of our studies for neutron star physics and for the research plans at FAIR.

*Keywords:*  $\bar{P}$ ANDA,  $\bar{p}$ -induced reactions,  $\Xi$ -induced reactions, multi-strangeness hypernuclei,  $\Xi$ N interactions,  $\Omega$ -production.

---

## 1. Introduction

Reactions induced by heavy-ion and hadron beams build the theoretical and experimental framework to look deeper inside the hadronic equation of state (EoS). Of particular interest is the strangeness sector of the EoS. Baryons with strangeness degree of freedom modify the nuclear EoS significantly at compres-

---

\*e-mail:tgaitano@auth.gr

sions beyond saturation [1, 2, 3, 4, 5, 6]. However, such effects show up already in finite nuclei. Adding hyperons to a nucleus typically leads to a rearrangement of the whole system[7]. This leads to observable effects in hypernuclei. It help us to determine the hyperon-nucleon (and hyperon-hyperon) in-medium interactions at densities of ordinary matter. On the other hand, these in-medium interactions involving hyperons are also crucial at densities beyond saturation. A prominent example are compact neutron stars. The high values of energy densities inside such a star make the formation of hyperons possible, even if their masses are much higher than the nucleonic ones.

The hyperonic in-medium properties can be studied in terrestrial laboratories. In fact, reactions induced by antiproton beams on nuclear targets provide the best environment to form, detect and study the properties of hyperons inside highly excited hadronic matter. In this work we discuss the formation mechanisms of strangeness production in such reactions. We use the well-known relativistic Boltzmann-type transport equation for the theoretical simulations of in-medium hadronic reactions. Emphasis is given to the heaviest  $\Omega$ -hyperon. This baryon is particularly interesting because it consists of three strange quarks, that is, its strangeness is  $S = -3$ . Thus, secondary  $\Omega$ -rescattering could be used for the production of multi-strangeness bound systems, such as double- $\Lambda$  or  $\Xi$  hypernuclei.

## 2. Theoretical description

The theoretical framework of our studies is based on the relativistic Boltzmann-equation as realized in the GiBUU transport model [8]. The GiBUU equation reads as

$$\left[ k^{*\mu} \partial_\mu^x + (k_\nu^* F^{\mu\nu} + m^* \partial_x^\mu m^*) \partial_\mu^{k^*} \right] f(x, k^*) = \mathcal{I}_{coll}. \quad (1)$$

It gives the time evolution of the 1-body phase-space density  $f(x, k^*)$  for the various hadrons under the influence of a hadronic mean-field (l.h.s. of Eq. (1)) and binary collisions (r.h.s. of Eq. (1)). The hadronic potential shows up in the transport equation through the kinetic 4-momenta  $k^{*\mu} = k^\mu - \Sigma^\mu$  and effective

(Dirac) masses  $m^* = M - \Sigma_s$  with in-medium self-energies  $\Sigma^\mu = g_\omega \omega^\mu + \tau_3 g_\rho \rho_3^\mu$  and  $\Sigma_s = g_\sigma \sigma$  ( $\tau_3 = \pm 1$  for protons and neutrons, respectively). For the model parameters (obvious meson-nucleon couplings) we use the *NL3*-parametrization, which includes non-linear self-interactions of the  $\sigma$  field [9]. The meson-hyperon couplings at the mean-field level are obtained from the nucleonic sector using simple quark-counting arguments.

Important for captured  $\Omega$ -particles inside nuclear matter are secondary scattering processes. These are modeled within the collision term, which includes all necessary binary processes for (anti)baryon-(anti)baryon, meson-baryon and meson-meson scattering and annihilation [8]. For more details of the corresponding mean-field and cross section parameters we refer to Refs. [10, 11, 12, 13, 14, 15].

### 3. Results and Discussion

We have performed transport calculations for antiproton-induced reactions including the second-step process of  $\Xi^-$ -collisions on a secondary nuclear target. We have used two different target nuclei,  $^{93}\text{Nb}$  and  $^{64}\text{Cu}$  for the  $\bar{p}$ - and  $\Xi$ -induced reactions, respectively. For the antiproton-nucleus reactions a heavier target is used to increase the rare  $\Omega$ -production via secondary scattering, while in the  $\Xi$ -induced reactions a lighter target is sufficient for the same purpose.

Fig. 1 shows the results of the transport calculations in terms of rapidity spectra of various produced hyperons for  $\bar{p}$ -induced reactions at different beam energies. We observe an abundant production of the lightest hyperon ( $\Lambda$ ) with a broad spectral distribution in longitudinal momentum followed by the production of the cascade particles. The big differences in their production yields arise from the smaller annihilation cross section into cascade particles relative to that into the  $\Lambda\bar{\Lambda}$ -channel. Note that here secondary re-scattering is mainly responsible for the breadth of the rapidity spectra. It causes the capture of these hyperons inside the target nucleus ( $\Lambda_{bound}$  and  $\Xi_{bound}$  rapidity yields) with the sub-sequential formation of  $\Lambda$ -hypernuclei. We do not go into further details

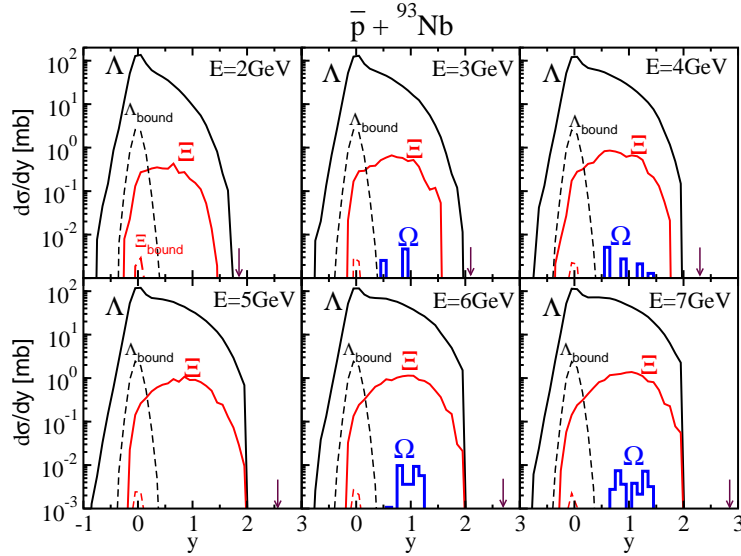


Figure 1: Rapidity distributions for various hyperons (as indicated) produced in  $\bar{p} + {}^{93}\text{Nb}$  reactions at antiproton-beam energies as shown in the panels. For the  $\Lambda$  and  $\Xi$  hyperons also the corresponding yields of them are displayed (dashed curves), which are bound inside the nucleus. The vertical arrows at each panel indicate the rapidity value of the corresponding beam-energy.

concerning the formation of hypernuclei. This task has been studied in the past in detail in previous works [16].

We focus now on the formation of the heavy  $\Omega$ -hyperon. It can be seen in Fig. 1 that the  $\Omega$ -production is a very rare process in antiproton-induced reactions at beam energies just close to the  $\Omega$ -production threshold of  $\sqrt{s} \simeq 3.344$  GeV. Note that we have analyzed around 4 millions of transport-theoretical events for each incident energy. The main reason for the low production yields of the  $\Omega$ -baryon is the extremely low annihilation cross section of several nb only. This value is far below the annihilation cross section of other exclusive processes. The major contribution to the annihilation cross section comes from multiple meson production [17]. It is important to note that the origin of the produced  $\Omega$ -particles isn't  $p\bar{p}$ -annihilation, but other secondary processes involving rescattering between antikaons, antikaonic resonances with hyperonic resonances ( $Y^*(S = -1)$ ). For instance, for the reaction  $\bar{p} + {}^{93}\text{Nb}$  at 4 GeV incident energy these secondary scattering processes contribute with a cross section of 1.148 nb to the total  $\Omega$ -production cross section of  $\sigma_{\Omega} = 1.15$  nb. The cascade particles and their resonances carries already a strangeness value of  $S = -2$ . Thus, one would expect that they preferably contribute to the  $\Omega$ -formation. This is

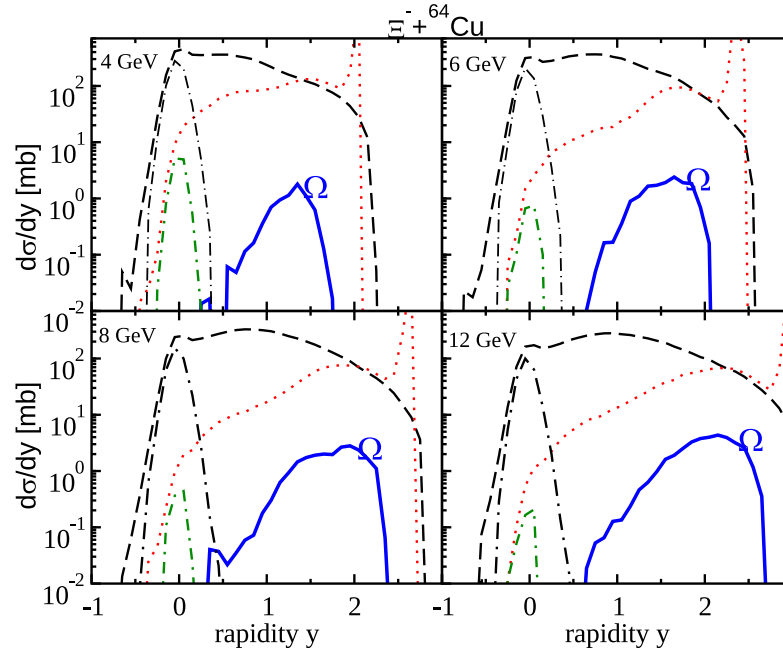


Figure 2: Rapidity distributions of different hyperons for  $\Xi$ -induced reactions on  $^{64}\text{Cu}$ -targets at four beam-energies, as indicated in each panel. Dotted curve:  $\Xi^-$ , dashed curve:  $\Lambda^-$ , dott-dashed curve: bound  $\Lambda^-$ , dot-dot-dashed curve: bound  $\Xi^-$ , thick solid curve:  $\Omega$ -rapidity spectra.

not the case, just because the  $\Xi$ -particles mainly escape the target nucleus.

The realization of a second target using the produced cascade particles as a secondary beam is important. At first, for the copious production of multi-strangeness hyperons and multi-strangeness hypernuclei, as proposed by the  $\bar{\text{P}}\text{ANDA}$  -experiment [18, 19]. According to the  $\bar{\text{P}}\text{ANDA}$  -proposal low-energy  $\Xi$ -beams will be used for the production of  $\Lambda\Lambda$ -hypernuclei. First theoretical predictions on such exotic hypermatter in low-energy  $\Xi$ -induced reactions have been indeed reported in Ref. [16]. Not only  $\Lambda\Lambda$ -hypernuclei, but also the direct formation of  $\Xi$ -hypermatter is accessible depending on the cascade-nucleon interaction [16].

We show now that the same experiment can be used to explore the formation of  $\Omega$ -baryons. This decuplet-hyperon is heavy causing high production thresholds. As discussed above, secondary re-scattering including intermediate production of high-mass hyperonic resonances can be a more favorable possi-

bility for  $\Omega$ -production. Due to the high strangeness value of this baryon the entrance channel should have as high as possible strangeness degree. Thus, the  $\bar{P}$ ANDA -experiment with the secondary  $\Xi$ -beam can be a good candidate for our purpose. This is shown in Fig. 2 in terms of the rapidity spectra, but now for  $\Xi$ -induced reactions at higher incident energies just above the  $\Omega$ -production threshold. At first, similar dynamic effects are observed for the  $\Lambda$ -hyperons as in the  $\bar{p}$ -induced reactions. They show the expected broad spectrum in rapidity (dashed curves) due to the enhanced multiple re-scattering. Latter causes also here their abundant capture inside the target nucleus, as shown by the dotted-dashed curves. The rapidity distributions of the cascade particles (dotted curves) are obviously peaked around the beam-value, but there is a significant contribution to lower rapidities too. This feature is again due to the secondary scattering, as discussed in previous works [16]. The production of bound cascade hyperons (dotted-dotted-dashed curves) is now enhanced. This effect induces the formation of exotic  $\Xi$ -hypernuclei (for more details on this task see Ref. [16]).

The most interesting part is the thick-solid curves in Fig. 2, which show the rapidity yields of the produced  $\Omega$ -baryons. The formation dynamics of the decuplet-particles here is similar to the dynamical production of the cascade particles in  $\bar{p}$ -induced reactions (for comparison see Fig. 1 again). However, the peak of the rapidity spectra of the  $\Omega$  baryons is now located to much higher energies. In particular, the probability of bound  $\Omega$ -particles inside the residual nucleus is very low. These different dynamical formations between the  $\Xi$ - and  $\Omega$ -particles have physical reasons beyond the trivial ones (slightly different target masses and beam-energies). The decuplet particles are much heavier and carry one additional strangeness degree of freedom. Latter property causes multi-particle final states in many secondary processes of  $\Omega$ -production due to strangeness conservation. For instance, in binary collisions between the cascade-beam with other nucleons three final-state particles are required to conserve strangeness and baryon numbers. This leads to rather high threshold energies. The  $\Omega$ -production thresholds are also high in other secondary processes

between the abundantly produced antikaons  $K^-(S = -1)$  with hyperons or hyperonic resonances  $\Lambda, \Sigma, Y^*(S = -1)$ . Thus, the  $\Omega$ -particles are produced with relatively high energies. The probability of secondary  $\Omega$ -scattering is low and they escape most likely the nucleus. Another interesting result is, that the  $\Omega$ -formation is pronounced largely in  $\Xi$ -nucleus collisions relative to the antiproton-induced reactions. In fact, the  $\Omega$ -production cross sections are in the range between 0.7 – 3.5 mb for the incident  $\Xi$ -energies under consideration. This arises from the rather high cross section values of secondary scattering ranging in the mb-region, as discussed in detail in Ref. [20].

#### 4. Summary

We have studied the elementary processes leading to the formation of  $\Omega$ -hyperons. The primary channel consists of  $N\bar{N}$ -annihilation into  $\Omega\bar{\Omega}$ , for which theoretical estimations exist in the literature. The predicted  $N\bar{N} \rightarrow \Omega\bar{\Omega}$ -cross sections are too small with respect to other annihilation processes. In particular, the elementary  $\Omega$ -production cross sections take values of a few nb only, which is approximately six orders of magnitude less than the nucleon-antinucleon annihilation into mesons. On the other hand, secondary re-scattering between antikaons and strangeness resonances occurs with much higher probability in the mb-regime. Therefore, in  $\bar{p}$ -nucleus reactions the formation probability of  $\Omega$ -particles is a very rare process with the prediction of a few nb only.

Our calculations, however, support the two-step reaction mechanism at  $\bar{P}$ ANDA for the observation of  $\Omega$ -hyperons. A high energetic  $\Xi$ -beam was utilized to overcome the high  $\Omega$ -production thresholds. The most important result was the formation of the  $\Omega$ -particles in  $\Xi$ -nucleus collisions with an observable probability. It is still an open question how the  $\Omega^-$ -hyperon can be observed experimentally probably by requiring reconstruction from coincidence experiments and particle correlations. However, the production cross sections in the mb-region, as estimated from the present analysis, indicate a high production rate. It would be a challenge to explore such hadron-nucleus reactions experimentally too. It

will be important to constraint better the physical picture of multi-strangeness elementary processes.

We conclude with pointing out the great opportunity of the future activities at FAIR to understand deeper the still little known high strangeness sector of the hadronic equation of state. Note that the strangeness sector of the baryonic equation of state is crucial for our knowledge in nuclear and hadron physics and astrophysics. For instance, hyperons in nuclei do not experience Pauli blocking within the Fermi-sea of nucleons. Thus they are well suited for explorations of single-particle dynamics. In highly compressed matter in compact neutron stars the formation of particles with strangeness degree of freedom is energetically allowed. Of particular interest are hereby the  $\Lambda$ -,  $\Sigma$ -,  $\Xi$ - and  $\Omega$ -hyperons with strangeness  $S=-1, -2$  and  $-3$ , respectively. As shown in recent studies [4, 21, 22], these hyperons modify the stiffness of the baryonic EoS at high densities considerably leading to the puzzling disagreement with recent observations of neutron stars in the range of 2 solar masses.

### Acknowledgement

Supported in part by DFG, contract Le439/9, BMBF, contract 05P12RGFTE, GSI Darmstadt, and Helmholtz International Center for FAIR.

### References

### References

- [1] I. Sagert, *et al.*, Phys. Rev. Lett. 102 (2009) 081101.
- [2] S. Weissenborn, D. Chatterjee, J. Schaffner-Bielich, Phys.Rev. C85 (2012) 065802, Phys.Rev. C90 (2014) 019904.
- [3] J. Schaffner-Bielich, A. Gal, Phys. Rev. C62 (2000) 034311.
- [4] J. Schaffner-Bielich, I.N. Mishustin, Phys. Rev. C53 (1996) 1416.
- [5] P. Demorest, *et al.*, Nature 467 (2010) 1081.

- [6] J. Antoniadis *et al.*, Science 340 (2013) 6131.
- [7] O. Hashimoto, H. Tamura, Prog. Part. Nucl. Phys. 57 (2006) 564.
- [8] O. Buss, *et al.*, Phys. Rept. 512 (2012) 1.
- [9] G.A. Lalazissis, *et al.*, Phys. Lett. B671 (2009) 36.
- [10] A. B. Larionov, T. Gaitanos and U. Mosel, Phys. Rev. C85 (2012) 024614.
- [11] B. Holzenkamp, K. Holinde, J. Speth, Nucl. Phys. A500 (1989) 485;  
A. Reuber, K. Holinde, J. Speth, Nucl. Phys. A570 (1994) 543.
- [12] Y. Fujiwara, *et al.*, Phys. Rev. 54 (1996) 2180;  
M. Kohno, *et al.*, Nucl. Phys. A674 (2000) 229;  
Y. Fujiwara, *et al.*, Prog. Part. Nucl. Phys. 58 (2007) 439.
- [13] K. Sasaki, *et al.*, Phys. Rev. C74 (2006) 064002;  
J. Haidenbauer, U.-G. Meissner, Phys. Rev. C72 (2005) 044005.
- [14] Landolt-Börnstein, New Series I/12b, [http : //dx.doi.org/10.1007/b35211](http://dx.doi.org/10.1007/b35211).
- [15] T.A. Rijken, Y. Yamamoto, nucl-th/0608074.
- [16] T. Gaitanos and H. Lenske, Phys. Lett. B737 (2014) 256.
- [17] E.S. Golubeva, *et al.*, Nucl. Phys. A537 (1992) 393.
- [18] M. F. M. Lutz, *et al.*, [PANDA Collaboration], arXiv:0903.3905 [hep-ex].
- [19] A. Esser, *et al.*, Nucl. Phys. A914 (2013) 519.
- [20] T. Gaitanos, Ch. Moustakidis, G.A. Lalazissis, H. Lenske, Nucl. Phys. A,  
in press.
- [21] S. Weissenborn, D. Chatterjee and J. Schaffner-Bielich, Nucl. Phys. A881  
(2012) 62.
- [22] Ch. Moustakidis, T. Gaitanos, G.A. Lalazissis, in preparation.

## Lifetime of the $4^+_1$ state of $^{148}\text{Ce}$ and its $B_{4/2}$ ratio

P. Koseoglou <sup>1\*</sup>, V. Werner <sup>1,2</sup>, N. Pietralla <sup>1</sup>, S. Ilieva <sup>1</sup>, C. Bernards <sup>2</sup>, A. Blanc <sup>3</sup>, A.M. Bruce <sup>4</sup>, R.B. Cakirli <sup>5</sup>, N. Cooper <sup>2</sup>, G. de France <sup>6</sup>, M. Jentschel <sup>3</sup>, J. Jolie <sup>7</sup>, U. Koester <sup>3</sup>,  
T. Kröll <sup>1</sup>, P. Mutti <sup>3</sup>, Z. Patel <sup>8</sup>, V. Pazyi <sup>9</sup>, Zs. Podolyak <sup>8</sup>, P. H. Regan <sup>8,10</sup>, J.-M. Régis <sup>7</sup>,  
O.J. Roberts <sup>4</sup>, N. Saed-Samii <sup>7</sup>, G.S. Simpson <sup>11</sup>, T. Soldner <sup>3</sup>, C. A. Ur <sup>12</sup>, W. Urban <sup>3</sup>, D. Wilmsen <sup>7</sup>,  
E. Wilson <sup>8</sup>

*1 IKP TU-Darmstadt, Germany / 2 Yale University, USA / 3 ILL Grenoble, France*  
*4 University of Brighton, England / 5 MPIK Heidelberg, Germany*  
*6 GANIL Caen, France / 7 IKP University of Cologne, Germany*  
*8 University of Surrey, England / 9 Universidad Complutense, Spain*  
*10 National Physical Laboratory, UK / 11 LPSC Grenoble, France / 12 INFN Legnaro, Italy*  
\*pkoseoglou@ikp.tu-darmstadt.de

### Abstract

Gamma radiation from  $^{235}\text{U}$  and  $^{241}\text{Pu}$  fission fragments were measured by a mixed spectrometer consisting of high-resolution Ge and fast  $\text{LaBr}_3(\text{Ce})$ -scintillator detectors at the high-flux reactor of the ILL. Prompt  $\gamma$ -ray cascades from the nuclei of interest are selected via Ge-Ge- $\text{LaBr}_3$ - $\text{LaBr}_3$  coincidences. The good energy resolution of the Ge detectors allows for setting precise gates, selecting the cascade, hence, the nucleus of interest. The excellent timing performance of the  $\text{LaBr}_3$  detectors in combination with the Generalized Centroid Difference method [8] allows the measurement of lifetimes in the ps range in preparation for the FATIMA experiment at FAIR. The first results on the neutron-rich nuclide  $^{148}\text{Ce}$  are presented.

### Introduction

The even-even  $N=90$  isotones with  $Z=60-66$ , present an interesting phase transition. This phase transition in nuclei is characterized by a sudden change of the shape of the nucleus due to changes in the location of the potential minimum [1]. The work of F. Iachello on geometrical models, based on the Bohr-Hamiltonian, describing spectroscopic properties at the critical point of the transition [3, 4] spurred much work on this classical region of spherical-to-prolate deformed transition nuclei, the light rare-earth nuclei around neutron number  $N=90$ . This phase transition is obvious in the  $R_{4/2}=E(4^+_1)/E(2^+_1)$  plot of these isotopes over the neutron number (Figure 1). The sharp transition in the Gd and Sm isotopic chains [1, 2, 5] from spherical nuclei ( $R_{4/2}=2-2.4$ ) to deformed ones ( $R_{4/2}=3-3.33$ ) is less pronounced in the Nd and Ce chains. The  $B_{4/2}=B(E2; 4^+_1 \rightarrow 2^+_1)/B(E2; 2^+_1 \rightarrow 0)$  ratio can give additional information on the shape of the nucleus ( $B_{4/2}=2$  for spherical symmetry,  $B_{4/2}=1.4$  for  $\gamma$ -rigid and  $\gamma$ -soft symmetries). Note, that  $7/10 \cdot B_{4/2}$  approximates the fourth order shape invariant  $K_4$  [6, 7] and is a measure of the softness of the potential in  $\beta$ . Figure 2 presents the  $B_{4/2}$  ratio for Gd, Sm and Nd isotopes as a function of the neutron number. The transition from  $N=88$  to  $N=90$  from near spherical symmetry to quadrupole deformed shapes is sharp for Gd and Sm but not as much for Nd.

The EXILL&FATIMA campaign provides data for extending these isotopes' region to more neutron-rich species in the vicinity of  $N=90$ . Cold-neutron induced fission of  $^{235}\text{U}$  and  $^{241}\text{Pu}$  at the Institut Laue-Langevin (ILL) of Grenoble, France, and the prompt  $\gamma$ -rays coming from the nuclei in interest were detected using an array of Ge and Ce-doped  $\text{LaBr}_3$  detectors (EXILL&FATIMA spectrometers [8]). In

this work the investigation over  $^{148}\text{Ce}$  is presented. The lifetime of the first  $4^+$  state and the  $B_{4/2}=\text{B}(E2; 4^+_1 \rightarrow 2^+_1)/\text{B}(E2; 2^+_1 \rightarrow 0)$  ratio are presented.

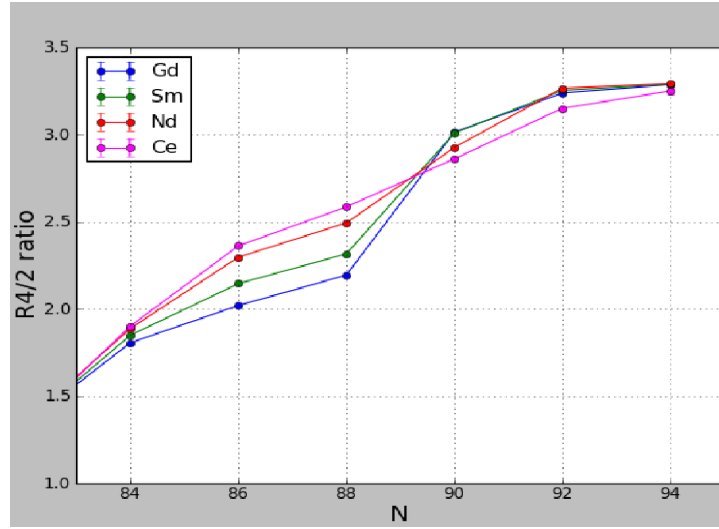


Figure 1

$R_{4/2}$  ratio over neutron number. The sharp transition of Gd and Sm from a spherical nuclei ( $R_{4/2}=2-2.4$ ) to a deformed one ( $R_{4/2}=3-3.33$ ) is not presented on Nd and Ce chains.

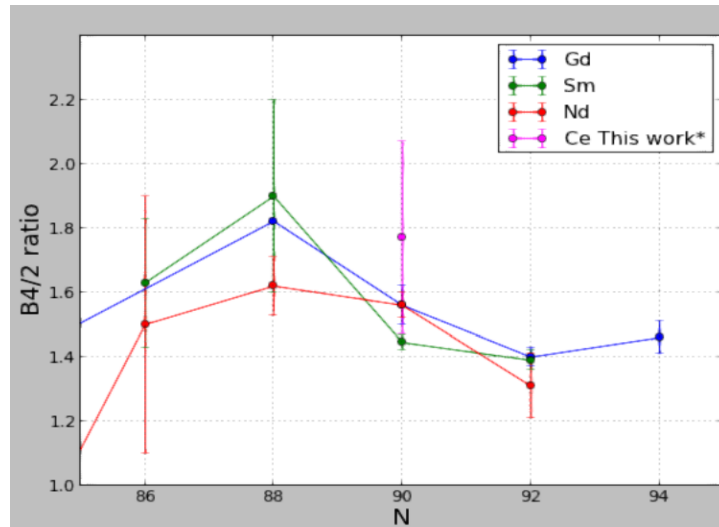


Figure 2

The  $B_{4/2}$  ratio can give additional information for the shape of the nucleus (2 for spherical symmetry, 1.4 for  $\gamma$ -rigid and  $\gamma$ -soft symmetries). Here the  $B_{4/2}$  ratio for Gd, Sm and Nd isotopes over the neutron number are presented, the transition from  $N=88$  to  $N=90$  from near spherical symmetry to  $\gamma$ -rigid and  $\gamma$ -soft symmetry is sharp for Gd and Sm but not for Nd. The obtained value for  $^{148}\text{Ce}$  is also presented.

## Experimental setup

More than 100 different nuclear species are strongly produced in fission. The HPGe high-resolution detectors of EXILL array (EXOGRAM in ILL) allowed the precise gate on the cascade of interest, hence, the nucleus of interest. The excellent time performance of the  $\text{LaBr}_3$  detectors in combination with the Generalized Centroid Difference method allowed the measurement of lifetimes in the ps range [1,2].

The EXILL array in ring shape was consisting out of 8 BGO-shielded EXOGAM clover detectors (composite detectors, each made of 4 Ge crystals) with target-to-detector distance of 14.5 cm, in 90° relative to beam direction. The FATIMA array was consisting by 2 rings of 8 (5% Ce-doped) LaBr<sub>3</sub> detectors each, with target to detector distance of 8.5 cm, in 40° and 140° relative to beam direction. Precise description of the setup can be found in [8]. All the fragments of the fissions were stopped by the thick packing of the target in <1ps. Ge-Ge-LaBr<sub>3</sub>-LaBr<sub>3</sub> quadruple coincidences were used to gate on the cascade of interest. The two Ge gates performed to “clean” the spectrum and the LaBr<sub>3</sub> gates were applied to the feeder and the decay gamma of the first 4<sup>+</sup> state of <sup>148</sup>Ce for the determination of the lifetime.

## Analysis – Conclusion

### Lifetime of the 4<sub>1</sub><sup>+</sup> state of <sup>148</sup>Ce

“Soco-v2” a C++ software package [10] was used to read and work with the data of the experiment. The Generalized Centroid Difference method [9] was used to extract the lifetime of the first 4<sup>+</sup> state of <sup>148</sup>Ce. This lifetime has not been measured in the past. For this case 4 gates were performed in total, two in Ge and two in LaBr<sub>3</sub> detectors. Three different cases of gating conditions on the Ge gates were performed and the data were summed (the event building procedure deter the usage of the same event more than one time). The gating cases can be seen in table 2. To make sure that the gates on the LaBr<sub>3</sub> detectors were clean of any contamination, gates were performed step by step and the Ge spectrum were checked in all gating cases. In figure 3 the Ge and LaBr<sub>3</sub> spectrum can be seen after applying the 2 Ge gates (left) and after performing also the LaBr<sub>3</sub> gate on the decay gamma of the first 4<sup>+</sup> state (right). Both LaBr<sub>3</sub> gates are not contaminated by any other significant big peak.

After applying the Ge gates and the first gate on the LaBr<sub>3</sub> (on the decay gamma of the 4<sub>1</sub><sup>+</sup> state) in each gating condition case, the LaBr<sub>3</sub>-time distribution matrix were summed (this was done for both start and stop matrix). A cut was applied on the summed LaBr<sub>3</sub>-time distribution matrix on the feeder gamma of the 4<sub>1</sub><sup>+</sup> state. The cut window was 24keV. The Peak-to-BG ratio on this 24 keV window was  $\Pi \approx 0.49$  (0.02) for both start and stop matrix. The two time distributions (start and stop) are presented on figure 4. The centroid difference is  $\Delta C = 51.5$  (6.4) ps. The centroid of each time distribution (“center of gravity” [11]) was obtained by integration.

The lifetime was obtained by using formula below [8], where  $\tau$  is the lifetime,  $\Delta C$  is the centroid difference, PRD the prompt respond difference for the setup for the combination of the feeder and the decay gamma which describes the linearly combined  $\gamma$ - $\gamma$  time-walk characteristics of FATIMA,  $\Pi$  the peak to background ratio,  $\Delta C_{Compton}$  the centroid difference of the Compton BG underneath the feeder peak,

$$\tau = \frac{1}{2} \left( \Delta C + \frac{\Delta C - \Delta C_{Compton}}{\Pi} - PRD \right)$$

The PRD for EXILL&FATIMA setup was determined using cascades with known lifetimes from <sup>152</sup>Eu decay (energy range: 40 – 1408 keV) and <sup>48</sup>Ti(n,g)<sup>49</sup>Ti reaction (energy range: 342 – 6760 keV). The PRD calibration with reference to 342 keV can be seen in figure 5. The PRD between the feeder and the decay gamma calculated to be PRD=PRD(386.15)-PRD(295.07)= -25 (2) ps. For the Compton background under the feeder peak an extrapolation of the Compton background around the peak was used (figure 6) and calculated to be  $\Delta C_{Compton} = 41$  (4) ps. The PRD calibration and the Compton investigation procedures are presented thoroughly in [1,2]. The preliminary lifetime for the first 4<sup>+</sup> state on <sup>148</sup>Ce obtained to be  $\tau_{4+} = 49$  (8) ps. In the present work only the Uranium date were analyzed.

Gating Case	Ge gate (gamma energy keV)	Ge gate (gamma energy keV)	LaBr gate (gamma energy keV)	LaBr gate (gamma energy keV)
1	Decay of $10^+_1$ (500.8)	Decay of $8^+_1$ (450.75)	Decay of $4^+_1$ (295.07)	Decay of $6^+_1$ (386.15)
2	Decay of $8^+_1$ (450.75)	Decay of $2^+_1$ (158.468)	Decay of $4^+_1$ (295.07)	Decay of $6^+_1$ (386.15)
3	Decay of $10^+_1$ (500.8)	Decay of $2^+_1$ (158.468)	Decay of $4^+_1$ (295.07)	Decay of $6^+_1$ (386.15)

Table 2

The three cases of gate conditions which were summed.

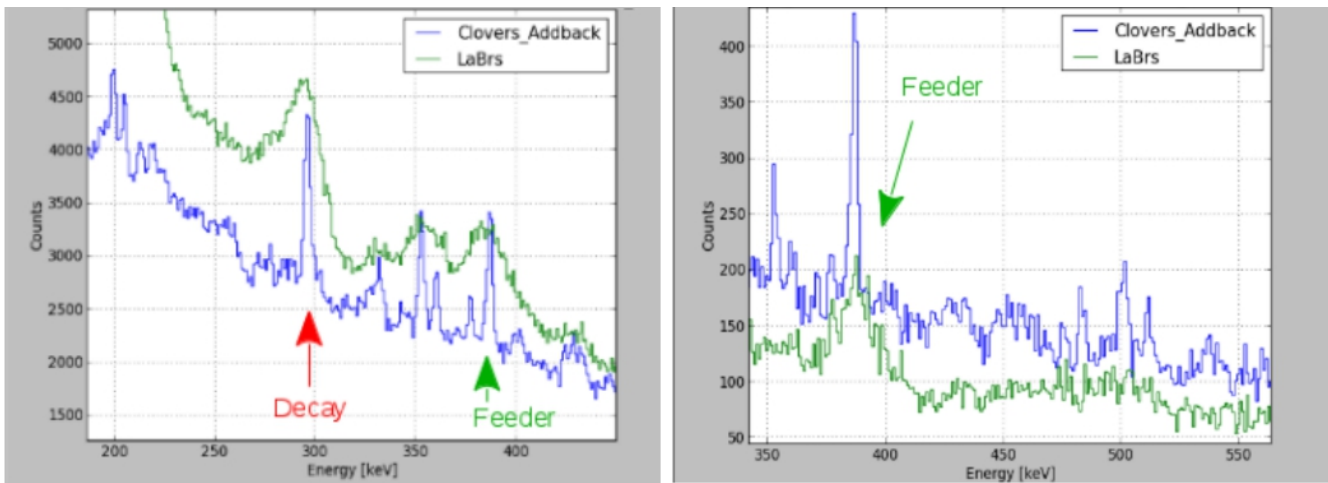


Figure 3

The Ge and LaBr<sub>3</sub> spectrum after gating on the decay transitions of the first 10<sup>+</sup> and first 8<sup>+</sup> states of <sup>148</sup>Ce on Ge (left) and after gating also on the decay transition of the first 4<sup>+</sup> state on the spectrum measured with the LaBr<sub>3</sub> detectors (right). The LaBr<sub>3</sub> gates on the decay and the feeder transitions of the first 4<sup>+</sup> state present no contamination of any other significant big peak.

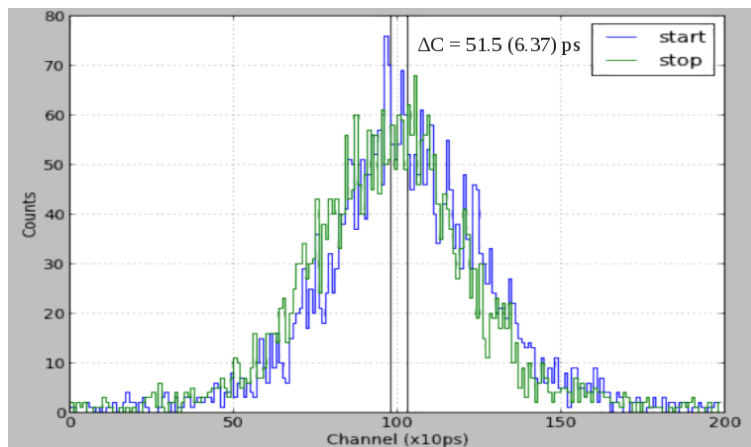


Figure 4

Time distribution spectrum. In “start” the feeder transition was the start signal, in “stop” the feeder transition was the stop signal. The centroid difference is  $\Delta C = 51.5 (6.37) \text{ ps}$ . The centroid of each time distribution was obtained by integration.

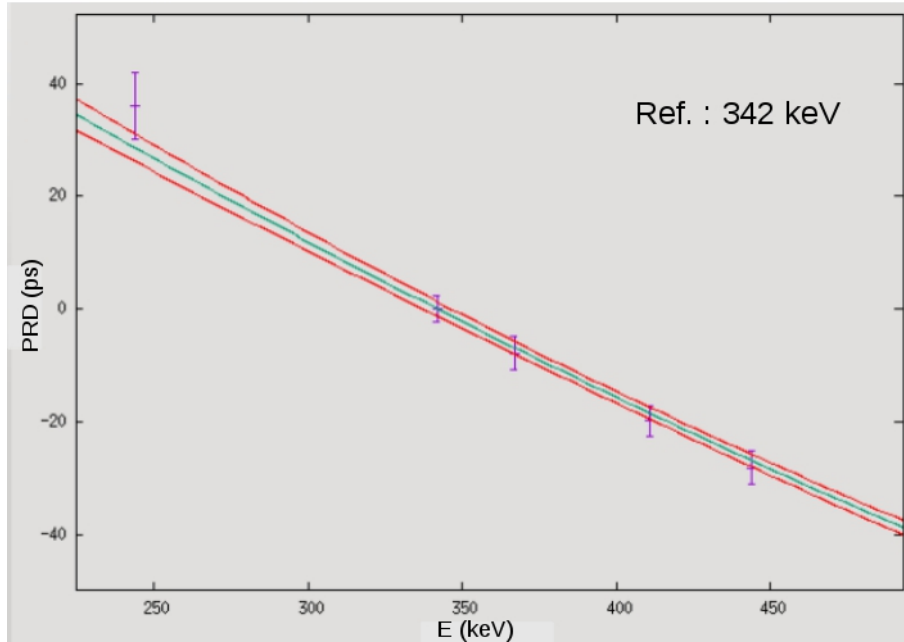


Figure 5

PRD calibration plot (purple points) and the fit of the PRD function (green line, the red lines are the errors on each point). Data are adjusted for the reference energy of 342 keV as explained in reference [8].

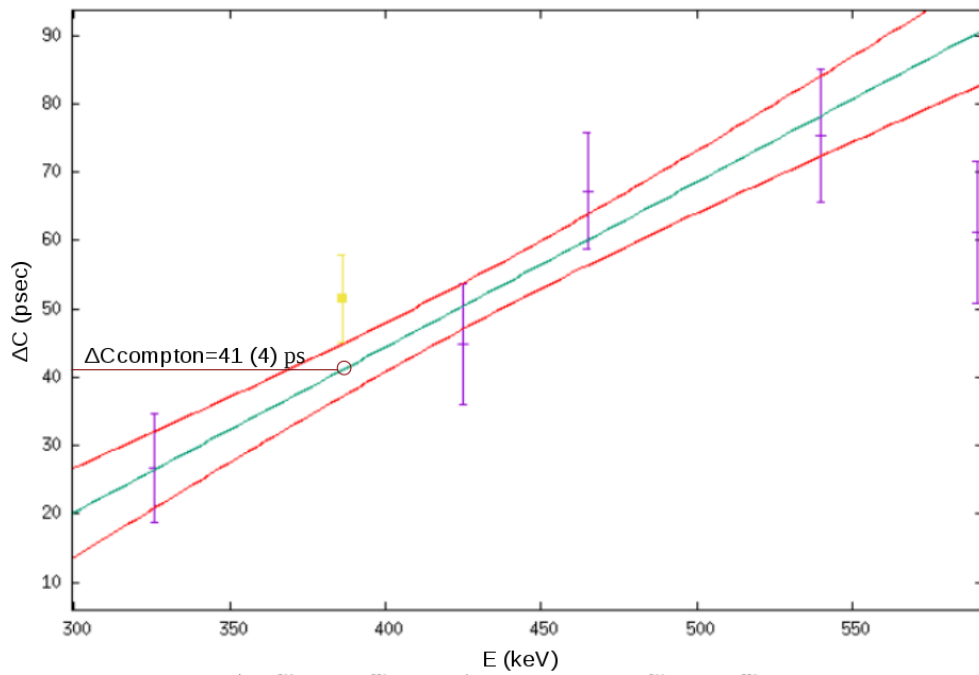


Figure 6

Compton investigation around the peak of the feeder transition (386.15 keV). The yellow point is the centroid difference ( $\Delta C$ ), for comparison.

## B<sub>4/2</sub> ratio

The lifetimes of the first 2<sup>+</sup> is known and the first 4<sup>+</sup> states on <sup>148</sup>Ce was measured, τ<sub>2+</sub>= 1457 (86) ps τ<sub>4+</sub>= 49.1 (8.3) ps. The B(E2)↓ values for each transition can be calculated by the decay width Γ and the lifetime. The general formula is the following.

$$\Gamma(\sigma \lambda; I_i \rightarrow I_f) = \frac{\hbar}{\tau} = \frac{8\pi(\lambda+1)}{\lambda[(2\lambda+1)!!]^2} \left(\frac{E_\gamma}{\hbar c}\right)^{(2\lambda+1)} B(\sigma \lambda; I_i \rightarrow I_f) (1+\alpha)^{-1}$$

The B↓(E2; 2<sub>+</sub><sup>1</sup>→0)= 3984 (237) e<sup>2</sup>fm<sup>4</sup> and B↓(E2; 4<sub>+</sub><sup>1</sup>→2<sub>+</sub><sup>1</sup>)= 7065 (1196) e<sup>2</sup>fm<sup>4</sup>. The B<sub>4/2</sub> ratio is 1.77 (0.32), mainly the error is occurring from the error in the τ<sub>4+</sub>. Beside of the big error, the ratio appears exactly between the values for deformed nucleus (ratio near to 1.4) and to nucleus with spherical symmetry (ratio near 2). Figure 7 present the B<sub>4/2</sub> ratios for N=90, for comparing the Ce with Nd, Sm, Gd and Dy, and figure 2 the B<sub>4/2</sub> ratio for Ce, Nd, Sm and Cd isotopes.

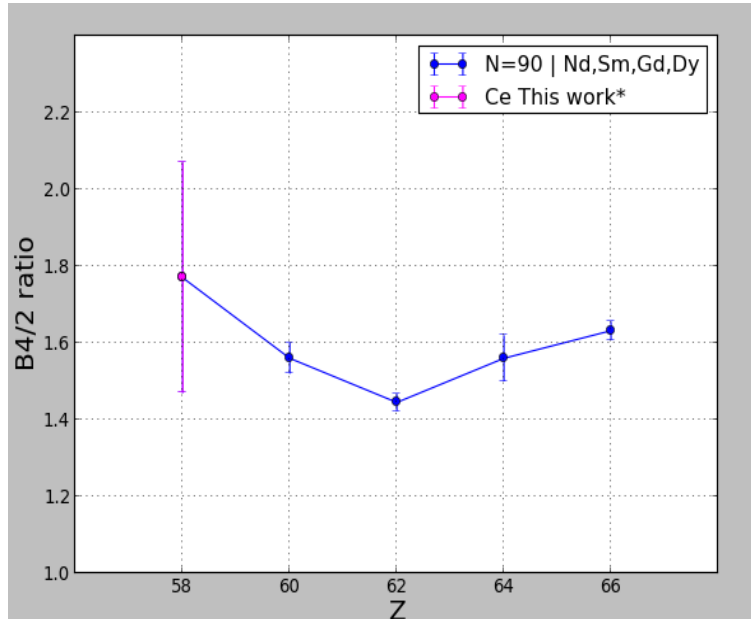


Figure 7

*B<sub>4/2</sub> ratios for N=90, for comparing Ce with Nd, Sm, Gd and Dy.*

**Acknowledgments.** This work was supported by the cooperation between TU Darmstadt and the GSI Helmholtz Center for Heavy Ion Research and by HGS-HIRE, by US DOE under Grant No. DE-FG02-91ER-40609, by STFC (UK) Grand No. ST/L005743/1 and ST/G000751/1.

## References

- [1] R. F. Casten and N. V. Zamfir, Phys. Rev. Lett. **87**, 052503 (2001)
- [2] R. F. Casten, Nuclear Structure from a Simple Perspective (Oxford University Press, Oxford, 1990)
- [3] F. Iachello, Phys. Rev. Lett. **85**, 3580 (2000)
- [4] F. Iachello, Phys. Rev. Lett. **87**, 052502 (2001)

- [5] N. Pietralla and O.M.Gorbachenko, Phys.Rev. C **70**, 011304 (2004)
- [6] R. V. Jolos, et al., Nucl. Phys. A**618**, 126 (1997)
- [7] V. Werner, et al., Phys. Lett. **521B**, 146 (2001)
- [8] J.-M. Régis, et al., Nucl. Instr. and Methods A **763** (2014) 210-220
- [9] J.-M. Régis, et al., Nucl. Instr. and Methods A **726** (2013) 191-202
- [10] N. Saed-Samii, Diploma Thesis, University of Cologne, 2013, unpublished
- [11] Z. Bay, Phys. Rev. **77**, 419 (1950)

# Systematic study of proton-induced spallation reactions with the Constrained Molecular Dynamics (CoMD) model

A. Assimakopoulou<sup>1</sup>, G. A. Souliotis<sup>1,\*</sup>, A. Bonasera<sup>2,3</sup>, M. Veselsky<sup>4</sup>

<sup>1</sup>Laboratory of Physical Chemistry, Department of Chemistry, National and Kapodistrian University of Athens, Athens, Greece

<sup>2</sup>Laboratori Nazionali del Sud, INFN, Catania, Italy,

<sup>3</sup>Cyclotron Institute, Texas A & M University, College Station, Texas, USA

<sup>4</sup>Institute of Physics, Slovak Academy of Sciences, Bratislava, Slovakia

\*Corresponding author, Email: soulioti@chem.uoa.gr

## Abstract

Proton – induced spallation reactions on <sup>238</sup>U, <sup>208</sup>Pb, <sup>181</sup>Ta and <sup>197</sup>Au targets at high energies were studied and investigated using the microscopic Constrained Molecular Dynamics (CoMD) model. Total fission cross sections, the ratio fission cross section to residue cross section, mean kinetic energy of fission fragments, mass yield curves and the number of nucleons emitted, before and after scission, as well as the total nucleon multiplicity were calculated using the CoMD model and compared with experimental data from the literature. Some of our calculations showed satisfactory agreement with available experimental data. The calculations of cross sections and the ratio fission cross section to residue cross section as a function of the proton energy gave us the opportunity to estimate observables for unmeasured nuclides.

**Keywords** constrained modelular dynamics, spallation, spallation neutrons, ATW, ADS

---

## INTRODUCTION

Spallation reactions induced by high-energy protons are of importance for fundamental research and technical applications in nuclear physics, as for instance, medical physics applications and nuclear-reactor technologies. The most important applications of these reactions are the spallation neutron sources, energy production techniques based on accelerator driven systems (ADS), transmutation of radioactive waste and radiation shield design for accelerators and cosmic devices. All these applications require the total fission cross section to be known with high accuracy in a wide proton energy range.

Since the accelerator driven system is considered as an option for the incineration of radioactive waste, many efforts have been made in providing experimental data on interactions in the energy range (100 – 1000 MeV) protons and neutrons with targets that are used in the ADS. Because of the variety of target nuclei and the wide range of energy of the beam particles, theoretical models and nuclear-reaction codes are needed.

Since the available experimental data on spallation reactions are rather poor and fragmentary, an experimental and theoretical work started at GSI Darmstadt [1]. In particular they measured the production of individual nuclides from charged-particle induced spallation

reactions, using the inverse kinematics technique with the high resolution magnetic spectrometer FRS. Also improved codes [2] have been developed. However, there are still uncertainties concerning measured total fission cross sections and other observables.

In the present work we used the CoMD model, which is described in the references [11-15]. With this model we were able to reproduce (p,f) cross sections, mass yield curves, fission to residue cross sections, and neutron multiplicities for the targets  $^{238}\text{U}$ ,  $^{208}\text{Pb}$ ,  $^{181}\text{Ta}$  at 200, 500, 1000 MeV and  $^{197}\text{Au}$  at 800 MeV. We chose these targets because they are important especially for accelerator-driven systems (ADS). For example tantalum alloys and lead-bismuth eutectic are optimum materials for the construction of spallation neutron sources. In our work, we compared our CoMD calculations with experimental data taken from refs. [3-10].

### COMD RESULTS AND COMPARISONS TO EXPERIMENTAL DATA

The present work was based on the use of the microscopic CoMD model in order to simulate the p-induced spallation reactions at intermediate and high energies on heavy targets ( $^{238}\text{U}$ ,  $^{208}\text{Pb}$ ,  $^{181}\text{Ta}$  and  $^{197}\text{Au}$ ). Below we present the mass yield curve of the reaction p(500 MeV) +  $^{208}\text{Pb}$ , the ratio fission cross section to residue cross section for the targets  $^{238}\text{U}$ ,  $^{208}\text{Pb}$ ,  $^{181}\text{Ta}$  and  $^{197}\text{Au}$  and finally the neutron multiplicity for the reaction p(500 MeV) +  $^{208}\text{Pb}$  at 200, 500 and 1000 MeV. We compare the CoMD calculations with available experimental data as it is shown on the corresponding figures.

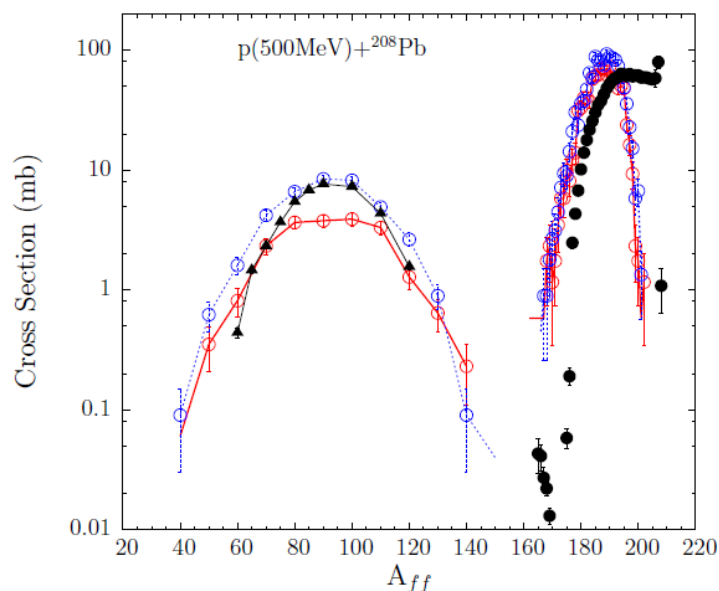


**Fig. 1.** Mass yield curve of fission fragments and heavy residues from the reaction p (500 MeV) +  $^{208}\text{Pb}$ , calculated with the CoMD code. Experimental data: black triangles [3], black circles [4], red points: CoMD calculations with the “standard” symmetry potential, blue points: CoMD calculations with the “soft” symmetry potential.

In Fig. 1, we show the mass number of the fragments as a function of the proton energy for the reaction  $p(500 \text{ MeV}) + {}^{208}\text{Pb}$ , calculated with the microscopic CoMD code. The CoMD calculations are compared with the experimental data of Rodriguez-Sanchez et al. [3] and Audouin et al. [4]. The red points represent the standard symmetry potential and the blue points the soft potential. Similarly, in this figure we distinguish two regions of fragments. One region has the fission fragments with the smaller mass numbers and the other region has the heavy residues with larger mass numbers, close to the target. We can observe that in the region with the fission fragments, the CoMD calculations are in overall agreement with the experimental data [3], which are indicated with black points. It seems that the cross sections for the fragments produced with the standard potential are lower than the cross sections produced with the soft symmetry potential. In the region with the heavy residues, the CoMD calculations are in agreement with data [4], although at heavier mass numbers there is a discrepancy with the data. We see also that the two symmetry potentials are in mutual agreement.

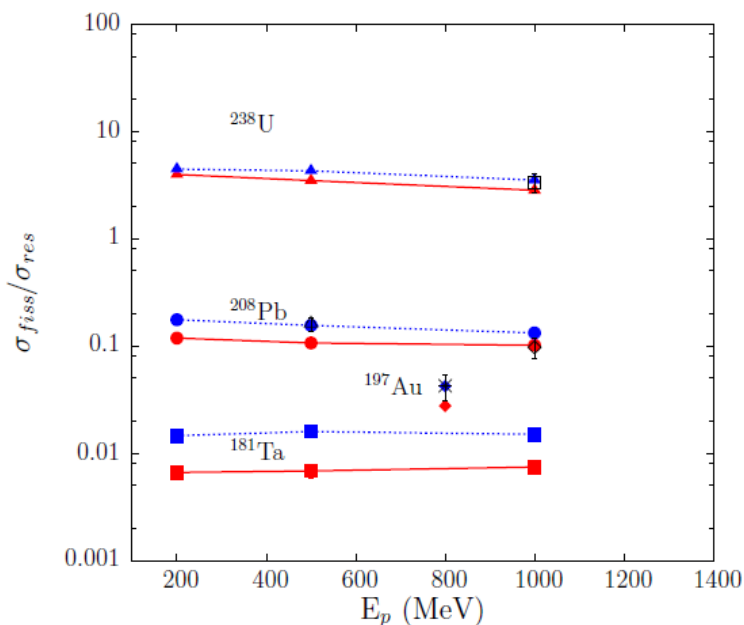


**Fig. 2.** Fission cross section to residue cross section ratio as a function of the proton energy at 200, 500 and 1000 MeV for the targets  ${}^{238}\text{U}$ ,  ${}^{208}\text{Pb}$  and  ${}^{181}\text{Ta}$  and  ${}^{197}\text{Au}$  at 800 MeV calculated with the CoMD code. The calculations are compared with experimental data. Red points: CoMD calculations with the “standard” symmetry potential, blue points: CoMD calculations with the “soft” symmetry potential. Experimental data: open square [6], open triangle [5], rhombus [7], star [8, 9].

In Fig. 2, we present the ratio of fission cross section to residue cross section as a function of the proton energy for  ${}^{238}\text{U}$ ,  ${}^{208}\text{Pb}$  and  ${}^{181}\text{Ta}$  at 200, 500 and 1000 MeV and  ${}^{197}\text{Au}$  at 800 MeV. We compare our calculations with the indicated experimental data. At first, we can observe that the ratio of  ${}^{238}\text{U}$  is about 8, which confirms that it is a high fissile nucleus. This value means that it has much higher possibility to undergo fission than evaporation. We notice also that the CoMD calculations at 1000 MeV are in good agreement with the data of Bernas et al. [19]. The ratio of fission cross section to residue cross section for  ${}^{208}\text{Pb}$ , calculated with the CoMD calculations, is about 10%. This demonstrates that lead target has a modest fissility. It appears that our calculations are in good agreement with the data of Fernandez et al. [5] at 500 MeV, especially the results with the soft symmetry potential. At 1000 MeV, the CoMD

calculations with the standard potential are in good agreement with the data of Enqvist et al. [7]. Next, we presented the ratio of  $^{197}\text{Au}$  at 800 MeV and this is about 6%. This shows that it has intermediate fissility in relation with tantalum and lead. We also compare our results with experimental data [8, 9]. The CoMD calculations with the soft symmetry potential are in very good agreement with the data. For  $^{181}\text{Ta}$ , the ratio is only about 1%, as calculated from the CoMD, showing its low fissility. This low value confirms that  $^{181}\text{Ta}$  is a low fissility target and shows its tendency to undergo mostly evaporation. In general, we can point out that the CoMD calculations with the soft potential are higher than the standard potential.

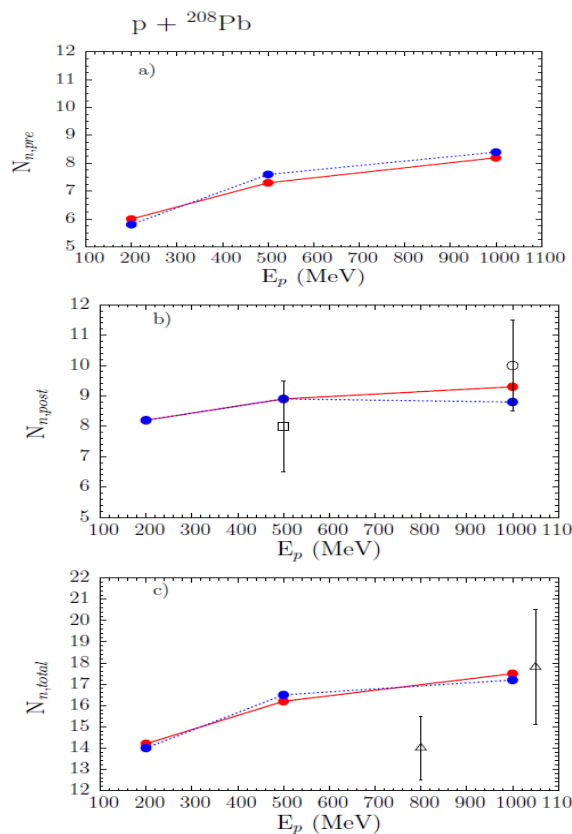


**Fig. 3.** a) neutron multiplicity before fission, b) neutron multiplicity after scission and c) total neutron multiplicity as a function of the proton energy for the reaction  $p + {}^{208}\text{Pb}$  at 200, 500 and 1000 MeV. The calculations are obtained with the CoMD code and are compared with experimental data. Red points: CoMD calculations with the “standard” symmetry potential, blue points: CoMD calculations with the “soft” symmetry potential. Experimental data: open square [5], open circle [7], open triangle [10] (displaced at 1100 from 1200).

In Fig. 3, we show the neutron multiplicity before scission, after scission and the total neutron multiplicity as a function of the proton energy for the reaction  $p + {}^{208}\text{Pb}$  at 200, 500 and 1000 MeV. The CoMD calculations are represented with red points for the standard symmetry potential and with blue points with the soft symmetry potential. In panel a), we can observe that as the proton energy increases, the number of neutrons that are emitted before scission increases. This happens because of the higher proton energy. In panel b), the number of neutrons that are emitted after scission increases as the proton energy increases, particularly in the calculations with the standard potential. We can point out that our CoMD calculations are higher than the data of Fernandez et al. [5] at 500 MeV, but within the error

bar. At 1000 MeV our results are within the error bar of the data of Enqvist et al [7]. In panel c) we present the total neutron multiplicity, which increases as the proton energy increases. Our calculations are compared with the experimental data of Leray et al. [10] at 800 and 1200 MeV. At 800 MeV we have not yet performed calculations with the CoMD code. At 1000 MeV our calculations are in agreement with the data of ref. [10] at 1200 MeV (which for display purposes, has been displaced at 1100 MeV).

## DISCUSSION AND CONCLUSIONS

From our calculations with the microscopic code CoMD, we see that the code is able to describe the full dynamic of the spallation process at high energies. We point out that we studied these targets because of the available experimental data in recent literature and because of their importance in the current applications of spallation. We observed that the fission of Pb (and also U, Ta, Au) target is symmetric due to the high excitation energy and because the shell effects at high energies are fully washed out. Also the ratio of fission over residue cross sections gave us the chance to make estimations for targets, such as  $^{181}\text{Ta}$ , where there are no experimental data and validate the existent data. Concerning the neutron multiplicities of  $p + ^{208}\text{Pb}$ , we found that they were also well reproduced, in comparison to experimental data. In general the CoMD calculations agree with the available experimental data for a broad range of observables that we have studied so far. We plan to present in detail the results of the present study in a full paper [16].

We conclude that further theoretical and experimental work of p-induced spallation reactions is needed, and we propose the systematic study of the above observables and comparison with experimental data. Besides the microscopic code CoMD, the use of phenomenological models INC and SMM and the comparison between them is considered important. We would like also to propose measurements in inverse kinematics concerning the  $^{181}\text{Ta}$  target.

## References

- [1] <https://www-win.gsi.de/charms>
- [2] A. Boudard, J. Cugnon, S. Leray, and C. Volant, Phys. Rev. C 66, 044615 (2002)
- [3] J.L. Rodriguez-Sanchez, J. Benlliure et al., Phys. Rev. C 91, 064616 (2015)
- [4] L. Audouin et al., NPA 768, 1-21 (2006)
- [5] B. Fernandez et al., Nucl. Phys. A 747, 227-267 (2005)
- [6] M. Bernas et al., Nucl. Phys. A 725 213-253 (2003)
- [7] T. Enqvist et al., Nucl. Phys. A 686, 481-524 (2001)
- [8] J. Benlliure, P. Armbruster et al., Nucl. Phys. A 700 469-491 (2002)
- [9] F. Rejmund et al., Nucl. Phys. A 683 540-565 (2001)
- [10] S. Leray et al., Phys. Rev. C 65, 044621 (2002)
- [11] M. Papa et al., J. Comp. Phys. 208, 403 (2005)
- [12] J. Aichelin, Phys. Rep. 202, 233 (1991)
- [13] M. Papa, Phys. Rev. C 87, 014001 (2013)
- [14] N. Vonta, G. A. Souliotis, M. Veselsky, A. Bonasera, Phys. Rev. C 92, 024616 (2015)
- [15] M. Papa, A. Bonasera, et al., Phys. Rev. C 64, 024612 (2001)
- [16] A. Assimakopoulou, G. A. Souliotis, A. Bonasera, M. Veselsky, in preparation

# Probing the cluster structure of ${}^7\text{Li}$ via elastic scattering on protons and deuterons in inverse kinematics

A. Pakou<sup>1,\*</sup>, V. Soukeras<sup>1</sup>, F. Cappuzzello<sup>2,3</sup>, L. Acosta<sup>4,5</sup>, C. Agodi<sup>2</sup>, X. Aslanoglou<sup>1</sup>, S. Calabrese<sup>2</sup>, D. Carbone<sup>2</sup>, M. Cavallaro<sup>2</sup>, A. Foti<sup>3,4</sup>, N. Keeley<sup>6</sup>, G. Marquinez-Duran<sup>7</sup>, I. Martel<sup>7</sup>, M. Mazzocco<sup>8,9</sup>, C. Parascandolo<sup>10</sup>, D. Pierroutsakou<sup>10</sup>, K. Rusek<sup>11</sup>, O. Sgouros<sup>1</sup>, E. Strano<sup>8</sup>, V. Zagatto<sup>2</sup>

<sup>1</sup> *Department of Physics and HINP, The University of Ioannina, Ioannina, Greece*

<sup>2</sup> *INFN, Laboratori Nazionali del Sud, Catania, Italy*

<sup>3</sup> *Dipartimento di Fisica e Astronomia, Inuversita di Catania, Catania, Italy*

<sup>4</sup> *INFN, Sezione di Catania, Catania, Italy*

<sup>5</sup> *Instituto de Fisica, Universidad Nacional Autonoma de Mexico, Mexico*

<sup>6</sup> *National Center for Nuclear Research, Otwock Warsaw, Poland*

<sup>7</sup> *Departamento de Fisica Aplicada, Universidad de Huelva, Huelva, Spain*

<sup>8</sup> *Departimento di Fisica e Astronomia, Universita di Padova, Padova, Italy*

<sup>9</sup> *INFN, Sezione di Padova, Padova, Italy*

<sup>10</sup> *INFN, Sezione di Napoli, Napoli, Italy*

<sup>11</sup> *Heavy Ion Laboratory, University of Warsaw, Warsaw, Poland*

---

## Abstract

Elastic scattering measurements have been performed for the  ${}^7\text{Li} + \text{p}$  system in inverse kinematics at the energies of 16, 25, 35 and 38.1 MeV and for the  ${}^7\text{Li} + \text{d}$  system at 38.1 MeV. The heavy ejectiles were detected by the large acceptance MAGNEX spectrometer at the Laboratori Nazionali del Sud (LNS) in Catania, Italy. The results are considered in a JLM and a CDCC framework. In the last case the cluster structure of  ${}^7\text{Li}$  proves to be critical for the theoretical interpretation of the experimental results.

---

## 1. Introduction

Continuing our systematic research of nucleon scattering on light weakly bound nuclei in inverse kinematics, we present in this article new elastic scattering results for  ${}^7\text{Li} + \text{p}$  and  ${}^7\text{Li} + \text{d}$  at near barrier energies ( $\sim 3$  to  $7x V_{C.b.}$ ).

---

\*e-mail:apakou@cc.uoi.gr

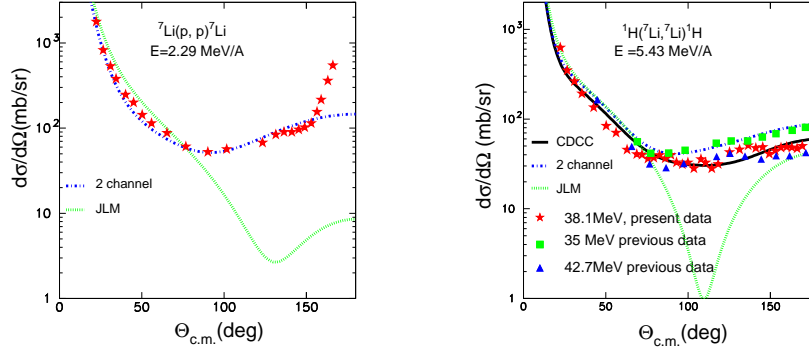


Figure 1: (Left panel) Elastic scattering of  ${}^7\text{Li} + p$  at 16 MeV (2.29 MeV/A). No CDCC calculation is performed for that energy as the available energy was not enough to excite the continuum.(right panel)Elastic scattering of  ${}^7\text{Li} + p$  at 38.1 MeV. The calculation includes excitations to continuum, and the resonance state. The variation between the CDCC and the 2 - channel approach is obvious here. The type of calculation compared with the data, is indicated in the Figure. Previous data are from [4].

It is well known that for energies above 10MeV/A and medium-heavy mass nuclei, the microscopic description of Jeukenne, Lejeune and Mahaux [1] potential (JLM potential) can be the basis for interpreting elastic scattering results. The applicability of JLM was succesfull in our recent studies for  ${}^{17}\text{F}+p$  [2], which was performed in inverse kinematics and at energies  $\sim 5$  MeV/A. The neutron skin of this nucleus was also successfully probed. Subsequently we have proceeded with elastic scattering studies of  ${}^6\text{Li}+p$  [3] putting in severe test the applicability of the model for this low mass projectiles and at the same low energies as in the  ${}^{17}\text{F}$  case. The JLM potential was found inadequate for describing such data. On the other hand Continuum Discretized Coupled Channel calculations (CDCC) were very succesfull, while the cluster structure of the projectile proved to be critical. Under the same motivation, we have extended our study on the elastic scattering of  ${}^7\text{Li}+p$  as well as on the elastic scattering of  ${}^7\text{Li}+d$ . Some inelastic scattering results were also considered.

## 2. Experimental details and Results

The experiment was performed at the MAGNEX facility of Istituto Nazionale di Fisica Nucleare Laboratori Nazionali del Sud (INFN - LNS) in Catania, Italy. Beams of  ${}^7\text{Li}^{3+}$  were accelerated by the TANDEM at the energies 16, 25, 35 and 38.1 MeV and impinged on a  $240 \mu\text{g}/\text{cm}^2$   $\text{CH}_2$  target. At the highest energy of 38.1 MeV the measurement was also performed with a  $260 \mu\text{g}/\text{cm}^2$   $\text{CD}_2$  target. Measurements were repeated with a  ${}^{12}\text{C}$  target of similar thickness, for estimating the carbon background. The elastically scattered lithium ions were momentum analyzed by the MAGNEX spectrometer [5, 6, 7], whose optical axis was set at  $\theta_{opt}=4^\circ$ , and were detected by its focal plane detectors [8]. For the elastic scattering on deuterons the optical axis of MAGNEX was set at  $\theta_{opt}=6^\circ$  and  $12^\circ$  for completing a full angular distribution measurement. Further details of the measurement and data analysis can be found in [3]. For an angular step of  $\sim 0.5^\circ$  and an angular uncertainty estimated to be  $\sim 2\%$ , angular distributions for all energies and both targets were formed. Sample results are shown for the lowest and highest energy at 16 and 38.1 MeV in Figure 1. In Figure 2 we present the results of elastic scattering on deuteron. Our results are compared with our calculations, to be briefly described below, and some previous results and were found to be in good consistency. It should be noted however, that only our data are extended to forward angles, where the scattering is Rutherford, therefore validating the normalization.

## 3. Theoretical calculations

For the microscopic JLM approach the Jeukenne, Lejeune and Mahaux model [1] is adopted according to the code developed by F. S. Dietrich at a standard normalization ( $\lambda_V=1.0$  and  $\lambda_W=0.8$ ). The density for  ${}^7\text{Li}$  was taken from Hartree Fock calculations performed by Trache et al. [9].

For the CDCC calculation we adopt the code FRESCO [10], in the form based in a cluster structure of the projectile or target. Some nuclei as  ${}^6,{}^7\text{Li}$  can be modeled as two inert clusters. Then, the Coulomb and nuclear excitations

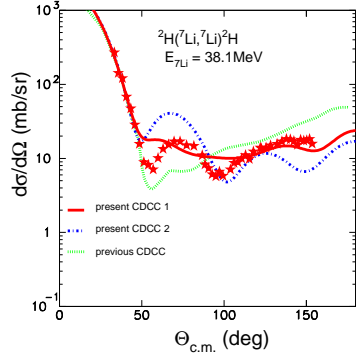


Figure 2: Present elastic scattering data of  ${}^7\text{Li} + \text{d}$  at 38.1 MeV, are compared with CDCC calculations. CDCC1 corresponds to present calculations taking into account excitations to continuum for  ${}^7\text{Li}$ , while CDCC2 corresponds to present calculations but taking into account excitations to continuum for  ${}^2\text{H}$ . Previous CDCC are from Tao Ye et al. [13] taking into account breakup of  ${}^2\text{H}$ .

can be interpreted and calculated in terms of the interactions of each cluster and the target. Therefore, a cluster  $\alpha + t$  model of  ${}^7\text{Li}$  is adopted. Special care was given for the potentials of each cluster and the target, that is, the  $p - \alpha$  and  $p - t$  potentials. For that empirical potentials were obtained by fitting previous elastic scattering data, studied at the appropriate energies  $E = \sim 2.5$  to 6 MeV/A [11] and were fed to a FRESKO calculation [10]. Couplings to the first excited state at 0.478 MeV and ground state reorientation was also considered. For the energy at 16 MeV no coupling to continuum was applied as the available energy is not enough for such excitation. The agreement of this simple calculation with the data (see Figure 1), where the only requirement is the cluster structure of the projectile should be underlined here. For the higher energies couplings to continuum were considered with all the parameters of the model including discretization and truncation described in detail in [12]. The  $7/2^-$  resonance at 4.630 MeV, was taken into account and was treated as momentum bin, with the width corresponding to 0.1 MeV. The calculation was repeated omitting couplings to continuum and/or to resonance state. No differentiation was observed at the energies of 25 and 35 MeV while at 38.1 MeV, as it can be seen in Figure 1, a substantial variation is seen, which is attributed solely to resonance excitation.

For the  ${}^7\text{Li} + \text{d}$  elastic scattering, calculations were done assuming couplings

to breakup either for  ${}^7\text{Li}$  or for  ${}^2\text{H}$ . Our results are presented in Figure 2, with the notation CDCC1, CDCC2 for the first and second scenario respectively. Both calculations can describe adequately well the data, but CDCC2 seems to be superior in respect with the better description of the scattering oscillatory nature.

#### 4. Summary

Elastic scattering studies for  ${}^7\text{Li} + \text{p}$  and  ${}^7\text{Li} + \text{d}$  were accomplished at energies 2 to 6 MeV/A. Measurements were performed at LNS-Catania with the MAGNEX spectrometer, and the results were interpreted in a microscopic JLM and a cluster + CDCC framework. It was found that the JLM potential does not apply to these low mass projectile and at these low energies. On the other hand, critical role to the second part of the calculation plays the cluster structure of  ${}^7\text{Li}$  ( ${}^4\text{He} + {}^3\text{H}$  mode) and for the higher energy couplings to the resonance state and not to continuum.

#### References

- [1] J.-P. Jeukenne, A. Lejeune and C. Mahaux, Phys. Rev. C 16, 80 (1977).
- [2] N. Patronis, A. Pakou, D. Pierroutsakou et al.; Phys. Rev. C 85, 024609 (2012).
- [3] V. Soukeras, A. Pakou, F. Cappuzzello et al.; Phys. Rev. C 91, 057601 (2015).
- [4] K. Kilian et al.; Nucl. Phys. A 126, 529(1969).
- [5] A. Cunsolo, F. Cappuzzello, M. Cavallaro et al.; Eur. Phys. J. Special Topics 150, 343 (2007).
- [6] A. Cunsolo, F. Cappuzzello, A. Foti et al.; Nucl. Instruments and Methods in Phys. Research A 484, 56 (2002).

- [7] A. Cunsolo, F. Cappuzzello, A. Foti et al.; Nucl. Instruments and Methods in Phys. Research A 481, 48 (2002).
- [8] M. Cavallaro, F. Cappuzzello, D. Carbone et al.; Eur. Phys. J. A 48, 59 (2012).
- [9] L. Trache et al., Phys. Rev. **C 61** (2000) 024612, and private communication
- [10] I.J. Thompson, Comput. Phys. Rep. 7, 167 (1988)
- [11] G. Freier et al.; Phys. Rev. 75, 1345(1949); P. D. Miller and G. C. Phillips; Phys. Rev. 112, 2043(1958); J. E. Brolley et al.; Phys. Rev. 117,1307(1960); R. Kankowsky et al.; Nucl. Phys. A263,29 (1976).
- [12] K. Rusek, P. V. Green, P.L. Kerr and K.W. Kemper, Phys. Rev. C **56**, 1895 (1997).
- [13] Tao Ye, Yukinobu Watanabe, Kazuyuki Ogata, Satoshi Chiba; Phys. Rev C 78, 024611(2008).

# Influence of resonance and continuum states on elastic scattering of ${}^6\text{Li}+\text{p}$

V. Soukeras<sup>1</sup>, A. Pakou<sup>1,\*</sup>, F. Cappuzzello<sup>2,3</sup>, L. Acosta<sup>4,5</sup>, C. Agodi<sup>2</sup>, N. Alamanos<sup>6</sup>, D. Carbone<sup>2</sup>, M. Cavallaro<sup>2</sup>, A. Di Pietro<sup>2</sup>, J.P. Fernandez-Garcia<sup>2</sup>, P. Figuera<sup>2</sup>, M. Fisichella<sup>2</sup>, A. Foti<sup>3,5</sup>, N. Keeley<sup>7</sup>, G. Marquinez-Duran<sup>8</sup>, I. Martel<sup>8</sup>, M. Mazzocco<sup>9</sup>, D. Pierrotsakou<sup>10</sup>, K. Rusek<sup>11</sup>, O. Sgouros<sup>1</sup>, E. Strano<sup>9</sup>, D. Torresi<sup>9</sup>

<sup>1</sup> *Department of Physics and HINP, The University of Ioannina, Ioannina, Greece*

<sup>2</sup> *INFN Laboratory Nazionali del Sud, Catania, Italy*

<sup>3</sup> *Dipartimento di Fisica e Astronomia, Universita di Catania, Catania, Italy*

<sup>4</sup> *Instituto de Fisica, Universidad Nacional Autonoma de Mexico, Mexico*

<sup>5</sup> *INFN Sezione di Catania, Catania, Italy*

<sup>6</sup> *CEA-Saclay, DAPNIA-SPhN, Gif-sur-Yvette, France*

<sup>7</sup> *National Center for Nuclear Research, Otwock Warsaw, Poland*

<sup>8</sup> *Departamento de Fisica Aplicada, Universidad de Huelva, Huelva, Spain*

<sup>9</sup> *Dipartimento di Fisica e Astronomia and INFN - Sezione di Padova, Padova, Italy*

<sup>10</sup> *INFN Sezione di Napoli, Napoli, Italy*

<sup>11</sup> *Heavy Ion Laboratory, University of Warsaw, Warsaw, Poland*

---

## Abstract

Elastic scattering measurements have been performed for the  ${}^6\text{Li} + \text{p}$  system in inverse kinematics at the energies of 16, 20, 25 and 29 MeV. The heavy ejectile was detected by the large acceptance MAGNEX spectrometer at the Laboratori Nazionali del Sud (LNS) in Catania, Italy. For the interpretation of the data, comprehensive Continuum Discretized Coupled Channel Calculations (CDCC) were performed for probing the influence of continuum and resonance states on elastic scattering. The results point out to a strong coupling to resonance states. Preliminary exclusive breakup angular distribution measurements will be also presented.

---

\*e-mail:apakou@cc.uoi.gr

## 1. Introduction

Collisions involving weakly bound nuclei, at low energies toward the Coulomb barrier, have disclosed interesting effects due to strong couplings to breakup [1]. The effect on elastic scattering of various weakly bound nuclei, stable and radioactive from low to heavy targets was thoroughly investigated in the past via Continuum Discretized Coupled Channel Calculations (CDCC) [1]. For  ${}^6\text{Li}$  projectiles, comprehensive analyses were done also from the point of view of the influence on elastic scattering of resonance state breakup or/and continuum breakup [2]. The study included low mass targets ( ${}^{16}\text{O}$  and  ${}^{24}\text{Mg}$ ) in a range of energies 4 to  $10xV_{C.b.}$ . It was found that both resonance and continuum breakup have equally strong influence on elastic scattering. For the lower energies however while the influence of continuum remains important the resonance state influence is the strongest one. On the other hand on recent studies at near barrier energies, below  $3.5xV_{C.b.}$  it was found that for low mass targets,  ${}^{28}\text{Si}$  and  ${}^{58}\text{Ni}$ , the coupling to resonance state has negligible effect [3] while on the contrary for heavier targets,  ${}^{144}\text{Sm}$ , the important coupling is the resonant one [4]. For  ${}^{6,7}\text{Li}$  on  ${}^{63}\text{Zn}$  [5] the significance of couplings to resonance is underlined.

In this work, we will present new elastic scattering measurements of  ${}^6\text{Li} + p$ , the simplest system, where the above issues can be clarified. Our elastic scattering data and CDCC calculations were reported already in Ref [6], while here we will present evidence for the influence of resonant and continuum states on elastic scattering as well as we will give preliminary results of our breakup measurement.

## 2. Experimental and Theoretical Details-Results

The experiment was performed at the MAGNEX facility of Istituto Nazionale di Fisica Nucleare Laboratori Nazionali del Sud (INFN - LNS) in Catania, Italy. Details of the measurement can be found in Ref. [6] and briefly we will give some points here. Beams of  ${}^6\text{Li}^{3+}$  were accelerated by the TANDEM at the energies

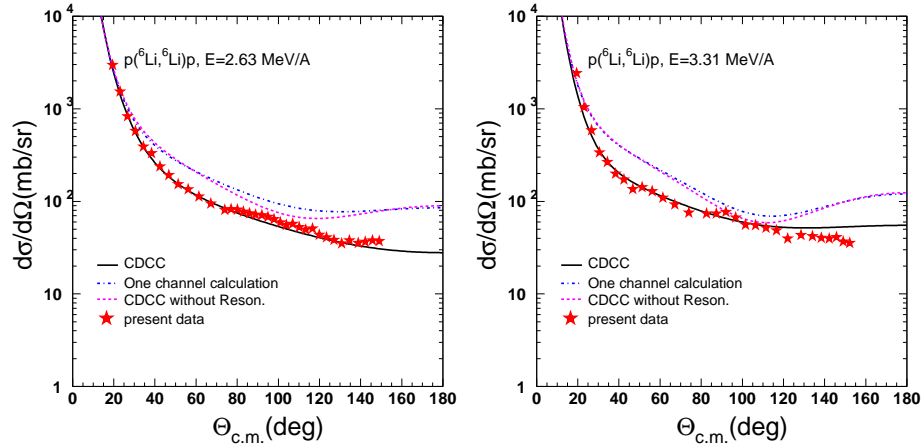


Figure 1: (Left panel) Elastic scattering of  ${}^6\text{Li}+p$  at 16 MeV (2.6 MeV/A). The type of calculation is designated in the plot (right panel) The same as before but for bombarding energy of 20 MeV (3.3 MeV/A).

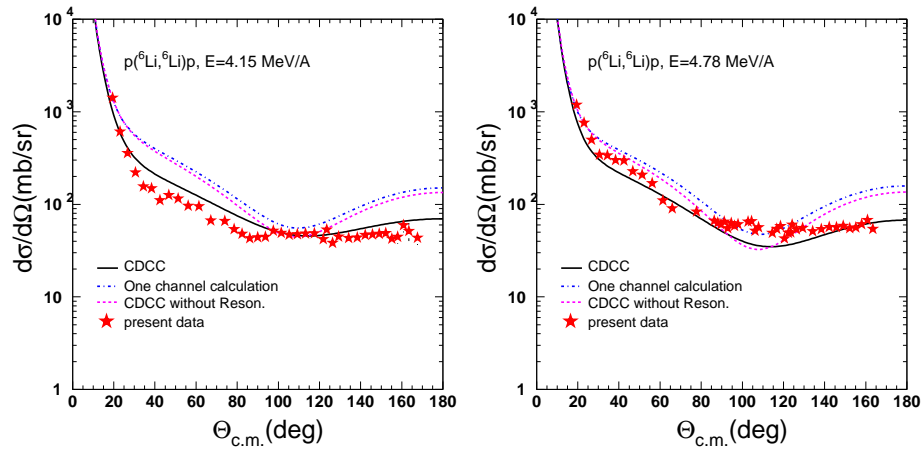


Figure 2: The same as in figure 1 but (left panel) for bombarding energy of 25 MeV (4.2 MeV/A) and (right panel) for bombarding energy of 29 MeV (4.8 MeV/A).

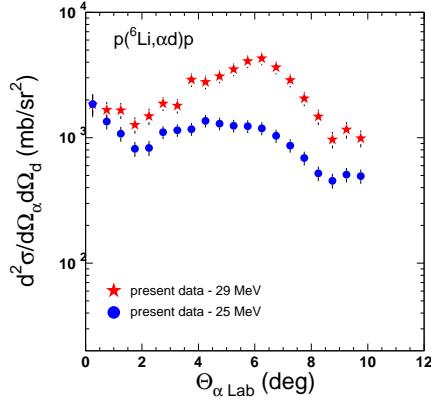


Figure 3: Angular distributions of exclusive breakup for 25 and 29 MeV

16, 20, 25 and 29 MeV and impinged on a  $240 \mu\text{g}/\text{cm}^2$   $\text{CH}_2$  target. Measurements were repeated with a  $^{12}\text{C}$  target of similar thickness, for estimating the carbon background. The elastically scattered lithium ions were momentum analyzed by the MAGNEX spectrometer [7], whose optical axis was set at  $\theta_{opt}=4^0$ , and were detected by its focal plane detectors. The exclusive breakup measurements were performed at the two highest energies, namely 25 and 29 MeV, requiring a coincidence between alpha fragments detected in MAGNEX and deuterons recorded in a silicon detector set at  $5^0$ . The detector was masked with a tantalum foil of appropriate thickness such as to stop the elastically scattered lithium ions but to allow deuterons to go through. MAGNEX worked in a full horizontal and vertical angular acceptance for breakup measurements, but with a reduced vertical acceptance in elastic scattering for protecting the focal plane detectors from the elastic high counting rate. After a successful trajectory reconstruction the experimental results were transformed to cross sections taking into account the target thickness, the flux of the beam recorded in a faraday cup, but also validated via Rutherford scattering at the most forward angles, and the solid angle. The solid angle, defined by 4 slits located at 250 mm from the target, was calculated taking into account the contour of the reconstructed  $(\theta_i, \phi_i)$  locus [8]. Our results are shown in Figures 1 and 2.

For the CDCC calculation, a cluster  $\alpha + d$  model of  ${}^6\text{Li}$  is adopted, with all the parameters of the model including discretization and truncation described in detail in [9]. The  $3^+$  resonance was taken into account and was treated as momentum bin, with the width corresponding to 0.1 MeV. The central part of the entrance potentials for  $\alpha - p$  and  $d - p$ , has been derived from empirical  $p - \alpha$  and  $p - d$  potentials by means of a single - folding method. The empirical potentials were obtained from previous elastic scattering data at the appropriate energies and were fed to a FRESCO calculation [11]. Our results, displayed in Figures 1 and 2, seem to reproduce the experimental data in a very adequate way. Subsequently in order to disentangle the influence of resonant and continuum couplings to elastic scattering, the calculation was repeated without any coupling (one channel calculation) where only the cluster structure of the projectile was probed and finally the calculation was repeated omitting the bin with the resonance. The results are compared with the data in Figures 1 and 2. It is obvious that the one channel calculation and the CDCC calculation, where the resonance was not taken into account, are almost identical and far from reproducing the data. This points out the fact that coupling to continuum is not significant for this energy regime (3 to 6  $xV_{C.b.}$ ), although for the higher energies, continuum starts to play some role. On the other hand coupling to resonance is very strong and the full CDCC calculation can describe very well the data. This is in accord with the findings in [2, 4, 5] but not [3] and clarifies that the target mass does not play any role for the influence of continuum or/and resonance state on elastic scattering. On the other hand the energy plays a critical role.

### 3. Summary

Elastic scattering measurements were performed in a very systematic way for  ${}^6\text{Li}+p$  at above barrier energies, namely 2.7 to 4.8 MeV/A. The results were treated in a CDCC framework and found to describe very well the data. It was shown that coupling to resonance state is the most important at these low

energies and not to the rest of continuum. The last starts to be significant as the projectile energy is increasing.

## References

- [1] N. Keeley, N. Alamanos, K. W. Kemper, K. Rusek; Prog. in Part. Nucl. Phys. **63**, 396 (2019); N. Keeley et al.; Prog. in Part. Nucl. Phys. **59**, 579 (2007); N. Keeley et al.; Eur. Phys. J **A 50**, 145 (2014).
- [2] Y. Hirabayashi; Phys. Rev. C **44**, 1581 (1991) and references therein.
- [3] A. Gomez Camacho et al.; Phys. Rev. C **91**, 014607 (2015).
- [4] A. Gomez Camacho et al.; Phys. Rev. C **93**, 024604 (2016).
- [5] J. P. Fernandez-Garcia et al.; Phys. Rev. C **92**, 054602(2015).
- [6] V. Soukeras, A. Pakou, F. Cappuzzello et al.; Phys. Rev. C **91**, 057601 (2015).
- [7] A. Cunsolo, F. Cappuzzello et al.; Eur. Phys. J. Special Topics **150**, 343 (2007); M. Cavallaro, F. Cappuzzello, D. Carbone et al.; Eur. Phys. J. A **48**, 59 (2012); A. Cunsolo, F. Cappuzzello et al.; NIM **A484**, 56 (2002); A. Cunsolo, F. Cappuzzello et al.; NIM **A481**, 48 (2002).
- [8] M. Cavallaro, F. Cappuzzello et al. NIM **A637**, 77 (2011).
- [9] K. Rusek, K. W. Kemper and R. Wolski, Phys. Rev. C **64**, 044602 (2001); K. Rusek, P. V. Green, P. L. Kerr and K. W. Kemper, Phys. Rev. C **56**, 1895 (1997).
- [10] R. Sherr, et al.; Phys. Rev. **72**, 662 (1947); F. Lahlou et al.; J. Phys. France **41**, 485(1980); D. C. Kocher, T. B. Clegg; Nucl. Phys. A **132**, 455(1969); A. S. Wilson et al.; Nucl. Phys. **A130**, 624(1969); K. Sagara et al.; Phys. Rev. C **50**, 576 (1994); G. Freier et al.; Phys. Rev. **75**, 1345(1949); P. D. Miller and G. C. Phillips; Phys. Rev. **112**, 2043(1958).
- [11] I. J. Thompson, Comput. Phys. Rep. **7**, 167 (1988).

# Study of the ${}^6\text{Li}+p \rightarrow {}^3\text{He}+{}^4\text{He}$ reaction in inverse kinematics

Ch. Betsou<sup>1</sup>, A. Pakou<sup>1,\*</sup>, F. Cappuzzello<sup>2,3</sup>, L. Acosta<sup>4,5</sup>, C. Agodi<sup>2</sup>, X. Aslanoglou<sup>1</sup>, D. Carbone<sup>2</sup>, M. Cavallaro<sup>2</sup>, A. Di Pietro<sup>2</sup>, J. P. Fernández-García<sup>2</sup>, P. Figuera<sup>2</sup>, M. Fisichella<sup>2</sup>, A. Foti<sup>3,4</sup>, N. Keeley<sup>6</sup>, G. Marquinez-Duran<sup>7</sup>, I. Martel<sup>7</sup>, M. Mazzocco<sup>8,9</sup>, N. G. Nicolis<sup>1</sup>, D. Pierroutsakou<sup>10</sup>, K. Rusek<sup>11</sup>, O. Sgouros<sup>1</sup>, V. Soukeras<sup>1</sup>, E. Stiliaris<sup>12</sup>, E. Strano<sup>9</sup>, D. Torresi<sup>2</sup>

<sup>1</sup> *Department of Physics and HINP, The University of Ioannina, Ioannina, Greece*

<sup>2</sup> *INFN, Laboratori Nazionali del Sud, Catania, Italy*

<sup>3</sup> *Dipartimento di Fisica e Astronomia, Inuversita di Catania, Catania, Italy*

<sup>4</sup> *INFN, Sezione di Catania, Catania, Italy*

<sup>5</sup> *Instituto de Fisica, Universidad Nacional Autonoma de Mexico, Mexico*

<sup>6</sup> *National Center for Nuclear Research, Otwock Warsaw, Poland*

<sup>7</sup> *Departamento de Fisica Aplicada, Universidad de Huelva, Huelva, Spain*

<sup>8</sup> *Departimento di Fisica e Astronomia, Universita di Padova, Padova, Italy*

<sup>9</sup> *INFN, Sezione di Padova, Padova, Italy*

<sup>10</sup> *INFN, Sezione di Napoli, Napoli, Italy*

<sup>11</sup> *Heavy Ion Laboratory, University of Warsaw, Warsaw, Poland*

<sup>12</sup> *Institute of Accelerating Systems and Applications and Department of Physics, University of Athens, Greece*

---

## Abstract

The  ${}^6\text{Li}+p \rightarrow {}^3\text{He} + {}^4\text{He}$  reaction was studied in inverse kinematics at incident energies of 2.7, 3.3, 4.2 and 4.8 MeV/u. Angular distribution measurements were performed detecting both recoils ( ${}^3\text{He}$  and  ${}^4\text{He}$ ) at  $\theta_{\text{lab}} = 16^\circ$  to  $34^\circ$  which allowed the determination of the angular distribution over a wide angular range in the center of mass frame ( $\theta_{\text{c.m.}} \sim 40^\circ$  to  $140^\circ$ ). The results clarify inconsistencies between existing data sets and are consistent with compound nucleus model calculations.

---

\*e-mail:apakou@cc.uoi.gr

## 1. Introduction

While the significance of the  ${}^6\text{Li}(p, {}^3\text{He}){}^4\text{He}$  reaction has been demonstrated for a long time in several experimental studies relevant to astrophysical problems and to studies of controlled thermonuclear reactors, it is considered in this work as a complementary study to our recent measurements of elastic scattering and breakup modes [1] with the MAGNEX spectrometer [2, 3, 4]. The latter is part of a systematic continuing research program of our group, relative to the optical potential at near-barrier energies with weakly-bound projectiles. In this respect the present results will be used in future work on a global understanding of the optical potential and relevant reaction mechanisms.

## 2. Experimental details and Results

The experiment was performed at the Istituto Nazionale di Fisica Nucleare, Laboratori Nazionali del Sud (INFN-LNS) in Catania, Italy. Beams of  ${}^6\text{Li}^{3+}$  were accelerated by the SMP13 tandem to energies of 16, 20, 25 and 29 MeV and impinged on a  $\sim 300 \mu\text{g}/\text{cm}^2$   $\text{CH}_2$  target. In a parallel basis to elastic scattering and breakup measurements performed with MAGNEX, angular distribution of the  ${}^6\text{Li} + p \rightarrow {}^4\text{He} + {}^3\text{He}$  reaction, reported herein, was performed using one telescope of the DINEX array [5] with  $\Delta E$  stage a DSSSD silicon detector, 48  $\mu\text{m}$  thick, and as an E stage, a silicon pad 530  $\mu\text{m}$  thick. The solid angle of each strip of the telescope was determined by an elastic scattering measurement performed with a gold foil target at the lowest energies, where the scattering can be considered as pure Rutherford. The gold foil measurements, together with measurements performed with a carbon foil 240  $\mu\text{g}/\text{cm}^2$  thick, were used for energy calibration purposes. The carbon target measurements were also used to estimate the background due to carbon in our  $\text{CH}_2$  target.

It should be noted that the angular distribution measurement was performed at each energy by detecting both reaction products,  ${}^4\text{He}$  and  ${}^3\text{He}$ . It was thus possible to span a wide angular range in the center of mass frame ( $\theta_{\text{c.m.}} = 40^\circ$  to  $140^\circ$ , corresponding to  $\theta_{\text{lab}} = 16^\circ$  to  $34^\circ$ ). The  ${}^3\text{He}$  ejectiles were well resolved

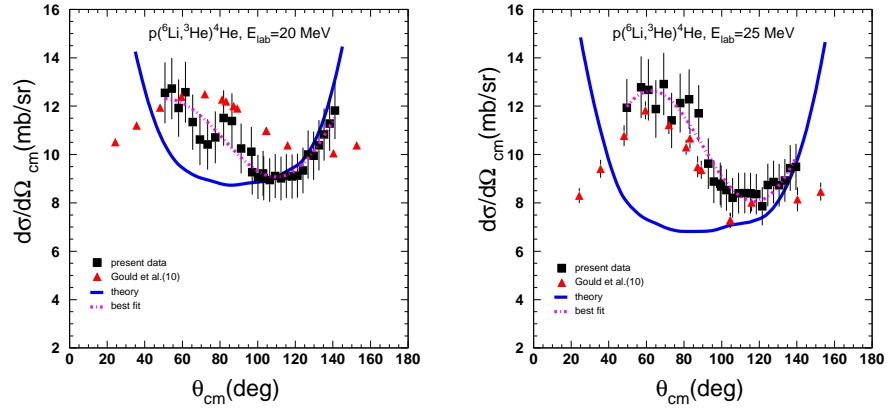


Figure 1: (Left panel) Present angular distribution data for the  $^6\text{Li}+p \rightarrow ^3\text{He}+^4\text{He}$  reaction at a bombarding energy of 16 MeV (2.7 MeV/u) are compared with previous data [7, 8] and with compound calculations performed with the code MECO [9]. (right panel) The same as before but for a bombarding energy of 20 MeV (3.3 MeV/u). The previous data are from Ref. [10].

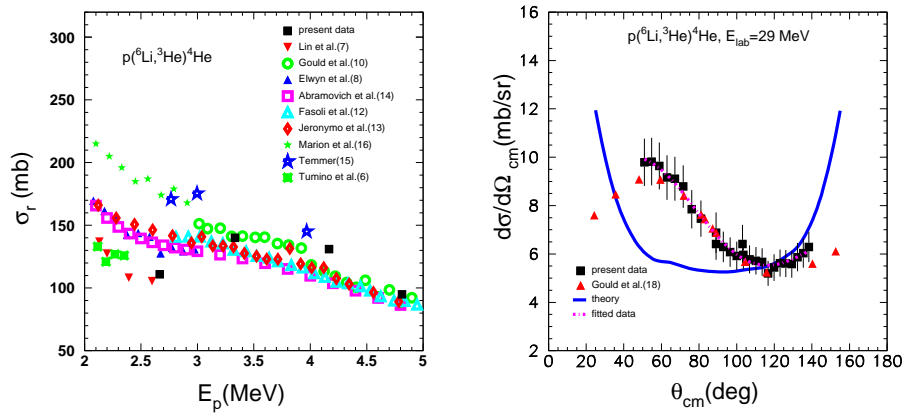


Figure 2: The same as in figure 1 but (Left panel) for bombarding energy at 25 MeV (4.2 MeV/u) and (right panel) for bombarding energy of 29 MeV (4.8 MeV/u).

via the  $\Delta E$ - $E$  technique. For the differential cross sections, integrated yields of  $^4\text{He}$  and  $^3\text{He}$  particles were normalized to the target thickness, the solid angle and flux, the last recorded in a Faraday cup and simultaneously tested by Rutherford scattering of  $^6\text{Li}$  detected in MAGNEX [1]. The assigned error in the differential cross sections due to statistics is less than 0.3 % and the rest is due to a 5 % error in the estimation of the target thickness, 5 % in the measured integrated beam charge and 7 % due to the solid angle measurement. The results at the four energies are presented in Figures 1 and 2 and are compared with previous measurements. At the two higher energies the agreement with the Gould et al. data [10] is good, at 20 MeV the agreement worsens, while at 16 MeV the inconsistency between the two existing sets of data of Elwyn et al. [8] and Lin et al. [7] is partly clarified by the present results. The new data at backward angles seem to agree well with the Lin et al. data, while at forward angles they seem to be located between the previous two measurements.

Statistical model calculations were performed [9] based to absorption cross sections obtained in a Continuum Discretized Coupled Channel (CDCC) context of our elastic scattering analysis as described in Ref. [1]. The results are presented in Figures 1 and 2 and exhibit an excellent agreement with the data at backward angles. This point out to an interconsistency of all data recorded and analyzed in the  $^6\text{Li}+p$  study. Also precludes the validity of the Elwyn et al. data [8] both in shape and intensity. However, comparing the theoretical predictions and the experimental data it is apparent that there is a broad peak centered at approximately  $\theta_{\text{c.m.}} = 50^\circ$  that is not explained by the MECO compound calculations and which becomes more pronounced as the bombarding energy increases. This peak could be due to a direct reaction component and this point was further considered in Ref. [11]. Finally, our differential cross sections were fitted to a sum of Legendre polynomials and the resulting reaction cross sections for the  $^6\text{Li}+p \rightarrow ^3\text{He}+^4\text{He}$  reaction are presented in Figure 3 in comparison with previous results [6, 7, 8, 10, 14, 12, 13, 15, 16] . The new results reveal previous inconsistencies and combined with the Lin et al. and Tumino et al. data [6, 7] could indicate the possible presence of a broad resonance at  $E_p = 3.7$  MeV.

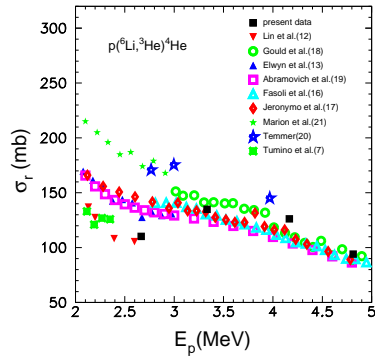


Figure 3: Present reaction cross section measurements as a function of energy, designated by the boxes, compared with previous values [6, 7, 8, 12, 13, 10, 14, 15, 16]. It should be noted that the data of Refs. [13, 14] are evaluated data and not original experimental data.

### 3. Summary

We have studied the reaction  ${}^6\text{Li}+p\rightarrow{}^3\text{He}+{}^4\text{He}$  in a complementary context of our elastic scattering and breakup studies. Indeed, the excellent agreement between angular distributions data at backward angles and statistical model calculations, based on absorption cross sections obtained from our elastic scattering studies supports a global description of the  ${}^6\text{Li}+p$  reaction. Further on previous inconsistencies are clarified with the very important issue of the support for the Lin et al and Tumino et al. data and the observation of a possible new broad resonance centered at  $E_p \sim 3.7$  MeV. Last but not least it was found that this reaction exhausts almost all the absorption from the elastic channel, while it proceeds at least by 85 % via a compound mechanism

### References

- [1] V. Soukeras, A. Pakou, F. Cappuzzello et al.; Phys. Rev. C **91**, 057601 (2015).
- [2] A. Cunsolo, F. Cappuzzello, M. Cavallaro et al.; Eur. Phys. J. Special Topics **150**, 343 (2007).
- [3] A. Cunsolo, F. Cappuzzello, A. Foti et al.; Nucl. Instruments and Methods in Phys. Research A **484**, 56 (2002).

- [4] A. Cunsolo, F. Cappuzzello, A. Foti et al.; Nucl. Instruments and Methods in Phys. Research A **481**, 48 (2002).
- [5] G. Marquinez-Duran et al.; Nucl. Instruments and Methods in Phys. Research A **A 755**, 69 (2014)
- [6] A. Tumino, C. Spitaleri et al.; Nucl. Phys. **A 734**, 639 (2004).
- [7] Lin Chia-Shou, Hou Wan-Shou, Wen Min, Chou Jen-Chang; Nucl. Phys. **A 275**, 93 (1977).
- [8] A. J. Elwyn et al.; Phys. Rev. **C 20**, 1984 (1979).
- [9] N.G. Nicolis, Int. Jour. Mod. Phys. **E17**, 1541 (2008).
- [10] C. R. Gould et al.; Nuclear Science and Engineering **55**, 267 (1974).
- [11] Ch. Betsou, A. Pakou, F. Cappuzzello et al., Eur. Phys. J A **51**, 86 (2015).
- [12] U. Fasoli, D. Toniolo and G. Zago, Phys. Lett. **B 8**, 127 (1964).
- [13] J. M. F. Jeronymo, G. S. Mani, A. Sadeghi, Nucl. Phys. **A 43**, 424 (1963).
- [14] S. N. Abramovich et al. ; Vop. At.Nauki i Tekhn., Ser.Yadernye Konstanty, 1984 Issue.4/58, 17 (1984)
- [15] G. M. Temmer; Nuclear Reaction Mechanisms Conference., Padua 1962, Italy, page 1013 (1962)
- [16] J. B. Marion, G. Weber, F. S. Mozer; Phys. Rev., **104**, 1402 (1956).

# Alpha - particle production in the reaction ${}^7\text{Be}+{}^{28}\text{Si}$ at near barrier energies

O. Sgouros<sup>1</sup>, A. Pakou<sup>1,\*</sup>, D. Pierroutsakou<sup>2</sup>, M. Mazzocco<sup>3,4</sup>, L. Acosta<sup>5,6</sup>,  
X. Aslanoglou<sup>1</sup>, Ch. Betsou<sup>1</sup>, A. Boiano<sup>2</sup>, C. Boiano<sup>7</sup>, D. Carbone<sup>8</sup>,  
M. Cavallaro<sup>8</sup>, J. Grebosz<sup>9</sup>, N. Keeley<sup>10</sup>, M. La Commara<sup>2,11</sup>, C. Manea<sup>4</sup>,  
G. Marquez-Duran<sup>12</sup>, I. Martel<sup>12</sup>, N.G. Nicolis<sup>1</sup>, C. Parascandolo<sup>2</sup>,  
K. Rusek<sup>13</sup>, A. M. Sanchez-Benitez<sup>14</sup>, C. Signorini<sup>15</sup>, F. Soramel<sup>3,4</sup>,  
V. Soukeras<sup>1</sup>, C. Stefanini<sup>3</sup>, E. Stiliaris<sup>16</sup>, E. Strano<sup>3,4</sup>,  
I. Strojek<sup>10</sup>, D. Torresi<sup>3,4</sup>

<sup>1</sup> *Department of Physics and HINP, The University of Ioannina, 45110 Ioannina, Greece*

<sup>2</sup> *INFN, Sezione di Napoli, via Cinthia, I-80125 Napoli, Italy*

<sup>3</sup> *Dipartimento di Fisica e Astronomia, Universita di Padova, I-35131 Padova, Italy*

<sup>4</sup> *INFN, Sezione di Padova, I-35131 Padova, Italy*

<sup>5</sup> *Instituto de Fisica, Universidad Nacional Autonoma de Mexico, Mexico Distrito Federal 01000, Mexico*

<sup>6</sup> *INFN, Sezione di Catania, via S. Sofia 64, I-95125 Catania, Italy*

<sup>7</sup> *INFN, Sezione di Milano, via Celoria 16, I-20133 Milano, Italy*

<sup>8</sup> *INFN, Laboratori Nazionali del Sud, via S. Sofia 62, I-95125 Catania, Italy*

<sup>9</sup> *IFJ-PAN, Krakow, Poland*

<sup>10</sup> *National Center for Nuclear Research, A. Soltana 7, 05-400 Otwock Warsaw, Poland*

<sup>11</sup> *Dipartimento di Scienze Fisiche, Universita di Napoli "Federico II", via Cinthia, I-80125 Napoli, Italy*

<sup>12</sup> *Departamento de Fisica Aplicada, Universidad de Huelva, E-21071, Huelva, Spain*

<sup>13</sup> *Heavy Ion Laboratory, University of Warsaw, Pasteura 5a, 02-093, Warsaw, Poland*

<sup>14</sup> *Centro de Fisica Nuclear da Universidade de Lisboa, 1649-003 Lisboa, Portugal*

<sup>15</sup> *INFN, Laboratori Nazionali di Legnaro, I-35020 Legnaro, Italy*

<sup>16</sup> *Institute of Accelerating Systems and Applications and Department of Physics, University of Athens, Greece*

---

## Abstract

The production of  $\alpha$  - particles, was studied in the  ${}^7\text{Be} + {}^{28}\text{Si}$  reaction at 3 near-barrier energies, namely at 13, 20 and 22 MeV. Angular distributions

---

\*e-mail:apakou@cc.uoi.gr

were measured at each energy and the data were treated in a statistical model framework in order to disentangle the degree of competition between direct and compound channels. Into this approach the energy evolution of ratios direct versus compound nucleus formation was determined at near barrier energies. Taking into account particle multiplicities and the  $\alpha$  - production cross sections due to the compound nucleus formation, fusion cross sections were deduced and are compared to systematics.

---

## 1. Introduction

Investigations on collisions with weakly bound projectiles at near barrier energies has been proved to be a valuable tool for probing coupling channel effects. The cluster structure of such projectiles in combination with their small separation energy create a very interesting ground for studies on elastic scattering and induced reactions, as direct processes like transfer and breakup are enhanced. In this respect several studies on inclusive and exclusive measurements of light reaction products has been undertaken. Amongst them outstanding role hold the studies for the determination of fusion cross sections and the evolution of competition between direct and compound nucleus formation. We have presented in this workshop, relevant studies for the system  ${}^7\text{Be}+{}^{28}\text{Si}$  at three near barrier energies, namely 13, 20 and 22 MeV (1.1 to 1.9  $xV_{C.b.}$ ). The goal of this work was to disentangle the reaction mechanisms responsible for this light particle production and furtheron to proceed with the determination of fusion cross sections.

## 2. Experimental details and data reduction

The  ${}^7\text{Be}$  secondary beam was delivered from the EXOTIC facility [1] by means of the In Flight (IF) technique and by using a primary  ${}^7\text{Li}^{3+}$  beam at 31 MeV and 33 MeV, produced in the LNL-XTU Tandem accelerator. Details of the secondary beam  ${}^7\text{Be}$  production can be found in [2]. The  ${}^7\text{Be}$  beam was produced at 3 energies namely, 13, 20 and 22 MeV, two of them with re-tuning

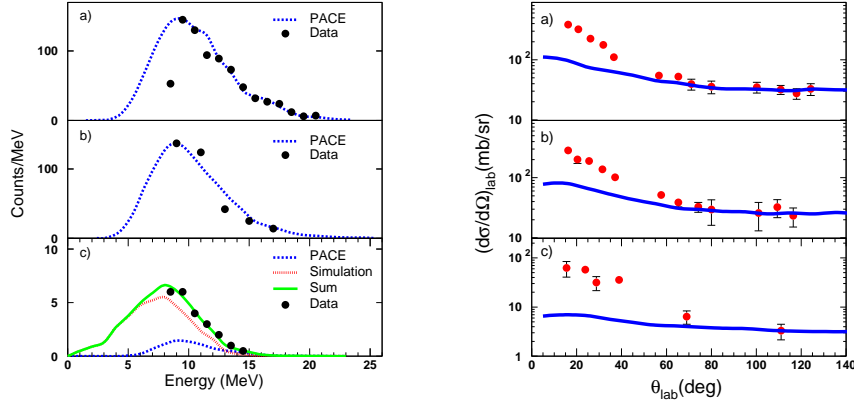


Figure 1: Left panel) Alpha energy spectra for a forward telescope at  $27^\circ$  for the three energies a) 22 MeV, b) 20 MeV and c) 13 MeV. The dashed blue line represents a simulated spectrum taking into account the evaporation of alpha particles determined via the PACE2 code. In the c) plot the dotted red line is a simulated alpha spectrum originating from direct reactions while the solid green line is the sum of direct and compound nucleus simulated alpha spectra (see text). Right panel) Angular distributions for the  $\alpha$  - particle production at a) 22 MeV, b) 20 MeV and c) 13 MeV. The solid line represents a calculation with the evaporation code PACE2 normalized to the backward angle data.

the primary beam while the lowest one was obtained via a degrader. The beam is going through two x-y sensitive Parallel Plate Avalanche Counters (PPACs) located along the beam line 909 mm (PPAC<sub>A</sub>) and 365 mm (PPAC<sub>B</sub>) upstream of the secondary target, impinging on a  $^{28}\text{Si}$  target 0.4 mg/cm<sup>2</sup> thick, and the produced reaction particles were recorded in the detector array of the EXOTIC facility.

The present setup included 6 telescopes in symmetrical positions for increasing the statistics and rule out any beam diversion. The telescopes were fixed at a distance of  $\sim 11$  cm far from the target position covering a total solid angle of 1.8sr. The trigger of the electronics was given by a signal created by the OR of the  $\Delta E$  stage of the telescopes in coincidence with the PPAC signal set. The reaction products, that is the  $\alpha$ -particles which are under study in this work, were

well separated by the  $\Delta E$ - $E$  technique and their yield for each detector and energy, were obtained by putting the appropriate windows in two dimension plots  $\Delta E$ - $E$ . Representative one dimension alpha energy spectra for one of the forward telescopes are given in the left panel of Figure 1 for each energy. Missing counts, due to the energy threshold of each telescope ( $\Delta E$  thickness) were estimated via our simulated spectra into the Monte Carlo statistical framework PACE2 [3]. For the higher energies this was a good assumption as the contribution is mainly due to evaporation and therefore, the agreement with the experimental spectrum is excellent as it can be seen in the left panel of Figure 1 for the runs at 20 and 22 MeV. For the lower energy at 13 MeV, a Monte Carlo simulation code was developed, for describing the direct channels leading to the emission of alpha particles, that is, the neutron pickup channel leading to  $^8\text{Be}$ , the neutron stripping channel leading to  $^6\text{Be}$  and the  $^3\text{He}$  - transfer channel. Energy spectra of the alpha particles for these processes were generated in our code, starting from angular distributions obtained in a Distorted Wave Born Approximation (DWBA) approach, for the production of  $^8\text{Be}$ ,  $^6\text{Be}$  and  $^4\text{He}$ . The appropriate transformations from the center of mass system to the laboratory system were obtained adopting the prescription of Olimov et al. [4]. Direct and compound nucleus spectra were summed up under various ratio assumptions of direct versus compound contributions and fitted to the data. The best fitted spectrum is shown in Figure 1c (left panel), with the solid green line.

### 3. Results and Discussion

The  $\alpha$ -particle yields for each strip, therefore for each angle, were transformed to cross sections taking into account flux and thickness of target from a simultaneous elastic scattering measurement, to be presented elsewhere. An elastic scattering measurement under the same conditions with a lead target ensured the correct determination of the solid angle. The so obtained angular distributions are given in the right panel of Figure 1.

For disentangling the compound from direct part we follow a standard tech-

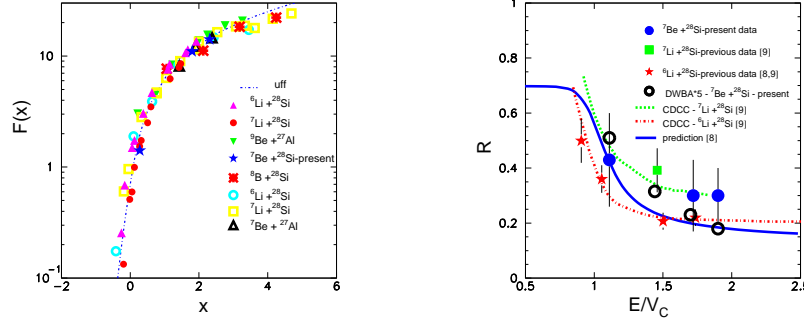


Figure 2: Left panel) Reduced fusion cross sections for various projectiles stable and radioactive on  ${}^{28}\text{Si}$  and  ${}^{27}\text{Al}$  targets. The reduction was done according to [7]. The line represents the universal function, uff, according to the same prescription [7]. Right panel) Energy evolution of ratio's,  $R$ , direct to total reaction cross sections. Present results for  ${}^7\text{Be}+{}^{28}\text{Si}$  are compared with previous results for  ${}^6\text{Li}+{}^{28}\text{Si}$ ,  ${}^7\text{Li}+{}^{28}\text{Si}$  and a phenomenological prediction outlined in Ref.[8]. Previous calculated ratios for  ${}^6\text{Li}+{}^{28}\text{Si}$  and  ${}^7\text{Li}+{}^{28}\text{Si}$ , outlined in Ref.[9], are also shown as the dot-dashed red line and dotted green line respectively. The open circles correspond to the present DWBA calculations, multiplied by 5 to match the data.

nique as applied previously for  ${}^6,7\text{Li} + {}^{28}\text{Si}$  [5, 6]. For that we have calculated in a statistical model approach the angular distribution of evaporated  $\alpha$ 's, which was renormalized to the backward detectors data. Both angular distributions, the total (experimental) and of compound nucleus origin (theoretical renormalized to experimental data), were integrated. The so obtained compound nucleus  $\alpha$ -particle production cross sections were transformed to fusion cross sections by using the appropriate multiplicities deduced from our statistical model approach. The present fusion results are compared in the left panel of Figure 2 with data reported previously for various targets at the same or similar targets, reduced to fusion functions according to the prescription of [7]. They are also compared with the universal fusion function (uff) defined in [7]. It is noted that, fusion cross sections for light weakly bound projectiles both stable and radioactive ones on low mass targets,  $A \sim 28$ , are consistent into an error of  $\sim 10\%$  with a one barrier penetration prediction.

Finally, ratios of direct to total reaction cross section,  $R = \text{direct}/\text{total}$  were

formed and are displayed in the right panel of Figure 2. It is obvious that, the present results follow in magnitude the results of  ${}^7\text{Li}$  rather than those of  ${}^6\text{Li}$ .

#### 4. Summary

The  $\alpha$ -particle production from the system  ${}^7\text{Be}+{}^{28}\text{Si}$  was studied at energies 13, 20 and 22 MeV. Direct from compound nucleus channels were disentangled via the angular distribution technique and statistical model calculations. Fusion cross sections were deduced and found to be in excellent compatibility with previous results of various projectiles ( ${}^6,{}^7\text{Li}$ ,  ${}^9\text{Be}$ ,  ${}^8\text{B}$ ) on the same and similar mass targets as well as with a simple one barrier penetration prediction. Ratio's of direct to total reaction cross section were also determined pointing out to substantial increase of direct channels at and below barrier.

*Acknowledgments:* The research leading to these results has received funding from the European Union Seventh Framework Programme FP7/2007-2013 under Grant Agreement No. 262010-ENSAR.

#### References

- [1] F. Farinon et al, Nucl. Instrum. Meth. B 266, 4097 (2008).
- [2] M. Mazzocco et al.; Phys. Rev C 92, 024615 (2015).
- [3] A. Gavron, Phys. Rev. C 21, 230 (1980).
- [4] Khusniddin K. Olimov et al., Int. J. Mod. Phys. E 25, 1650021 (2016).
- [5] A. Pakou et al, Phys. Rev. C 76, 054601 (2007).
- [6] A. Pakou, et al.; Phys. Rev. C 71, 064602 (2005).
- [7] L. F. Canto, P. R. S. Gomes, J. Lubian, L. C. Chamon, E. Crema, Nucl. Phys. A 821, 51 (2009).
- [8] A. Pakou et al.; Eur. Phys. J. A 51, 55 (2015).
- [9] A. Pakou, et al.; Eur. Phys. J. A 39, 187 (2009).

# Multi-sequential decay of $^{40}\text{Ar}$ -projectiles at 27.6 MeV/A

N.G. Nicolis  
Department of Physics  
The University of Ioannina  
Ioannina 45110, Greece

## *Abstract*

We investigate the disassembly of  $^{40}\text{Ar}$  projectiles in collisions with  $^{13}\text{C}$  and  $^{68}\text{Zn}$  at 27.6 MeV per nucleon. Experimental mass and isotopic fragment yields are compared with the predictions of our multi-sequential binary decay code MECO and other theoretical models. Many features of the experimental data are accounted for by our model. For  $^{13}\text{C}$ , the results depend critically upon the initial masses and excitation energies of the primary projectile fragments. For  $^{68}\text{Zn}$ , the experimental mass and isotopic distributions agree with the predictions of sequential binary decay models except for the heaviest fragments.

## *Introduction*

The study of projectile fragmentation reactions has been a subject of extensive experimental and theoretical interest. At energies  $\sim 20\text{MeV}/A$  several reaction mechanisms may coexist. Consequently, various models have been developed in order to study the nature of fragment multiplicities. These include cold projectile and/or target breakup, prompt fragmentation, sequential evaporation or multi-sequential decay as well as microscopic approaches (see [1] and references therein). Besides the interest in reaction mechanism studies, projectile fragmentation reactions are investigated as a means for the production of nuclei near the neutron drip line [2].

In the present paper, we report on predictions of our sequential binary decay code MECO [3,4] for the mass and isotopic distributions of  $^{40}\text{Ar}$  on  $^{13}\text{C}$  and  $^{68}\text{Zn}$  at 27.6 MeV/A. In these reactions, the excited  $^{40}\text{Ar}$  projectiles acquire high temperatures  $T \sim 5\text{-}6\text{ MeV}$  and a minimum amount of angular momentum. For this reason, they provide an appropriate testing ground for MECO. Our results are compared with experimental data and model predictions of other authors. The requirement for a simultaneous description of fragment mass and isotopic distributions imposes stringent tests on the model descriptions.

## *Model descriptions*

The code MECO [3] (Multi-sequential Evaporation COde) is a multi-step sequential binary decay code in which fragment emission may occur in both ground and excited (particle-bound or unbound) states. Gamma-decay, light-particle evaporation and IMF emission are treated in a unified framework, according to an extended Weisskopf formalism. Decays of the secondary fragments are described within the same framework, by feeding the events of the primary unbound fragments into an afterburner routine. The event structure is updated, in order to preserve correlations with the primary decay sequence. Stable primary species together with the products of secondary decays lead to the mass and charge distributions to be compared with the experiment. The validity of our approach is limited to light compound nuclei with an effective fissility parameter below the Businaro-Gallone point, characterized by an effective fissility parameter at zero spin smaller than 0.396, according to the liquid drop model [5]. Therefore, MECO is best suited for the exploration of the decay properties of excited light-mass compound nuclei.

In the following, we compare the predictions of MECO with experimental data and calculations based on the following codes:

- GEMINI [6] which is a sequential binary decay code. Emission of intermediate mass fragments is calculated with the transition stage theory. The Hauser-Feshbach formalism is used for nucleon and light cluster emission, using Fermi-gas level densities and ingoing-wave boundary condition transmission coefficients.
- In PACE2 [7], the compound nucleus is assumed to decay by n, p,  $\alpha$ ,  $\gamma$  evaporation and symmetric fission. Decay probabilities are calculated with the Hauser-Feshbach formalism, using Fermi gas level densities and optical model transmission coefficients.
- The multi-sequential decay model of Richert and Wagner [8-10]. This model is based on the temporal development of a many-body sequential evaporation of aggregates. The initial excited nucleus undergoes binary decays, the still excited daughter products continue to decay until the system does not have enough energy for aggregate decay.
- The projectile fragmentation model of Friedman [11] is based on a scenario of violent fragmentation in which the projectile breaks up suddenly into two pieces, one of which interacts with the target whereas the other one escapes.

### *The $^{40}\text{Ar} + ^{13}\text{C}$ reaction*

Experimental mass and isotopic distributions in  $^{40}\text{Ar} + ^{13}\text{C}$  collisions at  $27.5\text{ MeV}/A$  have been measured by M. Gonin et al., at the GANIL accelerator facility [12]. The analysis of experimental data suggests an incomplete fusion mechanism in which multi-sequential decay may play a non-negligible role. An analysis in terms of various theoretical models is given in references [10] and [12]. The calculated distributions seem to favour the formation of specific intermediate clusters.

We test the sensitivity of MECO calculations in A and Z of the emitting system. In Figure 1, open histograms show the experimental mass distribution in  $^{40}\text{Ar} + ^{13}\text{C}$  collisions at  $27.5\text{ MeV}/A$ . The bar histograms show the MECO calculations assuming the nuclei  $^{44}\text{Ca}$ ,  $^{45}\text{Ca}$ ,  $^{44}\text{K}$  and  $^{45}\text{Sc}$ , as emitting sources. In all cases, the initial excitation energy was set equal to  $166.375\text{ MeV}$ , corresponding to temperature  $T = 5.5\text{ MeV}$  a Fermi gas level density parameter  $k = A/8.0$ . We realize that the  $^{45}\text{Ca}$ , and  $^{45}\text{Sc}$  sources reproduce the high-A region of the mass distribution but underestimate the low-A region. The  $^{44}\text{Ca}$  and  $^{44}\text{K}$  sources produce distributions with lower mass numbers and there is a clear Z-dependence in the results. Furthermore, the region of mass numbers spanned by the calculated distributions depends on the initial excitation energy. For example, the  $^{44}\text{Ca}$  source with  $T = 5.0\text{ MeV}$  roughly reproduces the low-A wing of the experimental mass distribution. In order to reproduce the upper-A wing we need to lower the initial temperature to  $T = 4.0\text{ MeV}$ .

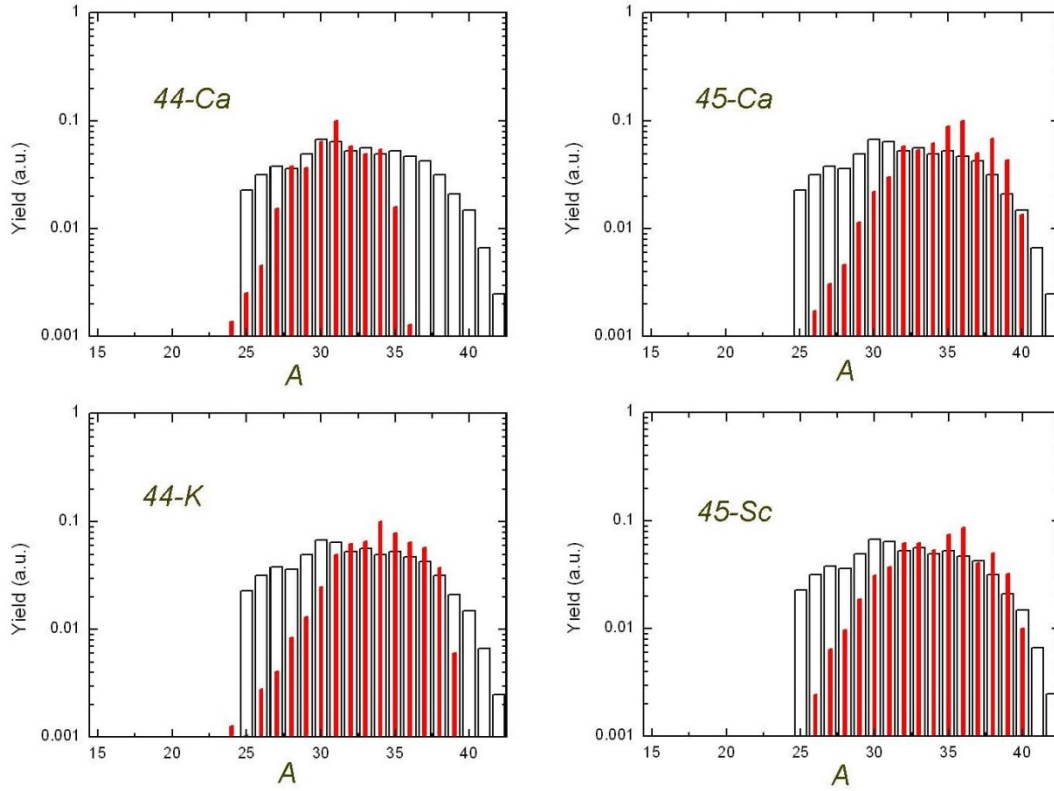


Figure 1. Experimental mass distribution in  $^{40}\text{Ar} + ^{13}\text{C}$  collisions at  $27.5\text{ MeV}/A$  and MECO calculations performed with various initial nuclei and initial excitation energy  $166.375\text{ MeV}$  (open and closed bar histograms, respectively).

In Figure 2, the experimental mass distribution is compared to calculations performed with MECO and other models. On panels (a), (b) and (c) the experimental mass distribution is indicated with the open histogram. The closed histograms are the results of calculations with MECO, GEMINI and PACE2. These calculations were performed with similar parameters. The initial spin was set to zero and the excitation energy to  $166.375\text{ MeV}$ . MECO produces a similar mass distribution to GEMINI apart from a depression of masses around  $A \sim 20$  and an excess around the peak of the distribution. Interestingly, the PACE2 calculation, which involves only nucleon and alpha emission, produces a result comparable to the other models. These calculations predict mass distributions with  $A \leq 35$ , as a result of the assumed value of the initial excitation energy. The predicted isotopic distributions by MECO and GEMINI are similar [4] and differ from the ones produced by PACE2. According to this finding the validity of the above models can be differentiated. On panel (d), the solid histogram shows the experimental and the open histogram shows the calculation of the model of Richert and Wagner with a reported initial temperature  $T = 5.5\text{ MeV}$ . This figure was reproduced from Ref. 10. The calculations in panels (a)-(c) were performed at the initial temperature  $T = 5.5\text{ MeV}$ . It seems that we need to use a lower initial temperature in order to reproduce the experimental mass distribution. In such a case, our temperature would be lower than in Ref. 10.

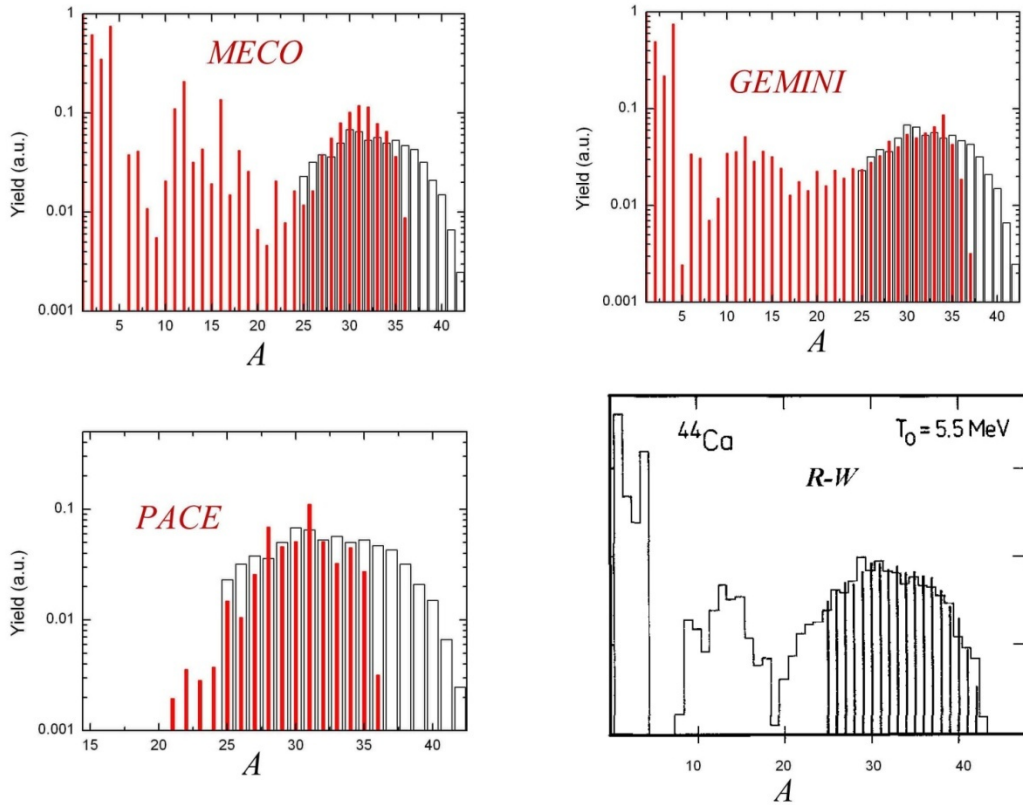


Figure 2. Experimental and calculated mass distributions in  $^{40}\text{Ar} + ^{13}\text{C}$  collisions at  $27.5 \text{ MeV}/A$  (open and solid histograms, respectively). Calculations with the indicated models refer to the initial temperature  $T = 5.5 \text{ MeV}$ .

### The $^{40}\text{Ar} + ^{68}\text{Zn}$ reaction

Mass and isotopic distributions of the reaction  $^{40}\text{Ar} + ^{68}\text{Zn}$  at  $27.6 \text{ MeV}/A$  were studied at the GANIL facility [13]. The experimental observables suggest a rather complex reaction mechanism, in which more than one emission sources have been identified. Fragments with  $6 \leq Z \leq 17$  show a remarkable stability in changes of the target nucleus (to Ni, Zn and Au), which strengthens the projectile fragmentation scenario.

The comparison of experimental isotopic distributions is shown in Fig. 3, adopted from Ref. 8. The experimental yields for  $12 \leq Z \leq 17$  are shown with crosses. Sequential binary decays of  $^{40}\text{Ar}$  were calculated with MECO assuming an initial excitation energy  $E^* = 137.5 \text{ MeV}$ , corresponding to an initial temperature  $T = 5 \text{ MeV}$  in the Fermi gas model with a level density parameter  $a = A/8$ . Results are shown in Fig. 3 with the red curves. MECO provides a good description of the distributions with  $Z = 12$  up to  $Z = 15$ . For  $Z = 16$  and  $Z = 17$ , the most neutron-rich yields are underestimated.

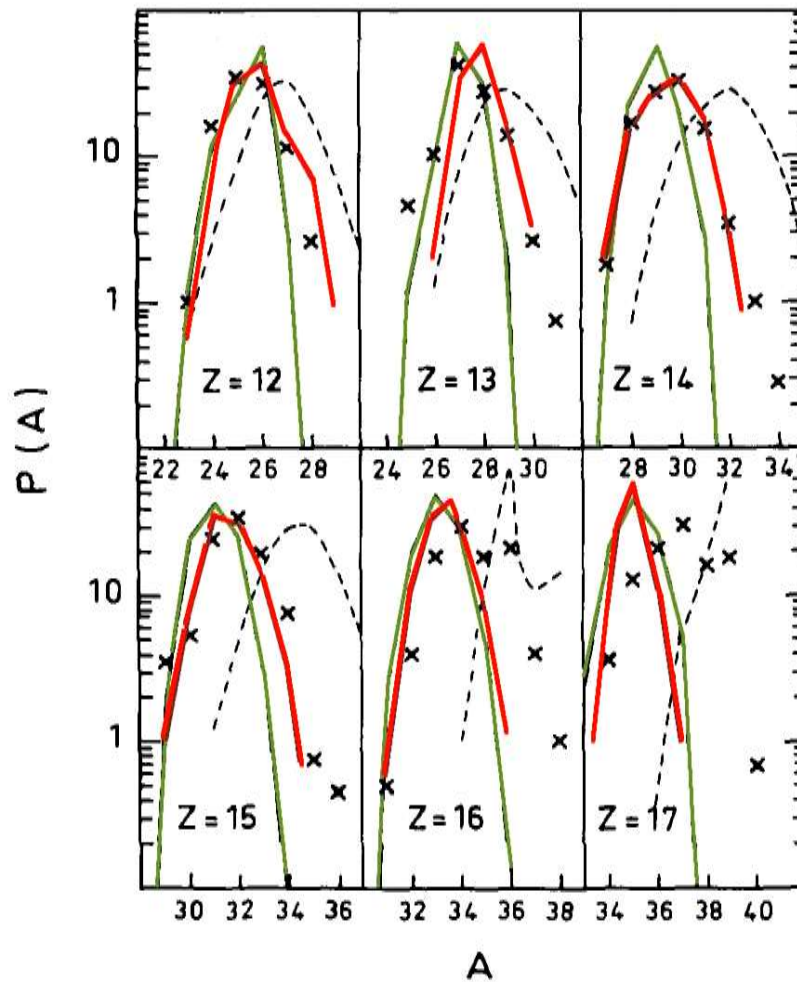


Figure 3. The crosses show the experimental isotopic distributions of fragments with  $12 \leq Z \leq 17$  from  $^{40}\text{Ar} + ^{68}\text{Zn}$  at  $27.6 \text{ MeV}/A$  [13,8]. The calculation with MECO is shown with the thick red lines. The thin green lines show the calculation with the model of Richert and Wagner [8]. The dashed lines show the result of Freedman's model [11].

In Figure 3, the green curves show the predictions of the model of Richert and Wagner, adopted from Ref. 8. We see that this model underestimates slightly the neutron-rich yields in the range  $Z = 12 - 15$  and more strongly the  $Z = 16, 17$  distributions. The narrow distributions predicted by this model has been explained as either due to unstable neutron-rich isotopes which were not taken into account in the calculation or too quick evaporation of light particles from the very beginning of  $^{40}\text{Ar}$  decay.

The dashed curves in Fig. 3, show the prediction of Freedman's model, based on the idea of violent fragmentation and subsequent absorption of one of the fragments. The calculation was adopted from Ref. 8. The predicted distributions peak at a higher mass number than the data. The disagreement deteriorates with increasing atomic number of the fragment. The model disagrees with the data completely for  $Z = 16, 17$ .

As far as the interpretation of the data is concerned, we realize a consistency with a mechanism of sequential binary decay for  $Z = 6 - 13$  but not for fragments with  $Z \geq 13$ , which are probably populated in peripheral collisions. Compared to the model of Richert and Wagner, MECO provides a slightly better description of the experimental isotopic distributions for  $12 \leq Z \leq 15$  and similar results to Reichert and Wagner for  $Z = 16, 17$ . However, we note that the similarity of the two calculations was achieved with a lower temperature in MECO ( $T = 5.0 \text{ MeV}$ ) compared to the model of Richert and Wagner ( $T = 6.0 \text{ MeV}$ ).

### Summary

We presented mass and isotopic distributions from the de-excitation of  $^{40}\text{Ar}$  projectiles calculated with our multi-sequential binary decay code MECO. Comparisons were made with experimental data from  $^{40}\text{Ar}$  collisions on  $^{13}\text{C}$  and  $^{64}\text{Zn}$  at  $27.6 \text{ MeV}$ , as well as other theoretical models. A simultaneous description of mass and isotopic distributions favours multi-sequential binary decay models over simple evaporation models involving nucleon and alpha-particle evaporation. In these reaction systems, the results of MECO are similar to GEMINI. For  $^{40}\text{Ar} + ^{13}\text{C}$ , the calculations depend critically upon the initial masses and excitation energies of the primary projectile fragments. For  $^{40}\text{Ar} + ^{68}\text{Zn}$ , the experimental mass and isotopic distributions agree with the predictions of sequential binary decay models except for the heaviest fragments. MECO provides a slightly better description of the isotopic distributions than the model of Reichert and Wagner, which provides a better overall description of the data. Our model could provide a similar overall description of the data if a lower initial temperature for the excited Ar fragments was assumed than the one previously reported in the literature.

### References

- [1] M. Geraci et al., Nucl. Phys. A 773 (2006) 1-6.
- [2] M. Notani et al., Phys. Rev. C 76, 044605 (2007).
- [3] N.G. Nicolis, Int.J.Mod.Phys. E17, 1541 (2008).
- [4] N.G. Nicolis, Proceedings of the 16<sup>th</sup> Symposium of the Hellenic Nuclear Physics Society, p. 83, National & Kapodistrian University of Athens, 26-27 May 2006.
- [5] L.G. Moretto and G.J. Wozniak, Prog. Part. Nucl. Phys. 21, 401 (1988).
- [6] R.J. Charity et al., Nucl. Phys. A483, 317(1988).
- [7] A. Gavron, Phys. Rev. C21, 230 (1980).
- [8] J. Richert and P. Wagner, Nucl. Phys. A466, 132 (1987).
- [9] C. Barbagallo, J. Richert and P. Wagner, Z. Phys. A324, 97-106 (1986).
- [10] J. Richert and P. Wagner, Z. Phys. A330, 283-288 (1988).
- [11] W.A. Friedman, Phys. Rev. C27, 569 (1983).
- [12] M. Gonin et al., Phys. Rev. C 38, 135 (1988).
- [13] F. Rami et al., Nucl. Phys. A444, 325 (1985).

# Production of rare isotopes toward the astrophysical r-process path

G.A. Souliotis<sup>a,\*</sup>, A. Papageorgiou<sup>a</sup>, Y.K. Kwon<sup>b</sup>, K. Tshoo<sup>b</sup>,  
S. C. Jeong<sup>b</sup>, M. Veselsky<sup>c</sup>, A. Bonasera<sup>d,e</sup>

<sup>a</sup> *Laboratory of Physical Chemistry, Department of Chemistry, National and Kapodistrian University of Athens, Athens, Greece*

<sup>b</sup> *The Rare Isotope Science Project (RISP), Institute for Basic Science, Daejeon, Korea.*

<sup>c</sup> *Institute of Physics, Slovak Academy of Sciences, Bratislava, Slovakia*

<sup>d</sup> *Cyclotron Institute, Texas A&M University, College Station, Texas, USA*

<sup>e</sup> *Laboratori Nazionali del Sud, INFN, Catania, Italy*

\* *Corresponding author. Email: soulioti@chem.uoa.gr*

---

## Abstract

The production cross sections of projectile-like fragments from collisions of  $^{86}\text{Kr}$  projectiles with  $^{64,58}\text{Ni}$  and  $^{124,112}\text{Sn}$  targets at 15 and 25 MeV/nucleon are studied systematically with emphasis on the neutron-rich isotopes. Our recent experimental data are compared with calculations employing a hybrid approach. The dynamical stage of the projectile-target interaction was described with either the phenomenological deep-inelastic transfer (DIT) model or the microscopic constrained molecular dynamics model (CoMD). For the de-excitation of projectile-like fragments, the statistical multifragmentation model (SMM) or the binary-decay code GEMINI were employed. A good agreement with the experimental results was obtained. We point out that our current understanding of the reaction mechanism at beam energies below the Fermi energy suggests that such nuclear reactions, involving peripheral nucleon exchange, can be exploited as a novel route to access extremely neutron-rich isotopes toward the r-process path and the hard-to-reach neutron drip-line.

---

## 1 Introduction

The study of the nuclear landscape toward the astrophysical r-process path and the neutron drip-line have recently received special attention by the nuclear physics community (see, e.g., [1,2] and references therein). Closely related

to this effort is the efficient production of very neutron-rich nuclides which constitutes a central issue in current and future rare isotope beam facilities (see, e.g., [3–12]).

Neutron-rich nuclides are mainly produced by spallation, fission and projectile fragmentation [13]. Spallation is an efficient mechanism to produce rare isotopes for ISOL-type techniques [14]. Projectile fission is appropriate in the region of light and heavy fission fragments (see, e.g., [15] for recent efforts on  $^{238}\text{U}$  projectile fission). Finally, projectile fragmentation offers a universal approach to produce exotic nuclei at beam energies above 100 MeV/nucleon (see, e.g., [16,17]). This approach is, nevertheless, based on the fact that optimum neutron excess in the fragments is achieved by stripping the maximum possible number of protons (and a minimum possible number of neutrons).

To reach a high neutron-excess in the products, apart from proton stripping, it may be necessary to capture neutrons from the target. Such a possibility is offered by reactions of nucleon exchange at beam energies from the Coulomb barrier [18,19] to the Fermi energy (20–40 MeV/nucleon) [20,21]. Detailed experimental data in this broad energy range are scarce at present [19,22,23]. In multinucleon transfer and deep-inelastic reactions near the Coulomb barrier [19], the low velocities of the fragments and the wide angular and ionic charge state distributions may limit the collection efficiency for the most neutron-rich products. The reactions in the Fermi energy regime combine the advantages of both low-energy (i.e., near and above the Coulomb barrier) and high-energy (i.e., above 100 MeV/nucleon) reactions. At this energy, the synergy of the projectile and the target enhances the  $N/Z$  of the fragments, while the velocities are high enough to allow efficient in-flight collection and separation.

Our initial experimental studies of projectile fragments from 25 MeV/nucleon reactions of  $^{86}\text{Kr}$  on  $^{64}\text{Ni}$  [20] and  $^{124}\text{Sn}$  [21] indicated substantial production of neutron-rich fragments. Motivated by recent developments in several facilities that will offer either very intense primary beams [5,8] at this energy range or re-accelerated rare isotope beams [4,5,8,9], we continued our experimental studies at 15 MeV/nucleon [24]. In this contribution, after a short overview of the experimental measurements, we present a systematic calculation of the production cross sections based on either the phenomenological deep-inelastic transfer (DIT) model or the microscopic constrained molecular dynamics model (CoMD). The good description of the experimental results with the CoMD code, as well as, with a properly modified version of the DIT code, suggest the possibility of using the present theoretical framework for the prediction of exotic nuclei employing radioactive beams that will soon be available in upcoming facilities. As an example, we present the production cross sections and the rates of neutron-rich nuclei using a radioactive beam of  $^{92}\text{Kr}$  at 15 MeV/nucleon.

## 2 Outline of Results and Comparisons

A detailed presentation of the experimental results appear in [24] in which the mass spectrometric measurements of production cross sections of neutron-rich projectile fragments from the reactions of a 15 MeV/nucleon  $^{86}\text{Kr}$  beam with  $^{64}\text{Ni}$ ,  $^{58}\text{Ni}$  and  $^{124}\text{Sn}$ ,  $^{112}\text{Sn}$  targets are given. We also note that the experimental results of the 25MeV/nucleon reactions and the relevant procedures are described in detail in our articles [20–23].

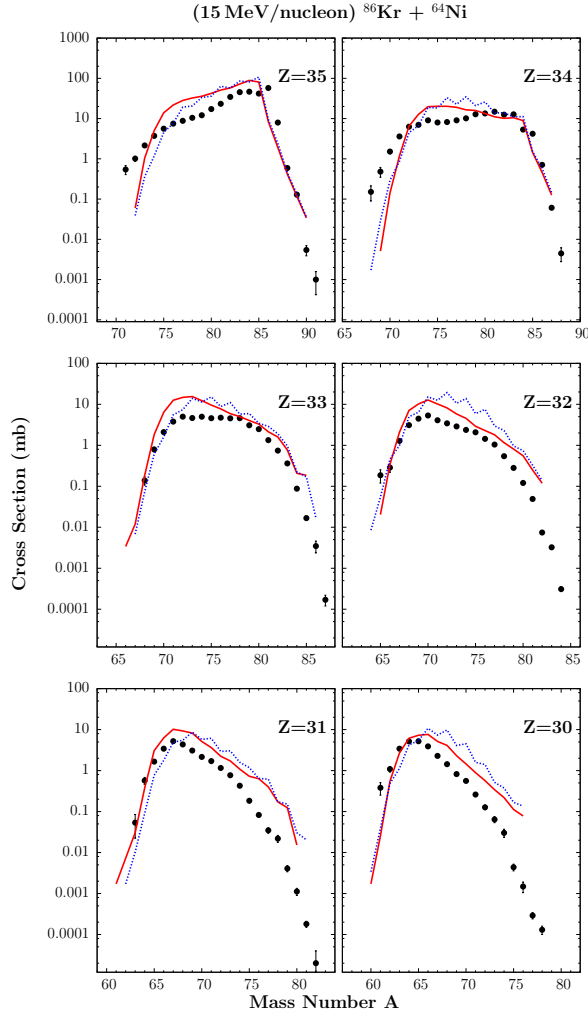


Fig. 1. (Color online) Experimental mass distributions (symbols) of elements with  $Z = 35\text{--}30$  observed in the reaction  $^{86}\text{Kr}(15\text{ MeV/nucleon})+^{64}\text{Ni}$  [24] compared to the results of CoMD/SMM calculations (solid red line) and CoMD/GEMINI calculations (dotted blue line).

In Fig. 1 we present the experimental mass distributions of elements with  $Z = 35\text{--}30$  of the reaction  $^{86}\text{Kr}(15\text{ MeV/nucleon})+^{64}\text{Ni}$  [24] compared to the calculations with the CoMD code [25,26] combined with the de-excitation codes SMM [27] (solid line) and GEMINI [28] (dotted line), used for the de-

excitation of the quasiprojectiles emerging after the dynamical stage. The results of the calculations are in overall agreement with the experimental data especially for the isotopes close to the projectile with  $Z = 35$ – $32$ . We also observe that the microscopic CoMD model is able to describe even the rare neutron-rich products from this reaction that are the products for our main interest. The overestimation of the cross sections for the products with  $Z = 31, 30$  is related to issues of the excitation energy as calculated by CoMD and are currently under further investigation.

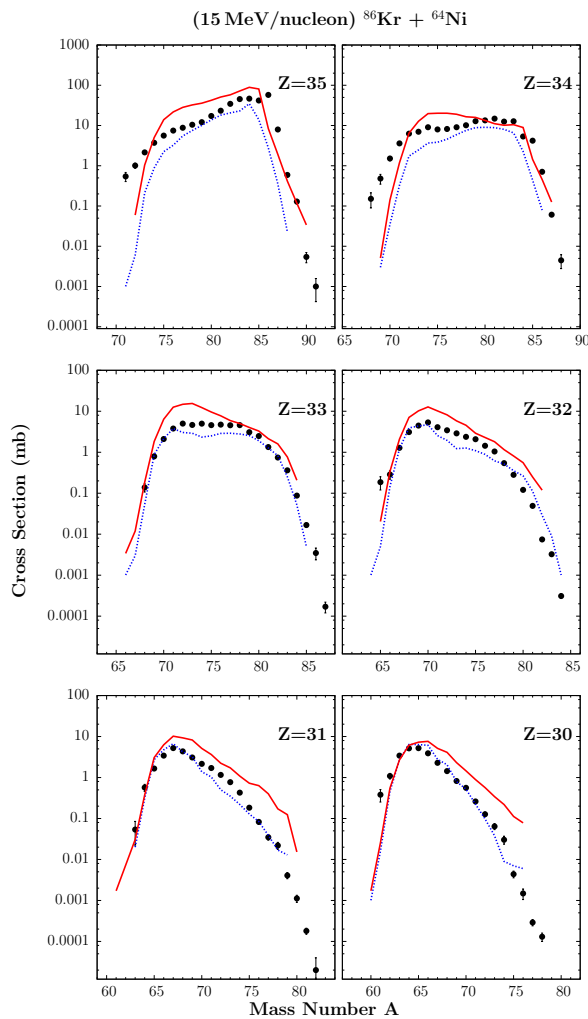


Fig. 2. (Color online) Experimental mass distributions (symbols) of elements with  $Z = 35$ – $30$  observed in the reaction  $^{86}\text{Kr}(15 \text{ MeV/nucleon}) + ^{64}\text{Ni}$  [24] compared to the results of CoMD/SMM calculations (solid red line) and DITm/SMM calculations (dotted blue line).

Subsequently, motivated by our previous studies [20,21], we employed Tassan-Got's phenomenological model of deep inelastic transfer (DIT) [29] coupled with SMM [27] or GEMINI [28]. The results of this standard version of DIT were not satisfactory. We thus proceeded with our modified version of the DIT model (DITm) [30] in which we have introduced a detailed description of

the nuclear surface and the neutron skin of the involved nuclei. In Fig 2, we present the experimental mass distributions of elements with  $Z = 35-30$  of the reaction  $^{86}\text{Kr}(15 \text{ MeV/nucleon})+^{64}\text{Ni}$  [24] and compare them to the results of the modified DIT (DITm) calculations (dotted line) and to the results of the CoMD calculations (solid line) using SMM as the de-excitation code. From this figure we observe that the modified DIT code describes the experimental results rather well at these beam energies. Moreover, it can better describe the products further away from the projectile, that cannot be well described by CoMD, as we mentioned previously.

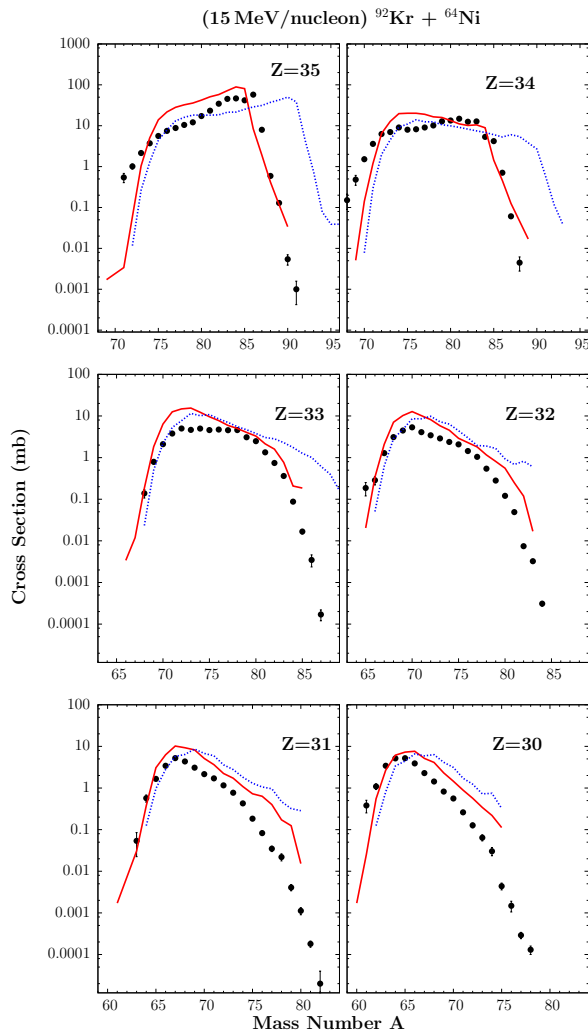


Fig. 3. (Color online) Experimental mass distributions (symbols) of elements with  $Z = 35-30$  observed in the reaction  $^{86}\text{Kr}(15 \text{ MeV/nucleon})+^{64}\text{Ni}$  [24], calculations CoMD/SMM for the reaction  $^{86}\text{Kr}(15 \text{ MeV/nucleon})+^{64}\text{Ni}$  (solid red line), calculations CoMD/SMM for the reaction  $^{92}\text{Kr}(15 \text{ MeV/nucleon})+^{64}\text{Ni}$  (dotted blue line).

We mention that a thorough comparison of the data with the calculations for the 15 MeV/nucleon, as well as the 25 MeV/nucleon reactions has been performed that appears in [31]. After this systematic comparison of the calculations with the experimental data of the stable  $^{86}\text{Kr}$  beam, we proceeded to

Table 1

Cross sections and rate estimates (last column) of very neutron-rich isotopes from the reaction  $^{92}\text{Kr}$  (15 MeV/nucleon) +  $^{64}\text{Ni}$ . For the rates, a radioactive beam of  $^{92}\text{Kr}$  with intensity 0.5 pnA ( $3.1 \times 10^9$  particles/sec) is assumed to interact with a  $^{64}\text{Ni}$  target of 20 mg/cm<sup>2</sup> thickness.

Rare Isotope	Reaction Channel	Cross Section (mb)	Rate (sec <sup>-1</sup> )
$^{93}\text{Kr}$	-0p+1n	18.8	$1.1 \times 10^4$
$^{94}\text{Kr}$	-0p+2n	2.3	$1.3 \times 10^3$
$^{95}\text{Kr}$	-0p+3n	0.63	$3.8 \times 10^2$
$^{96}\text{Kr}$	-0p+4n	0.2	$1.2 \times 10^2$
$^{92}\text{Br}$	-1p+1n	4.5	$2.7 \times 10^3$
$^{93}\text{Br}$	-1p+2n	0.75	$4.5 \times 10^2$
$^{94}\text{Br}$	-1p+3n	0.078	47
$^{95}\text{Br}$	-1p+4n	0.040	23
$^{96}\text{Br}$	-1p+5n	0.008	5
$^{90}\text{Se}$	-2p+0n	2.7	$1.6 \times 10^3$
$^{91}\text{Se}$	-2p+1n	0.6	$3.5 \times 10^2$
$^{92}\text{Se}$	-2p+2n	0.12	70
$^{93}\text{Se}$	-2p+3n	0.04	23

investigate what results we would obtain by using a neutron-rich radioactive beam, such as  $^{92}\text{Kr}$ . In Fig. 3 we present again the experimental mass distributions (black symbols) of the reaction  $^{86}\text{Kr}(15 \text{ MeV/nucleon})+^{64}\text{Ni}$ , the CoMD/SMM calculations for this reaction (solid line) and, furthermore, the CoMD/SMM calculations for the reaction  $^{92}\text{Kr}(15 \text{ MeV/nucleon})+^{64}\text{Ni}$  (dotted line). We observe that by using the neutron-rich radioactive beam of  $^{92}\text{Kr}$ , we obtain more neutron-rich products. This is primarily true for the isotopes near the projectile. We point out that, e.g., for bromine ( $Z=35$ ), isotopes that have up to 15 more neutrons ( $A = 96$ ) than the corresponding stable isotope ( $A = 81$ ) can be obtained. This observation indicates that by using neutron-rich radioactive beams, and through the mechanism of peripheral multinucleon transfer, we will have the possibility to produce even more neutron-rich nuclides toward neutron drip line.

In Table I, we present the predicted cross-sections and the production rates of neutron rich isotopes from the reaction of the radioactive beam of  $^{92}\text{Kr}$  (15

MeV/nucleon) with  $^{64}\text{Ni}$ . For the rate calculations, the  $^{92}\text{Kr}$  beam with intensity  $0.5\text{ pA}$  ( $3.1 \times 10^9$  particles/sec) is assumed to interact with a  $^{64}\text{Ni}$  target of  $20\text{ mg/cm}^2$  thickness. We see that we have the possibility to produce extremely neutron-rich isotopes in these energies with the use of re-accelerated radioactive beams, such as  $^{92}\text{Kr}$ , that will be available in upcoming rare-isotope facilities (e.g. [10,11]).

### 3 Summary and Conclusions

In summary, we performed a systematic study of the production cross sections of projectile-like fragments from collisions of  $^{86}\text{Kr}$  projectiles with  $^{64,58}\text{Ni}$  and  $^{124,112}\text{Sn}$  targets at 15 and 25 MeV/nucleon with emphasis on the neutron-rich isotopes. Our experimental data were compared with systematic calculations employing a two-step approach. The calculations for the dynamical stage of the projectile-target interaction were carried out using either the phenomenological deep-inelastic transfer (DIT) model or the microscopic constrained molecular dynamics model (CoMD). For the de-excitation of the projectile-like fragments, the statistical multifragmentation model (SMM) or the binary-decay code GEMINI were employed. An overall good agreement with the experimental results was observed. With the current understanding of the reaction mechanism at these beam energies, we suggest that these nuclear reactions, involving peripheral nucleon exchange, be exploited as an efficient route to access neutron-rich rare isotopes toward the r-process path and the neutron drip-line. Therefore, future experiments in several accelerator facilities [13] can be planned that will enable a variety of nuclear structure and nuclear reaction studies in unexplored regions of the nuclear chart.

### References

- [1] J. Erler et al, *Nature* **486**, 509 (2011).
- [2] J. Äystö, W. Nazarewicz, M. Pfützner, C. Signorini, eds, Proceedings of the Fifth International Conference on Exotic Nuclei and Atomic Masses (ENAM'08), Ryn, Poland, September 7–13 (2008); *Eur. Phys. J. A* **42** (2009).
- [3] D. F. Geesaman, C. K. Gelbke, R. V. F. Janssens, B. M. Sherrill, *Ann. Rev. Nucl. Part. Sci.* **56**, 53 (2006)
- [4] FRIB main page: [www.frib.msu.edu](http://www.frib.msu.edu)
- [5] GANIL main page: [www.ganil.fr](http://www.ganil.fr)
- [6] GSI main page: [www.gsi.de](http://www.gsi.de)

- [7] RIBF main page: [www.rarf.riken.go.jp/Eng/facilities/RIBF.html](http://www.rarf.riken.go.jp/Eng/facilities/RIBF.html)
- [8] ATLAS main page: [www.phy.anl.gov/atlas/facility/index.html](http://www.phy.anl.gov/atlas/facility/index.html)
- [9] EURISOL main page: [www.eurisol.org](http://www.eurisol.org)
- [10] RISP main page: [www.risp.re.kr/eng/pMainPage.do](http://www.risp.re.kr/eng/pMainPage.do)
- [11] K. Tshoo, Y. K. Kim, Y. K. Kwon et al, Nucl. Instrum. Methods B **317**, 242 (2013).
- [12] K. Tshoo, H. Chae, J. Park, J.Y. Moon, Y.K. Kwon, G.A. Souliotis et al, Nucl. Instrum. Methods B **376**, 188 (2016).
- [13] Y. Blumenfeld, T. Nilsson and P. Van Duppen, Phys. Scr. T152 014023 (2013).
- [14] A. Kelić, M. V. Ricciardi, K. -H. Schmidt, BgNS Transactions, **13**, 98 (2009).
- [15] H. Alvarez-Pol et al., Phys. Rev. C **82**, 041602 (2010).
- [16] O. B. Tarasov et al., Phys. Rev. C **80**, 034609 (2009).
- [17] S. Lukyanov et al., Phys. Rev. C **80**, 014609 (2009).
- [18] V. V. Volkov, Phys. Rep. **44**, 93 (1978).
- [19] L. Corradi, G. Pollarolo, S. Szilner, J. Phys. G **36**, 113101 (2009).
- [20] G. A. Souliotis et al., Phys. Lett. B **543**, 163 (2002).
- [21] G. A. Souliotis et al., Phys. Rev. Lett. **91**, 022701 (2003).
- [22] G. A. Souliotis et al., Nucl. Instrum. Methods **B 204** 166 (2003).
- [23] G. A. Souliotis et al., Nucl. Instrum. Methods **B 266**, 4692 (2008).
- [24] G. A. Souliotis et al., Phys. Rev. C **84**, 064607 (2011).
- [25] M. Papa et al., Phys. Rev. C **64**, 024612 (2001).
- [26] M. Papa et al, J. Comp. Phys. **208**, 403 (2005).
- [27] J. Bondorf et al., Phys. Rep. **257**, 133 (1995).
- [28] R. Charity et al., Nucl. Phys. **A 483**, 391 (1988); Phys. Rev. C **58**, 1073 (1998).
- [29] L. Tassan-Got and C. Stephan, Nucl. Phys. **A 524**, 121 (1991).
- [30] M. Veselsky and G.A. Souliotis, Nucl. Phys. **A 765**, 252 (2006).
- [31] P.N. Fountas, G.A. Souliotis, M. Veselsky and A. Bonasera, Phys. Rev. C **90**, 064613 (2014).

# Neutron-Rich Isotope Production in $^{238}\text{U}$ Projectile Fission at 20 MeV/nucleon

N. Vonta<sup>a</sup>, G.A. Souliotis<sup>a,\*</sup>, Y.K. Kwon<sup>b</sup>, K. Tshoo<sup>b</sup>,  
S. C. Jeong<sup>b</sup>, M. Veselsky<sup>c</sup>, A. Bonasera<sup>d,e</sup>

<sup>a</sup> *Laboratory of Physical Chemistry, Department of Chemistry, National and Kapodistrian University of Athens, Athens, Greece*

<sup>b</sup> *The Rare Isotope Science Project (RISP), Institute for Basic Science, Daejeon, Korea.*

<sup>c</sup> *Institute of Physics, Slovak Academy of Sciences, Bratislava, Slovakia*

<sup>d</sup> *Cyclotron Institute, Texas A&M University, College Station, Texas, USA*

<sup>e</sup> *Laboratori Nazionali del Sud, INFN, Catania, Italy*

\* *Corresponding author. Email: soulioti@chem.uoa.gr*

---

## Abstract

The present report describes our continued efforts to study the production of neutron-rich nuclides in projectile fission of  $^{238}\text{U}$  beams in the energy range of 20 MeV/nucleon expected from the RISP accelerator complex. We report our efforts to systematically model the reaction mechanism at this energy range using the Deep Inelastic Transfer (DIT) model or the Constrained Dynamics Model followed by the Statistical Multifragmentation Model (SMM). We compared our model calculations with our previous data of  $^{238}\text{U}$  (20 MeV/nucleon)+ $^{208}\text{Pb}$  and  $^{197}\text{Au}$  (20 MeV/nucleon)+ $^{197}\text{Au}$  and found reasonable agreement, especially for the neutron-rich side of the distributions. We plan to systematically study the optimum projectile, target and energy combinations for the production of neutron-rich rare isotopes at KOBRA using the approach of projectile fission in the energy range of 20 MeV/nucleon.

---

## 1 Introduction

We have recently presented our efforts to study the production of neutron-rich rare isotopes employing the mechanism of multinucleon transfer with stable or radioactive beams in the energy range 15–25 MeV/nucleon expected from low-energy facilities (e.g. the RISP accelerator facility [1–5]). Our recent article [6]

describes our current theoretical understanding and computational description of the reaction mechanism for near projectile fragments for which substantial experimental effort has been devoted by us in recent years [7–11].

In this contribution, we present our efforts to systematically model the reaction mechanism at this energy range. For this purpose, we first used the deep-inelastic transfer (DIT) model, as well as the Constrained Dynamics Models for the description of the multinucleon transfer stage of the projectile–target interaction. The excited quasiprojectiles were then de-excited with the statistical multifragmentation model (SMM), with appropriate setting of the parameters to describe fission as a low-energy binary division (i.e. treated as a special case of nuclear multifragmentation). We compared our model calculations with our previous data [12–14] of  $^{238}\text{U}$  (20 MeV/nucleon)+ $^{208}\text{Pb}$  and  $^{197}\text{Au}$  (20 MeV/nucleon) +  $^{197}\text{Au}$  and found reasonable agreement as we will discuss below.

We are now equipped with a reliable model framework to describe projectile fission and we plan to explore various combinations of projectile, target and energy to optimize the production of very neutron-rich (and possibly new) rare isotopes at KOBRA. We expect that our progress on the study of projectile-fission reactions using heavy beams of 20 MeV/nucleon will have important contribution and application to the unique capabilities of the KOBRA/RISP facility, opening up new world-class opportunities in neutron-rich rare-isotope nuclear and astrophysical research.

## 2 Study of Neutron-Rich nuclide production in $^{238}\text{U}$ and $^{197}\text{Au}$ projectile fission at 20 MeV/nucleon

In Fig. 1, we present the experimental mass distributions (closed points) of several elements from the projectile fission of  $^{238}\text{U}$  (20 MeV/nucleon) interacting with the  $^{208}\text{Pb}$  target [12]. The DIT/SMM calculations are given by the solid (red) lines and the CoMD/SMM calculations by the dotted (blue) lines. These two calculations are close to each other on the neutron-rich side, while the latter calculations are systematically lower in the central region of the distributions. From the figure, we observe some agreement in the shape of the calculations with the experimental cross sections. More specifically, we are able to obtain a relatively good description of the neutron-rich sides of the isotope distributions, which consists the primary interest of the present work. For the neutron deficient sides, the present calculations extent more to the left compared to the experimental data. We explored this issue in detail and concluded that in the experimental data, the magnetic rigidity range did not extend to the low- $B\rho$  region necessary for these isotopes. It is thus clear that, in order to avoid such issues in upcoming experiments, careful consid-

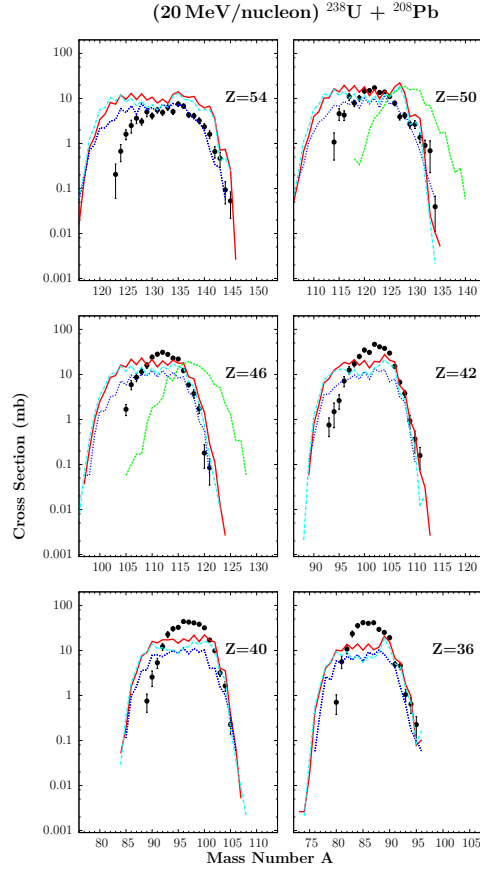


Fig. 1. (Color online) Comparison of calculated mass distributions (lines) of projectile fission fragments from the reaction  $^{238}\text{U}$  (20 MeV/nucleon) +  $^{208}\text{Pb}$  with the experimental data (closed points) of [12]. The calculations are with DIT/SMM [solid (red) line] and with CoMD/SMM [dotted (blue) line]. The dashed (green) lines for  $Z=46,50$  are for hot fission fragments from DIT/SMM. The dot-dashed (light blue) lines are from  $^{238}\text{U}$  (20 MeV/nucleon) +  $^{64}\text{Ni}$ .

eration should be given to the necessary of  $B\rho$  coverage that is possible to be predicted with the help of the present model framework. Moreover, in Fig. 1 the dashed green lines (for  $Z = 46, 50$ ) show the distributions of the hot fission fragments (after binary partition, but before deexcitation in SMM). As we discussed before, these products are very neutron-rich and deexcite toward more stable nuclides.

Finally, in Fig. 1 we present the DIT/SMM calculations [dot-dashed (light blue) lines] for projectile fission fragments from the interaction of  $^{238}\text{U}$  (20 MeV/nucleon) with the lighter  $^{64}\text{Ni}$ . The cross sections are very close to those of the U+Pb reaction [solid (red) lines], but the angular distributions are narrower (as we discuss later in relation to Fig. 3) rendering the use of the lighter target preferable for applications to neutron-rich RIB production.

In Fig. 2, we turn our attention to the projectile fission of  $^{197}\text{Au}$  (20 MeV/nucleon) interacting with a  $^{197}\text{Au}$  target. This reaction was studied as part of our ex-

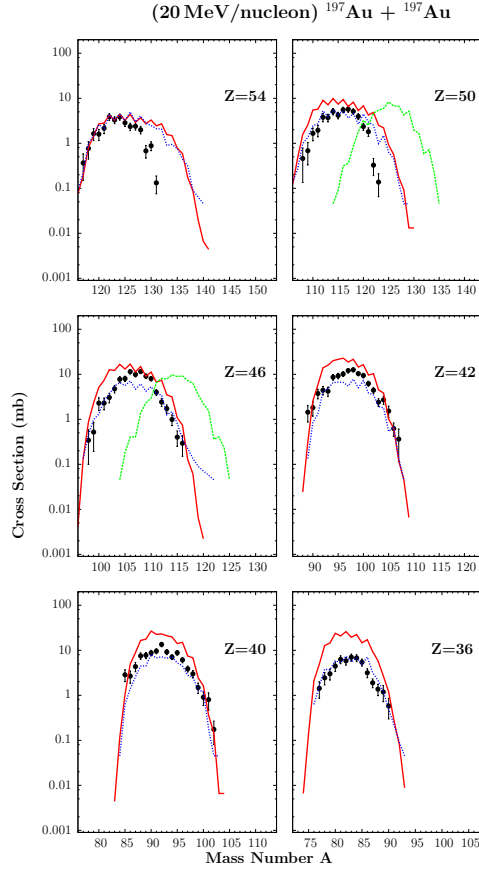


Fig. 2. (Color online) Comparison of calculated mass distributions (lines) of projectile fission fragments from the reaction  $^{197}\text{Au}$  (20 MeV/nucleon) +  $^{197}\text{Au}$  with the experimental data (closed points) of [14]. The calculations are with DIT/SMM [solid (red) line] and with CoMD/SMM [dotted (blue) line]. The dashed (green) lines for  $Z=46,50$  are for hot fission fragments from DIT/SMM.

tended study of Au-induced reactions at NSCL/MSU [28,14]. The Au+Au data were recently fully analyzed for the purpose of this work. The general behavior of the data in comparison to our calculations is similar to that of U+Pb, we thus show here only the yield distributions of several fission fragments. In Fig. 2, the experimental mass distributions are shown by full points. We see some disagreement between the data and the DIT/SMM calculations [full (red) lines] and the CoMD/SMM calculations [dotted (blue) lines] at the neutron-rich side for the heavier fission fragments ( $Z=54, 50$  in the figure). We may attribute these discrepancies, in part, to incomplete  $B\rho$  coverage during the experimental measurements [14]. For the lower elements, we observe that the CoMD/SMM calculations are in good agreement with the data, whereas the DIT/SMM calculations are higher than the data. The differences between the calculations may be due to differences in the excitation energy distributions of the primary quasiprojectiles predicted by the two different dynamical codes. We understand that the beam of  $^{197}\text{Au}$  ( $N/Z = 2.49$ ) is not the optimum choice for the production of neutron-rich isotopes in projectile fission,

compared, of course, to the  $^{238}\text{U}$  ( $N/Z=2.59$ ) beam. Nevertheless, the Au+Au data offer additional detailed testing of our model framework.

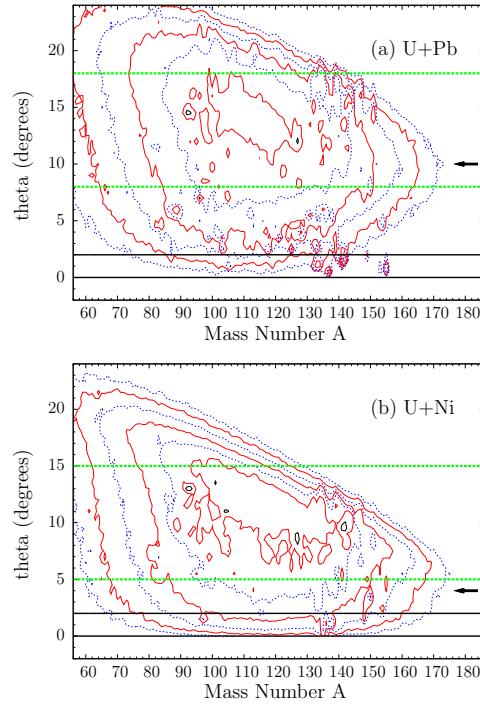


Fig. 3. (Color online) (a) DIT/SMM calculated mass-resolved angular distributions of projectile fission fragments from the reaction  $^{238}\text{U}$  (20 MeV/nucleon) +  $^{208}\text{Pb}$ . The successive contours (starting from the innermost) represent a drop in the yield by a factor of two. The horizontal lines represent the polar angular acceptance of: the A1200 spectrometer setup [12] (lower solid lines) and the KOBRA spectrometer [33] (upper dashed lines) (see text). The arrow indicates the grazing angle of the U+Pb reaction (in the lab system). (b) As in (a), but for the reaction  $^{238}\text{U}$  (20 MeV/nucleon) +  $^{64}\text{Ni}$  (see text).

To understand the kinematics and the angular spread of the fission fragments from the projectile fission of  $^{238}\text{U}$  at 20 MeV/nucleon, in Fig. 3a we show the DIT/SMM calculated mass-resolved angular distributions for U+Pb. The successive contours (starting from the innermost) represent a drop in the yield by a factor of two. The (lower) horizontal full lines represent the polar angular acceptance of the A1200 spectrometer in the experimental setup of [12]. The (upper) horizontal dashed lines indicate the angular acceptance of the KOBRA separator [33], that we consider as a representative large acceptance separator appropriate for rare isotope production at this energy regime. In the KOBRA setup, we assume that the beam hits the primary target at an angle of  $6^\circ$  (that may be achieved with the aid of an appropriate beam swinger system [33]) and fragments are collected in the polar angular range of  $8^\circ$ – $18^\circ$ . From the figure, we see the issue of the very small acceptance of our setup in the original A1200 separator scheme. A fraction on the order of 1% or smaller of the produced projectile fission fragments falls in the angular acceptance of the

A1200 spectrometer. However, with an advanced large-acceptance separator like KOBRA, a substantial fraction of the projectile-fission fragments (that can reach 30–50%) can be collected, provided that we swing the primary beam at an appropriate angle (that we can choose to be near the grazing angle of the reaction).

In Fig. 3b, we show the mass resolved angular distributions for the reaction of  $^{238}\text{U}$  (20 MeV/nucleon) with the lighter target of  $^{64}\text{Ni}$ . The grazing angle for this system is  $\sim 4.0^\circ$ , much smaller than the U+Pb system at 20 MeV/nucleon. We clearly see that the angular distributions of the projectile fission fragments are narrower, allowing, of course, a more efficient collection by the separator. For this reaction, we may assume that the beam hits the primary target at an angle of  $3^\circ$  in the KOBRA setup and fragments are collected in the polar angular range of  $5^\circ$ – $10^\circ$ .

We note that our choice of  $^{208}\text{Pb}$  ( $N/Z=1.54$ ) as a target [12] was based on its large  $N/Z$ . However, with our present reaction model framework, we find that the calculated production cross sections of neutron-rich projectile fission fragments using the lighter  $^{64}\text{Ni}$  ( $N/Z=1.29$ ) target are nearly similar to those coming from reaction using the more neutron-rich  $^{208}\text{Pb}$  target (see Fig. 1). This is mainly due to the fact that the most neutron-rich fission fragments come from rather cold quasiprojectiles that, in turn, originate from the most peripheral collisions of the  $^{238}\text{U}$  projectile with the targets. As such, the projectile essentially interacts with the neutron-skin of the target. Because of this, we may expect a small effect in the absolute cross sections that we wish to investigate in detail both theoretically and experimentally. However, from a practical standpoint, the use of lighter targets is preferable, as it leads to narrower angular distributions and thus larger acceptance which is desirable for applications of projectile fission in RIB production schemes. We mention that our event-by-event simulations may allow full event tracking of the products through the beam-optical elements of the separator. We can thus determine rates for the production and separation of desired neutron-rich projectile fission fragments, as it is now being performed by members of the KOBRA team [33].

After the above discussion on production cross sections and angular distributions, we wish to provide an overall perspective of accessible neutron-rich nuclides in  $^{238}\text{U}$  projectile fission at 20 MeV/nucleon. In Fig. 4 we show the DIT/SMM calculated production cross sections of projectile fission fragments from the reaction  $^{238}\text{U}$  (20 MeV/nucleon) +  $^{64}\text{Ni}$  on the  $Z$ – $N$  plane. Several cross section ranges are shown by open circles according to the figure key. The closed squares show the stable isotopes. The solid (red) line shows the astrophysical  $r$ -process path and the dashed green line indicates the location of the neutron drip-line as calculated by [31]. We observe that a broad range of very neutron-rich nuclides above Fe ( $Z=26$ ) becomes accessible with the

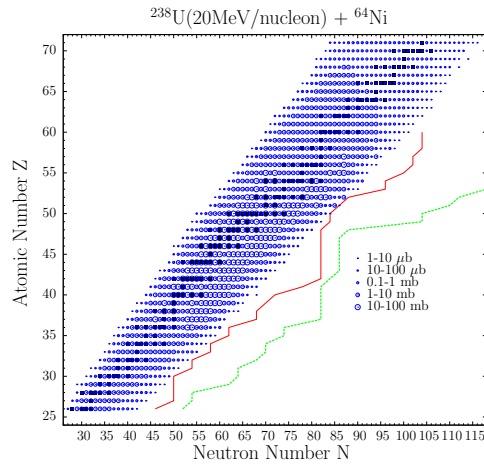


Fig. 4. Representation of DIT/SMM calculated production cross sections of projectile fragments from the reaction  $^{238}\text{U}$  (20 MeV/nucleon) +  $^{64}\text{Ni}$  on the Z–N plane. The cross section ranges are shown by open circles according to the key. The closed squares show the stable isotopes. The solid (red) line shows the astrophysical r-process path and the dashed (green) line shows the location of the neutron drip-line [31].

projectile fission approach at this energy range. We plan to perform larger statistics calculations (to reach approx. 100 times lower cross sections) for practical applications [33].

It is interesting to evaluate, using the above cross section calculations, what total rates we might expect for very short-lived neutron-rich nuclei. For this purpose, we assume a primary  $^{238}\text{U}$  beam intensity of 10 particle nA ( $6.2 \times 10^{10}$  particles/sec) at 20 MeV/nucleon from, e.g, the RISP accelerator complex [?]. Furthermore, we assume a production target thickness of 20 mg/cm<sup>2</sup>  $^{64}\text{Ni}$ , a separator angular acceptance of 20 msr and momentum acceptance of 5%. Under these conditions, we estimate that a production cross section of 10  $\mu\text{b}$  corresponds to a production rate of about 5 counts/sec. Of course, the overall transmission of the separator has to be carefully taken into account along with the above estimate of total rates. However, we may conclude that for a large number of very neutron-rich nuclei, production rates of 10-1000 /sec (at energies around 20 MeV/nucleon) are possible, allowing the study of the structure of these nuclei.

Furthermore, we point out that for very neutron-rich nuclei toward the r-process path, the predicted halflives are less than 1 second, making their production in the ISOL facility very difficult. For such nuclei, counting rates of 10–1000 /day should be reachable with the present projectile fission approach, which suffices to verify their stability and in the most favorable cases allow measurements of their decay properties. Finally, an interesting observation from Fig. 4, is the possibility to move close to (or even reach) the neutron drip-line in the region Z=45–50 (A=130–140) with the present projectile-fission

approach.

Apart from our ongoing calculational efforts on projectile fission, in the near future we plan to perform detailed measurements of projectile fission at Texas A&M with the MARS recoil separator and a  $^{238}\text{U}$  beam at 12 MeV/nucleon. We expect that these measurements, apart from providing a detailed testing ground for our models, will offer access to very neutron-rich nuclei for decay studies, combined with the capabilities of the MARS separator and detector systems. Furthermore, these efforts will provide experience and preparation for future plans at large-acceptance separator facilities (e.g. KOBRA [33]).

In conclusion, we believe that the possibility of producing very neutron-rich nuclides from projectile fission at low energy facilities, as in the KOBRA/RISP facility, will open up a rich and diversified program of nuclear structure studies of neutron-rich rare isotopes in these facilities, complementary to the current successful programs of higher-energy RIB facilities [34–36].

## References

- [1] RISP main page: [www.risp.re.kr/eng/pMainPage.do](http://www.risp.re.kr/eng/pMainPage.do)
- [2] Baseline Design Summary, August 2012, Accessible at <http://www.risp.re.kr/eng/orginfo/infoblds.do>
- [3] K. Tshoo, Y. K. Kim, Y. K. Kwon et al, Nucl. Instrum. Meth. B **317**, 242 (2013).
- [4] Progress report of the RAON recoil spectrometer KOBRA, Low Energy Nuclear Science team (RISP, IBS) and KOBRA Collaboration. Internal Report, February 2014.
- [5] C. B. Moon, AIP Advances **4**, 041001 (2014).
- [6] P.N. Fountas, G.A. Souliotis, M. Veselsky and A. Bonasera, Phys. Rev. C **90**, 064613 (2014).
- [7] G. A. Souliotis et al., Phys. Rev. C **84**, 064607 (2011).
- [8] G. A. Souliotis et al., Phys. Lett. B **543**, 163 (2002).
- [9] G. A. Souliotis et al., Phys. Rev. Lett. **91**, 022701 (2003).
- [10] G. A. Souliotis et al., Nucl. Instrum. Methods **B 204** 166 (2003).
- [11] G. A. Souliotis et al., Nucl. Instrum. Methods **B 266**, 4692 (2008).
- [12] G.A. Souliotis, W. Loveland, et al., Phys. Rev. C **55**, 2146(R) (1997)

- [13] G.A. Souliotis, W. Loveland et al., Proceedings of the 2nd International Conference on Fission and Properties of Neutron-Rich Nuclides, St. Andrews, Scotland, June 1999.
- [14] G.A. Souliotis, W. Loveland et al, Nucl. Phys. A **705**, 279 (2002).
- [15] Y. Blumenfeld, T. Nilsson and P. Van Duppen, Phys. Scr. T152 014023 (2013).
- [16] Texas A&M Cyclotron Institute main page: [cyclotron.tamu.edu](http://cyclotron.tamu.edu)
- [17] R. E. Tribble et al., Nucl. Instrum. Methods A **285**, 441 (1989).
- [18] L. Tassan-Got and C. Stephan, Nucl. Phys. **A 524**, 121 (1991).
- [19] M. Papa et al., Phys. Rev. **C 64**, 024612 (2001).
- [20] M. Papa et al, J. Comp. Phys. **208**, 403 (2005).
- [21] G. A. Souliotis, J. Phys. CS **205**, 012019 (2010).
- [22] J. Bondorf et al., Phys. Rep. **257**, 133 (1995).
- [23] A.S. Botvina and I.N. Mishustin, Phys. Rev. **C 63**, 061601 (2001).
- [24] N. Buyukcizmeci, R. Ogul and A.S. Botvina, Eur. Phys. J. **A 25**, 57 (2005).
- [25] G.A. Souliotis, A.S. Botvina et al., Phys. Rev. **C 75**, 011601 (2007).
- [26] G.A. Souliotis, A.S. Botvina et al., Nucl. Instrum. Methods **B 261**, 996 (2007).
- [27] N. Vonta, G.A. Souliotis, M. Veselsky, A. Bonasera, Phys. Rev. C **92**, 024616 (2015).
- [28] G.A. Souliotis, K. Hanold, W. Loveland et al, Phys. Rev. C **57**, 3129 (1998).
- [29] G.A. Souliotis, Physica Scripta T **88**, 153 (2000).
- [30] M. Thoennessen, Rep. Prog. Phys. **76**, 056301 (2013).
- [31] P. Moller, J.R. Nix and K.L. Kratz, At. Data Nucl. Data Tables **66**, 131 (1997).
- [32] N. Vonta, G.A. Souliotis, W. Loveland, Y.K. Kwon, K. Tshoo, A. Bonasera, A. Botvina et al. in preparation (to be submitted in Phys. Rev. C)
- [33] K. Tshoo, H. Chae, J. Park, J.Y. Moon, Y.K. Kwon, G.A. Souliotis et al, Nucl. Instrum. Methods B **376**, 188 (2016).
- [34] FRIB main page: [www.frib.msu.edu](http://www.frib.msu.edu)
- [35] GSI main page: [www.gsi.de](http://www.gsi.de)
- [36] RIBF main page: [www.rarf.riken.go.jp/Eng/facilities/RIBF.html](http://www.rarf.riken.go.jp/Eng/facilities/RIBF.html)

# Rare Isotope Production in peripheral heavy-ion collisions in the energy range 15-25 MeV/nucleon

A. Papageorgiou<sup>a</sup>, G.A. Souliotis<sup>a,\*</sup>, Y.K. Kwon<sup>b</sup>,  
K. Tshoo<sup>b</sup>, S. C. Jeong<sup>b</sup>, M. Veselsky<sup>c</sup>, A. Bonasera<sup>d,e</sup>

<sup>a</sup> *Laboratory of Physical Chemistry, Department of Chemistry, National and Kapodistrian University of Athens, Athens 15771, Greece*

<sup>b</sup> *Rare Isotope Science Project (RISP), Institute for Basic Science, Daejeon, Korea.*

<sup>c</sup> *Institute of Physics, Slovak Academy of Sciences, Bratislava, Slovakia*

<sup>d</sup> *Cyclotron Institute, Texas A&M University, College Station, Texas, USA*

<sup>e</sup> *Laboratori Nazionali del Sud, INFN, Catania, Italy*

\* *Corresponding author. Email: soulioti@chem.uoa.gr*

---

## Abstract

In this contribution we summarize recent efforts to describe the production of rare isotopes with beams of 15–25 MeV/nucleon expected from low-energy facilities. We first present calculated production cross sections of proton-rich nuclides from collisions of stable beams of mass  $A \sim 60$ –80. Our calculations are performed with the phenomenological deep-inelastic transfer (DIT) model and the microscopic constrained molecular dynamics model (CoMD). De-excitation of the excited quasiprojectiles from the dynamical stage of the reaction is performed with the statistical multifragmentation model (SMM). In addition to the efforts on proton-rich nuclides, we investigated the possibility of producing neutron-rich rare isotopes in the mass range  $A \sim 180$ –200, i.e. near the third r-process peak of  $A=195$ . We performed calculations for a  $^{208}\text{Pb}$  (15 MeV/nucleon) beam and find that the multinucleon transfer mechanism leads to very neutron-rich nuclides in this mass range. We believe that our continued progress on the study of multinucleon transfer reactions using heavy-ion beams of 15–25 MeV/nucleon, can provide new opportunities in rare isotope research in the near future, as planned at the KOBRA facility of RISP in Korea.

---

## 1 Introduction

We have recently presented our efforts to study the production of neutron-rich rare isotopes employing the mechanism of multinucleon transfer with stable or

radioactive beams in the energy range 15–25 MeV/nucleon expected from the RISP accelerator facility [1–3]. We showed that this approach – termed QP (quasiprojectile) fragmentation – offers the possibility of essentially adding neutrons (along with the usual stripping of protons) to a given stable (or radioactive) projectile by its interaction with a neutron-rich target. Our recent article [4] elaborates on our understanding of the reaction mechanism and our description with the phenomenological DIT (deep-inelastic transfer), as well as the microscopic CoMD (Constrained Molecular Dynamics) models.

In the present article, we first summarize our initial efforts regarding the production of proton-rich isotopes in the range  $Z=10$ – $40$ . Our approach, involving peripheral nucleon exchange and then binary deexcitation ( or multifragmentation ), constitutes an efficient way to access extremely proton-rich rare isotopes for a broad variety of studies. Careful review of the current literature indicates that there is a lot of activity in the nuclear physics community concerning the production of proton-rich nuclei at and beyond the proton drip line. Interest has aroused in prompt or sequential two-proton emission [5–9], as well as for nuclides with astrophysical importance in nucleosynthesis cycles involving proton-rich nuclei [10,11].

We performed calculations of proton-rich isotope production cross sections based on our usual hybrid approach: the dynamical stage of the projectile-target interaction is described with either the phenomenological deep-inelastic transfer (DIT) model [12], or with the microscopic constrained molecular dynamics (CoMD) model [14,15]. Subsequently, for the de-excitation of the projectile-like fragments (quasi-projectiles), our version [16] of the statistical multifragmentation model (SMM) [17,18] is employed. In this microcanonical SMM version, careful adjustment of the excitation-energy dependence of the symmetry energy is performed according to our previous findings [16,18]. We showed that our approach constitutes an efficient way to access extremely proton-rich rare isotopes for spectroscopy or reaction studies.

In parallel to the efforts of proton-rich nuclide production, we investigated the possibility of producing neutron-rich nuclides in the mass range  $A\sim 180$ – $200$ , i.e. near the isotones of  $N=126$ , that constitute the third r-process peak of  $A=195$ . This region of n-rich nuclides is of primary importance at present, as indicated by a number of recent references (e.g. [19,20] and references therein). We initiated our study by performing DIT/SMM and CoMD/SMM calculations for a  $^{208}\text{Pb}$  (15 MeV/nucleon) beam interacting with neutron-rich targets and found that the multinucleon transfer mechanism leads to very neutron-rich nuclides in this mass range.

We conclude that we are at the stage of using the present theoretical framework of DIT/SMM or CoMD/SMM for the prediction of exotic proton-rich nuclei or neutron-rich nuclei employing appropriate intense stable beams at

the KOBRA/RISP facility.

## 2 Proton-Rich nuclide production at 15–25 MeV/nucleon

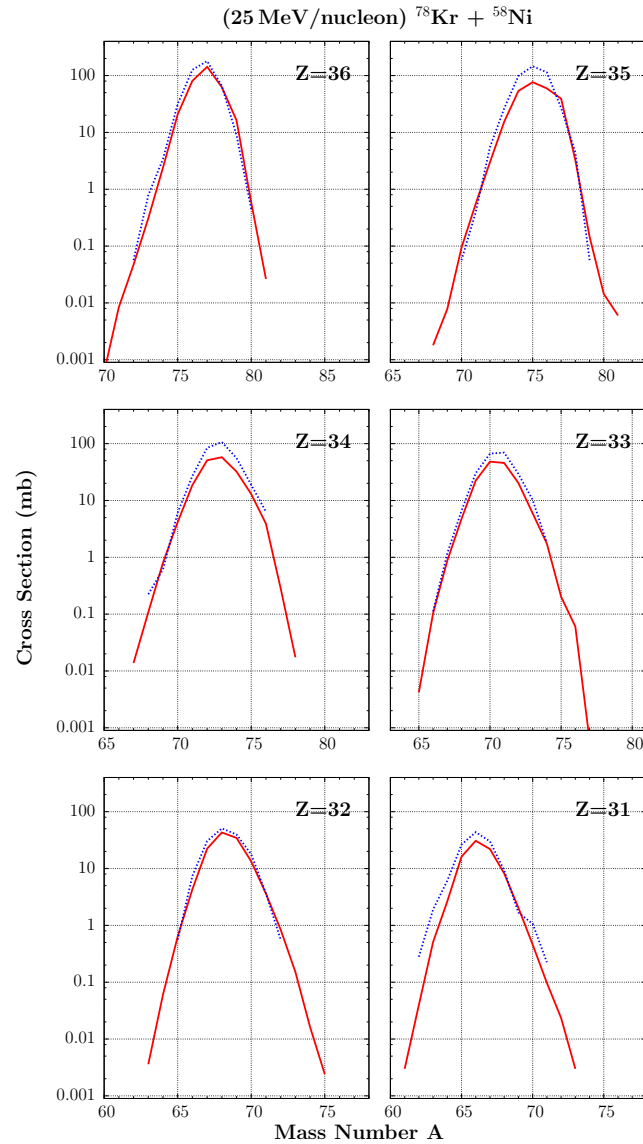


Fig. 1. Calculated mass distributions (lines) of proton-rich nuclides with  $Z=31-36$  from the reaction  $^{78}\text{Kr}(25 \text{ MeV/nucleon})+^{58}\text{Ni}$ . The calculations are: DIT/SMM (solid red line) and CoMD/SMM (dotted blue line)

In Fig. 1, we present the calculated mass distributions of elements with  $Z = 31-36$  from the reaction  $a^{78}\text{Kr}(25 \text{ MeV/nucleon})+^{58}\text{Ni}$ . As already mentioned, in the calculations, we employed the standard DIT code (solid red line) and the CoMD code (dotted blue line). Our version of the SMM code [16] was used for the de-excitation stage. From the figure we observe an overall agreement in

shape of the two calculations the DIT/SMM and the CoMD/SMM. We note that the CoMD calculations are only preliminary and that higher statistics runs are now underway. However, the present comparison reassures that our reaction approaches are in mutual agreement.

In Figs. 2, 3 we present the calculated mass distributions of elements with  $Z=25-30$ ,  $Z=19-24$ , respectively, from the reactions of 25 MeV/nucleon  $^{78}\text{Kr}$  and  $^{64}\text{Zn}$  beams with a  $^{58}\text{Ni}$  target. The calculations are with DIT/SMM for  $^{78}\text{Kr}+^{58}\text{Ni}$  (solid red line) and  $^{64}\text{Zn}+^{58}\text{Ni}$  (dashed green line). Interestingly, we note that for  $Z=30-25$ , essentially near the  $^{64}\text{Zn}$  projectile, the cross sections of proton-rich nuclides are higher with this projectile compared with the  $^{78}\text{Kr}$  projectile. However, for lower mass fragments the cross sections from both beams are nearly similar on the proton-rich side.

In the following we provide, some examples of production rates assuming a primary beam of  $^{78}\text{Kr}$  with intensity of 100 pA ( $6 \times 10^{11}$  particles/s) and a 20 mg/cm<sup>2</sup>  $^{58}\text{Ni}$  target:  $^{65}\text{As}$  ( $4\mu\text{b}$ ,  $4.0 \times 10^2$  counts/s),  $^{58}\text{Zn}$  ( $8\mu\text{b}$ ,  $8.0 \times 10^2$  counts/s),  $^{42}\text{Ti}$  ( $10\mu\text{b}$ ,  $1.0 \times 10^3$  counts/s), and  $^{23}\text{Al}$  ( $10\mu\text{b}$ ,  $1.0 \times 10^3$  counts/s).

We mention that we are also studying the reactions of both  $^{78}\text{Kr}$  and  $^{64}\text{Zn}$  beams with  $^{27}\text{Al}$ ,  $^{48}\text{Ti}$ , as well as  $^{112}\text{Sn}$  targets with results comparable to that of the  $^{58}\text{Ni}$  target that we present here. As a subsequent step, we plan to explore the dependence of the production cross sections on the beam energy. Apart from our chosen 25 MeV/nucleon energy (on which we have performed extensive experimental work in the past with neutron-rich beams), we will also try detailed calculations at 15 and 35 MeV/nucleon. We also plan to compare the present calculations with data from fragmentation reactions [21,22]. Furthermore, we plan to apply our approach in the use of proton-rich RIBs from the first stage of KOBRA to produce even more proton-rich nuclides that can be studied at the subsequent stages of KOBRA.

Apart from the issue of production cross sections of the proton-rich nuclides from the above reactions, we point out that their angular distributions have to be carefully considered when applied to the KOBRA RIB production scheme. Our event-by-event calculations allow full event tracking of the products through the beam-optics simulation of the KOBRA separator, as it has been studied by the members of the KOBRA team. From a practical standpoint, we remind that the DIT code is a rather fast code (in contrast to the computer-intensive CoMD code) and thus, can be used effectively for the design of experiments with proton-rich radioactive beams at the KOBRA/RISP facility.

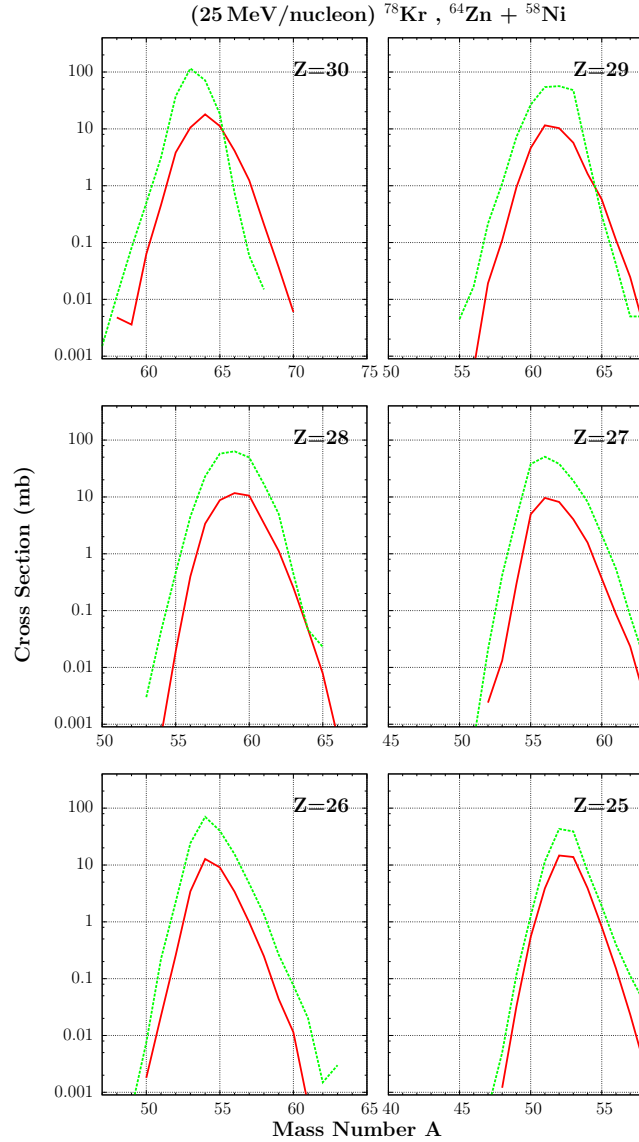


Fig. 2. Calculated (DIT/SMM) mass distributions (lines) of proton-rich nuclides with  $Z=25-30$  from the reactions  $^{78}\text{Kr}(25 \text{ MeV/nucleon})+^{58}\text{Ni}$  (solid red line) and  $^{64}\text{Zn}(25 \text{ MeV/nucleon})+^{58}\text{Ni}$  (dashed green line).

### 3 Results with mass $A \sim 180-200$ beams at 15 MeV/nucleon

In parallel to the proton-rich nuclide studies, we investigated the possibilities of producing neutron-rich rare isotopes in the mass range  $A=180-200$ , i.e. well above the typical heavy fission-fragment mass, accessible to the standard ISOL facilities or the projectile-fission facilities (see, e.g. [23]).

We performed calculations for a  $^{208}\text{Pb}$  (15 MeV/nucleon) beam interacting with a  $^{64}\text{Ni}$  and a  $^{48}\text{Ti}$  target with our DIT/SMM and CoMD/SMM code framework and we found that the multinucleon transfer mechanism can lead

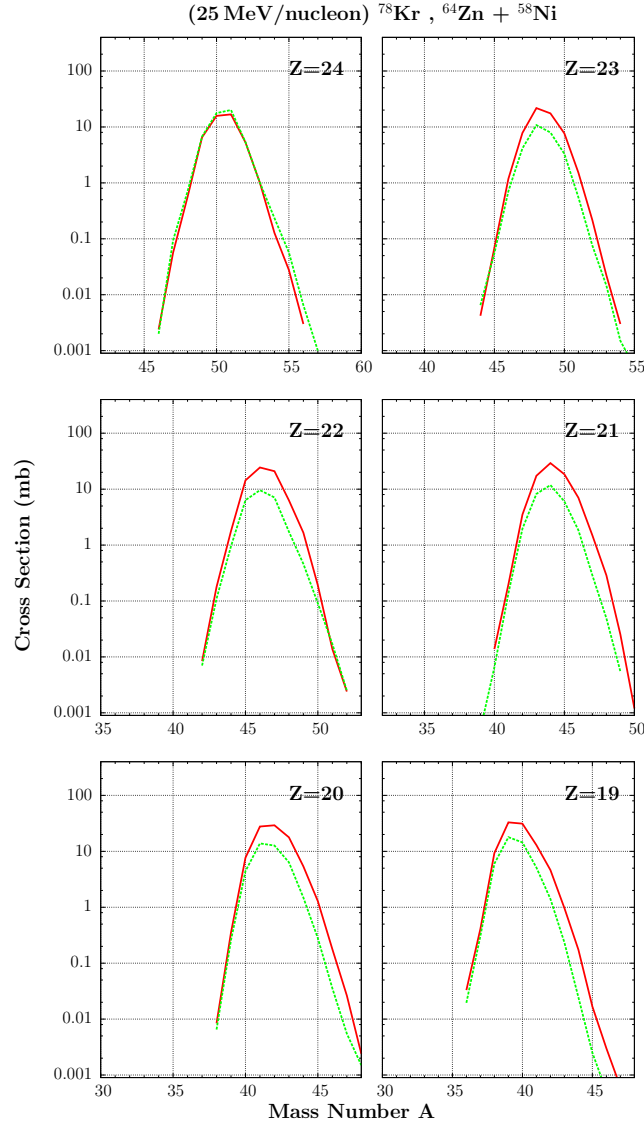


Fig. 3. Calculated (DIT/SMM) mass distributions (lines) of proton-rich nuclides with  $Z=19-24$  from the reactions  $^{78}\text{Kr}(25 \text{ MeV/nucleon})+^{58}\text{Ni}$  (solid red line) and  $^{64}\text{Zn}(25 \text{ MeV/nucleon})+^{58}\text{Ni}$  (dashed green line).

to very neutron-rich nuclides, possibly to new ones in this mass range.

To provide a perspective of the accessible nuclides, we show in Fig. 4 the DIT/SMM calculated production cross sections of projectile fragments from these reactions. We also provide, three examples of production rates assuming a primary beam of  $^{208}\text{Pb}$  with intensity of 100 pnA ( $6 \times 10^{11}$  particles/s) and a  $20 \text{ mg/cm}^2$   $^{64}\text{Ni}$  target:  $^{208}\text{Hg}$  ( $2 \mu\text{b}$ ,  $2.0 \times 10^2$  counts/s),  $^{206}\text{Hg}$  ( $200 \mu\text{b}$ ,  $2.0 \times 10^4$  counts/s), and  $^{200}\text{Pt}$  ( $20 \mu\text{b}$ ,  $2.0 \times 10^3$  counts/s).

So far our comparisons were focused primarily on the use of the  $^{64}\text{Ni}$  target (also the Ti tagret) as a good compromise of high  $N/Z$  ( $N/Z=1.29$ ) and moderate size, so that we keep the products as much as possible forward-focused

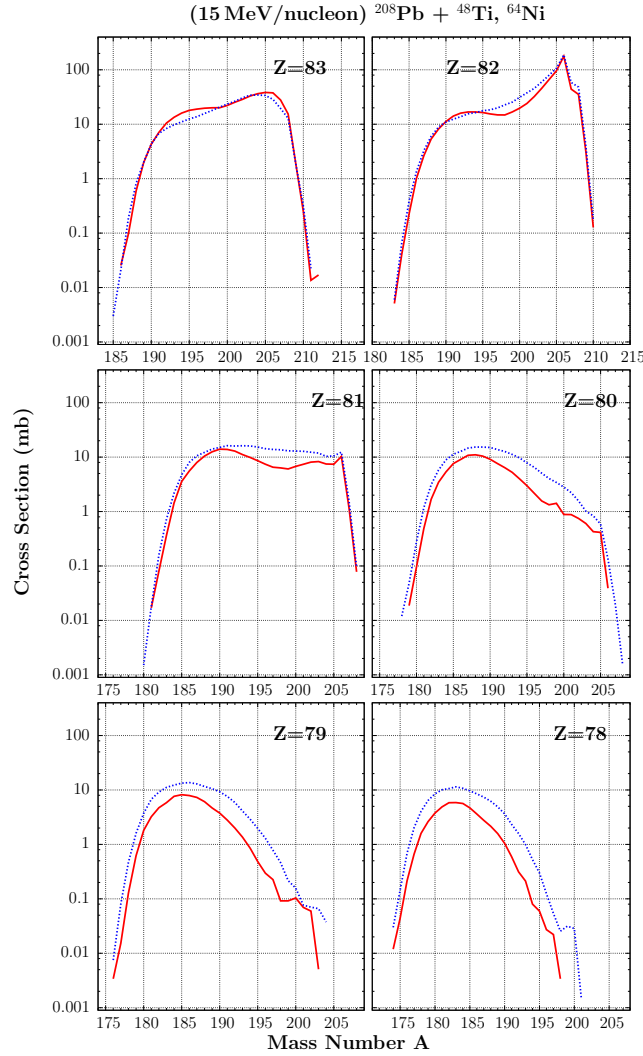


Fig. 4. Calculated (DIT/SMM) mass distributions (lines) of neutron-rich nuclides with  $Z=78-83$  from the reaction of  $^{208}\text{Pb}$  (15 MeV/nucleon) with targets of  $^{48}\text{Ti}$  (solid red line) and  $^{64}\text{Ni}$  (dotted blue line).

(and thus, within the acceptance of the KOBRA separator). As a subsequent step, we plan to explore the reactions of the  $^{208}\text{Pb}$  (15 MeV/nucleon) beam with heavy targets as  $^{124}\text{Sn}$ ,  $^{208}\text{Pb}$ ,  $^{232}\text{Th}$  and  $^{238}\text{U}$ , in order to appreciate the effect of the  $N/Z$  of the target, of course along with the wider angular distributions resulting from the reactions with these heavier targets. In addition, similar reactions with a  $^{198}\text{Pt}$  beam will be explored in detail.

However, from an experimental point of view, we wish to point out that for these heavier projectiles, special attention has to be paid to issues concerning the broad ionic charge-state distribution, as well as the  $Z$  and  $A$  resolutions of the detection system necessary to perform the particle identification. We mention that in the past, we developed a detailed analysis procedure for heavy beams (i.e. Au, U) in this energy range [24] and succeeded in characterizing

the residue distributions from deep-inelastic and incomplete fusion reactions. We even succeeded to identify "new" proton-rich nuclei [25] that have recently been reported in the isotope review article [26]. It is our expectation that we will proceed with our collaborators of the KOBRA group to continue such experimental efforts using appropriate heavy beams from RISP, in order to access new regions of the chart of the nuclides in the near future.

#### 4 Summary and Conclusions

In this contribution, we presented our continued efforts to study the production of rare isotopes with beams of 15–25 MeV/nucleon expected from a low-energy facility, as e.g. the RISP accelerator complex. We first present calculated production cross sections of proton-rich nuclides from collisions of stable beams of mass  $A \sim 60$ –80. Our calculations are performed with the phenomenological deep-inelastic transfer (DIT) model and the microscopic constrained molecular dynamics model (CoMD). De-excitation of the excited quasiprojectiles from the dynamical stage of the reaction is performed with the statistical multifragmentation model (SMM). We find that our approach constitutes an efficient way to access extremely proton-rich rare isotopes for a broad range for spectroscopy studies. In parallel to the efforts on proton-rich nuclides, we investigated the production of neutron-rich rare isotopes in the mass range  $A \sim 180$ –200, i.e. near the third r-process peak of  $A=195$ . We presented calculations for a  $^{208}\text{Pb}$  (15MeV/nucleon) beam and find that the multinucleon transfer mechanism leads to very neutron-rich nuclides in this mass range of interest to spectroscopic and astrophysical studies.

Moreover, since our calculations are complete event-by-event simulations, we are able to systematically study the velocity distributions, the angular distributions and, furthermore, the ionic charge state distributions of the various groups of fragments. This information may help us to perform realistic beam optics simulations of the behavior of the KOBRA spectrometer and the capability to separate and identify the exotic neutron-rich nuclides of interest.

We believe that the present continued progress in the front of peripheral heavy-ion reactions using beams of 15–25 MeV/nucleon, in combination with the unique capabilities of the KOBRA facility are expected to offer new exciting opportunities in rare isotope research in the near future.

## References

- [1] RISP main page: [www.risp.re.kr/eng/pMainPage.do](http://www.risp.re.kr/eng/pMainPage.do)
- [2] K. Tshoo, Y. K. Kim, Y. K. Kwon et al, Nucl. Instrum. Meth. B **317**, 242 (2013).
- [3] K. Tshoo, H. Chae, J. Park, J. Y. Moon, Y.K. Kwon, G.A. Souliotis et al., Nucl. Instrum. Meth. B **376**, 188 (2016).
- [4] P.N. Fountas, G.A. Souliotis et al., Phys. Rev. C **90**, 064613 (2014).
- [5] K. W. Brown et al., Phys. Rev. C **92**, 034329 (2015).
- [6] A. A. Ciemny et al., Phys. Rev. C **92**, 014622 (2015).
- [7] I. Mukha et al., Phys. Rev. Lett. **115**, 202501 (2015).
- [8] M. Pomorski et al., Phys. Rev. C **83**, 061303 (2011).
- [9] R.J. Carroll et al., Phys. Rev. Lett. **112**, 092501 (2014).
- [10] U. Chowdhury et al., Phys. Rev. C **92**, 045803 (2015).
- [11] X. L. Tu et al., Nucl. Phys. A **945**, 89 (2016).
- [12] L. Tassan-Got and C. Stephan, Nucl. Phys. A **524**, 121 (1991).
- [13] M. Veselsky and G.A. Souliotis, Nucl. Phys. A **765**, 252 (2006).
- [14] M. Papa, A. Bonasera et al., Phys. Rev. C **64**, 024612 (2001).
- [15] G. A. Souliotis, J. Phys. CS **205**, 012019 (2010).
- [16] G.A. Souliotis, A.S. Botvina et al., Phys. Rev. C **75**, 011601 (2007).
- [17] A.S. Botvina and I.N. Mishustin, Phys. Rev. C **63**, 061601 (2001).
- [18] N. Buyukcizmeci, R. Ogul and A.S. Botvina, Eur. Phys. J. A **25**, 57 (2005).
- [19] Y. X. Watanabe et al., Phys. Rev. Lett. **115**, 172503 (2015).
- [20] T. Kurtukian-Nieto et al., Phys. Rev. C **89**, 024616 (2014).
- [21] R. Pfaff et al., Phys. Rev. C **53**, 1753 (1996).
- [22] M. Mocko et al., Phys. Rev. C **74**, 054612 (2006).
- [23] Y. Blumenfeld, T. Nilsson and P. Van Duppen, Phys. Scr. T152 014023 (2013).
- [24] G.A. Souliotis, K. Hanold, W. Loveland et al, Phys. Rev. C **57**, 3129 (1998).
- [25] G.A. Souliotis, Physica Scripta T **88**, 153 (2000).
- [26] M. Thoennessen, Rep. Prog. Phys. **76**, 056301 (2013).

# Microscopic description of neutron-induced fission with the CoMD Model: Preliminary Results

S. Papadimitriou<sup>1</sup>, G.A. Souliotis<sup>1\*</sup>, A. Assimakopoulou<sup>1</sup>, A. Bonasera<sup>2,3</sup>, M. Veselsky<sup>4</sup>

<sup>1</sup>*Laboratory of Physical Chemistry, Department of Chemistry, National and Kapodistrian University of Athens, Athens, Greece*

<sup>2</sup>*Cyclotron Institute, Texas A&M University, College Station, Texas, USA*

<sup>3</sup>*Laboratori Nazionali del Sud, INFN, Catania, Italy*

<sup>4</sup>*Institute of Physics, Slovak Academy of Sciences, Bratislava, Slovakia*

*\*Corresponding author. Email: soulioti@chem.uoa.gr*

---

## Abstract

In the present work, we initiated a systematic study of neutron-induced fission reactions using the code CoMD (Constrained Molecular Dynamics) of A. Bonasera and M. Papa [1,2]. The code implements an effective interaction with a nuclear-matter compressibility of  $K=200$  (soft EOS) with several forms of the density-dependence of the nucleon symmetry potential. In addition, CoMD imposes a constraint in the phase space occupation for each nucleon restoring the Pauli principle at each time step of the collision). Proper choice of the surface parameter of the effective interaction has been made to describe fission. In this poster, we presented preliminary results of neutron-induced fission on  $^{235}\text{U}$  at neutron energies 5, 10, 15, 25, 50 and 100 MeV. Calculated mass and energy distributions are shown and compared with the recent experimental data of Loveland et al. [3]. It appears that the microscopic code CoMD is able to describe the complicated many-body dynamics of the n-induced fission process. Proper adjustment of the parameters of the effective interaction and further improvements of the code will be implemented to achieve a satisfactory description of the experiment data.

---

## INTRODUCTION

The microscopic description of the mechanism of nuclear fission still remains a topic of intense nuclear research. Understanding of nuclear fission, apart from the theoretical many-body point of view, is of exceptional practical importance for energy production, as well as for the transmutation of nuclear waste. Furthermore, nuclear fission is the mechanism that sets the upper limit to the periodic table of the elements (via the so-called fission-recycling process) and plays a vital role in the production of heavy elements via the astrophysical rapid neutron-capture process (r-process).

The present work is a study of neutron-induced fission based on the semi-classical microscopic N-body constrained molecular dynamics (CoMD) model in regards to its ability to describe the full dynamics of the fission process in neutron induced reactions on  $^{235}\text{U}$  at low and intermediate energies. We remind that most of the energy released in the fission process appears in the kinetic energy of the fission fragments. The deformed scission-point fragments will return to their equilibrium deformations and the deformation

energy will be converted into internal excitation energy. These quantities depend on the mass split in fission which in turn, at low excitation energies, may reflect the fragment nuclear structure. We intent to study these quantities with CoMD model.

## RESULTS AND DISCUSSION

We performed CoMD calculations on the neutron induced fission of  $^{235}\text{U}$ , at neutron energies 5, 10, 15, 25, 50, 100 MeV. In Fig. 1, we present the mass yield curves for the fission reaction  $n + ^{235}\text{U}$  at energy 50 MeV employing the standard and soft symmetry potential [2]. We observe that  $^{235}\text{U}$  is undergoing asymmetric fission as indicated from the double-humped curve. In the near future, we plan to explore this feature of the calculations in detail.

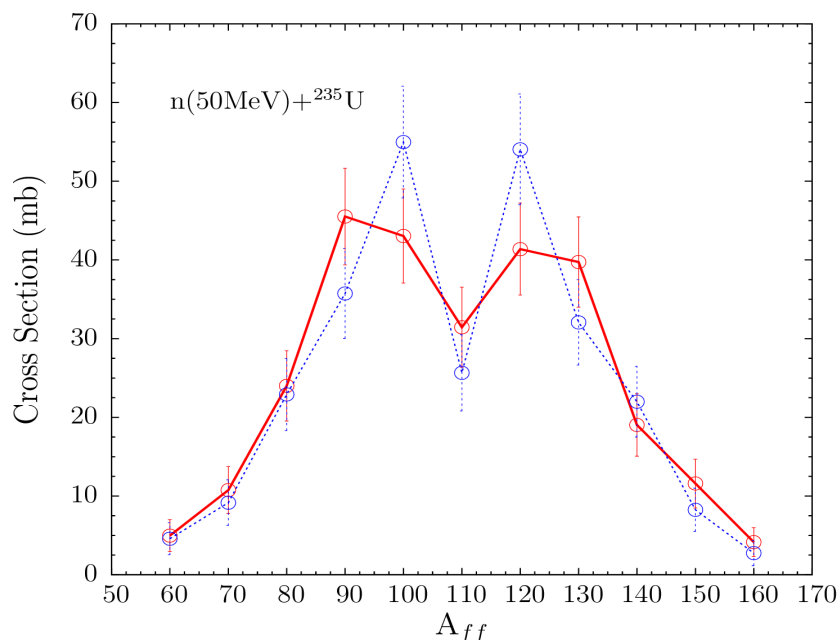


**Fig. 1.** CoMD calculated mass-yield curves for the fission reaction  $n(50\text{MeV})+^{235}\text{U}$ . Red points (connected with a continuous line): calculations with the standard symmetry potential [2]. Blue points (connected with a dotted line): calculations with the soft symmetry potential [2].

In Fig. 2, a plot of the total kinetic energy of the fission fragments versus the neutron energy is presented. Our calculations with the CoMD model were performed with the standard and the soft symmetry potential [2] and they were compared with the experimental data of Loveland et al. [3].

A reasonable agreement (within a few MeV) of our calculations with the data is obtained. We plan to explore and understand the differences in the near future.

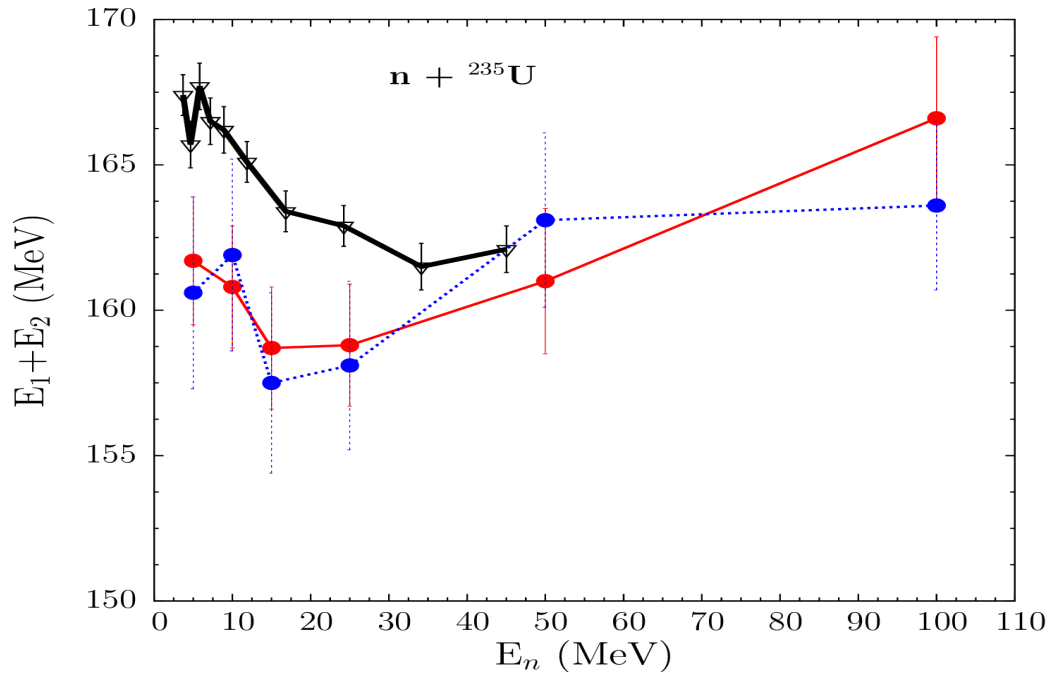


**Fig. 2.** CoMD calculations of the average total energy of fission fragments from  $n+^{235}\text{U}$  with respect to neutron energy. Red points (connected with a continuous line) : CoMD calculations with the standard symmetry potential [2]. Blue points (connected with a dotted line): CoMD calculations with the soft symmetry potential [3]. Black points (connected with thick solid line) : experimental data of Loveland et al. [3].

## CONCLUSIONS

In the present work we employed the semi-classical microscopic code CoMD to describe neutron-induced fission of  $^{235}\text{U}$  in a variety of energies and compared our results with available experimental data. Our preliminary results are in overall agreement with the experimental data. We intend to study systematically neutron-induced fission by calculating various observables such as: mass-yield curves, cross sections, energy distributions, fission time scale, as well as, pre-fission and post-fission neutron emission.

We mention that the present version of the CoMD code does not include the effect of spin-orbit interaction in the mean field, as a result of the absence of spin dependence of the effective nucleon-nucleon interaction used [1,2]. We intend to add such a dependence in the code to improve our ability to describe the low-energy fission of actinides, and most notably, the well-pronounced double-humped structure of the mass-yield curves.

## References

- [1] M. Papa, A. Bonasera et al., Phys. Rev. C 64, 024612 (2001)
- [2] N. Vonta, G.A. Souliotis et al., Phys. Rev. C 92, 024616 (2015)
- [3] R. Yanez, W. Loveland et al., Phys. Rev. C 89, 051604 (2014)